December 2014

An Optimization Method for Estimating Joint Parameters of the Hip and Knee

Ben Tesch
University of Wisconsin-Milwaukee

AN OPTIMIZATION METHOD FOR ESTIMATING JOINT PARAMETERS OF THE HIP AND KNEE

by

Ben Tesch

A Thesis Submitted in

Partial Fulfillment of the

Requirements for the Degree of

Master of Science

in Engineering

at

The University of Wisconsin-Milwaukee

December 2014

ABSTRACT
AN OPTIMIZATION METHOD FOR ESTIMATING JOINT PARAMETERS OF THE HIP AND KNEE

by

Ben Tesch

The University of Wisconsin-Milwaukee, 2014
Under the Supervision of Professor Brian S.R. Armstrong

Biomechanics, generally speaking, concerns the application of engineering principles to the study of living things. This work is concerned with human movement analysis, a subfield of biomechanics, where the methods of classical mechanics are applied to human movement. This field has contributed to the general understanding of human movement, and its techniques are used in the diagnosis and treatment of disease. Central to the field is the process of measuring human movement. Since classical mechanics deals with the motion of rigid bodies, and ideal measurement system would be able to accurately record the exact pose — combined position and orientation — of the bones. The techniques that reach this ideal require exposure to radiation or the insertion of metal pins into bones. Non-invasive methods are far more commonly used, and these involve the optical tracking of special markers placed over the skin on each segment of the body being studied. Motion capture systems are able to accurately record the pose of the markers, but they bear no repeatable relationship to the pose of the underlying bone. Many techniques are employed to bridge the gap between the two. The most direct technique finds three or more points on each bone near the surface of the skin, called Anatomical Landmarks (ALs), and uses them to define the bone's pose relative to the motion tracking markers. There are concerns about the reliability of this method; the same experimenter performing this procedure multiple times on the same subject will choose slightly different points on the bone, leading to variation in its orientation. The problem is exacerbated when multiple experimenters are involved. This affects the ability to compare data across time or between working groups;

it may also lead to erroneous interpretations of data. Furthermore, this technique cannot be used directly to locate the hip joint center; instead, ALs at the pelvis are used as independent variables in a regression equation which statistically predicts the hip joint center location. Such techniques have begun to show reasonable reliability only recently.

An alternative approach is to orient the bones based on a mathematical analysis of the motion of the tracking markers while the subject moves. This is the domain of functional and optimization methods. Functional methods are commonly used to find two joint parameters in particular: the center of the hip joint and the axis of rotation of the knee. Once found, these parameters are used to determine the orientation of the bones relative to the tracking markers. Functional methods are subject specific and operator independent but may be biased due to the presence of Soft Tissue Artifact (STA), which is the measurement error caused by the movement of tissue in between the tracking markers and the underlying bone. Optimization methods estimate joint parameters by fitting a kinematic model of the joints under study to motion data which records a subject exercising those joints. Unlike functional methods, which estimate parameters for a single joint, optimization methods may estimate the parameters of multiple joints in some circumstances. The parameters of a kinematic model incorporating multiple joints may be estimated as long as the relative pose of the end segments of the model is measured with more Degrees of Freedom (DoF) than the model itself possesses. *The key insight of this work* is that a kinematic model which contains a spherical hip joint and a 2 DoF compound hinge knee joint may be fitted to motion data from the pelvis and lower leg. There are two benefits to this procedure. First, the thigh is known to be affected by a high degree of STA; by removing dependence on data from the thigh, this method gains the potential for more accurate joint parameter estimates. Second, once fitted to movement data, the model provides an estimate of the pose of the femur. One may investigate STA at the thigh by comparing the pose of the thigh markers to the model's estimate of the pose of the femur. Typically, medical imaging or invasive methods are required to investigate STA; this procedure is accessible and safe.

In summary, this work presents a technique which has the potential to make the

non-invasive measurement of human movement more reliable. This technique also provides the possibility of estimating soft tissue artifact at the thigh in a safe and convenient manner.

TABLE OF CONTENTS

LIST OF FIGURES

LIST OF TABLES

Chapter 1

Background Material

1.1 Introduction

The field of human movement analysis applies the techniques of classical mechanics to the study of human movement. This field is concerned both with the diagnosis and treatment of disease, as well as with the broader investigation of human movement in its various forms. Since classical mechanics concerns the mathematical analysis of rigid bodies, it is desirable to quantitatively measure the *pose*, the combined position and orientation, of the human body's rigid bodies — the bones. For reasons of practicality and safety, such measurement is not often carried out directly. Instead, optical tracking markers are placed over the surface of a subject's skin on each segment of the body under study, and a motion capture system tracks the pose of the markers as the subject moves [7].

Placing the tracking markers over the skin has two drawbacks. The first is that the markers do not have a repeatable relationship to the underlying bone across data collections or subjects [7]; this prevents the meaningful comparison of different data sets unless further steps are taken. The second drawback is called Soft Tissue Artifact (STA). It encompasses the measurement error which results from movement of the tissue in between the tracking markers and the underlying bone [22].

The unreliable relationship between the tracking markers and bones is overcome by defining, for each body segment, the pose of the underlying bone relative to the tracking markers. This is typically carried out by manually palpitating points on the bone which are near the surface of the skin, a procedure which is prone to operator error and may introduce spurious results during data processing [10]. Functional methods aim for improved reliability by defining the pose of the bones relative to the tracking markers using joint

parameters, which include the centers and axes of rotation of the body's joints. Functional methods estimate joint parameters by a mathematical analysis of a subject's movement data, removing the potential for operator error [29]. Unfortunately, they are adversely affected by STA [27].

This work presents a method for estimating the joint parameters of the hip and knee by fitting a kinematic model incorporating both joints to motion capture data from markers on the pelvis and lower leg. Model fitting is accomplished using a nonlinear optimization routine, which is operator independent, just like functional methods. Furthermore, the particular combination of kinematic model and optimization routine set forth in this work removes dependence on data from the thigh segment, which is prone to a high degree of STA. This opens the possibility for more accurate estimates of the joint parameters of the hip and knee, which would improve the quality of data used in human movement analysis.

The kinematic model and optimization routine mentioned above are covered in Chapters 2, 3, and 4. For more information on these chapters, see Section 1.5. The present chapter covers background information assumed in Chapters 2, 3, and 4 under two main sections: *background in biomechanics*, which primarily covers data collection in human movement analysis and *background in parameter estimation*, which is basic to understanding the optimization routine. These are tied together by a final section discussing functional methods, which were mentioned above.

1.2 Background in Biomechanics

Biomechanics is the application of classical mechanics to the study of living things. Less broadly, the present work focuses on the kinematics of the human hip and knee, where kinematics is the subfield of classical mechanics which concerns the motion of rigid bodies [24, p. 3]. This chapter begins by defining helpful terminology for describing the body and its movement and proceeds to cover motion capture technology and the mathematical techniques for quantifying human movement; these topics are basic to the understanding of later chapters.

1.2.1 Anatomical Directions

Consider two people talking about a part of the body: The first says to the second, "The right side of the leg," and means to indicate the right side of the right leg. The second person (mis)understands the first to mean the right side of the left leg. Initially, these two people will be unaware that they are talking about opposite things! Appropriate terminology helps to prevent such misunderstanding.

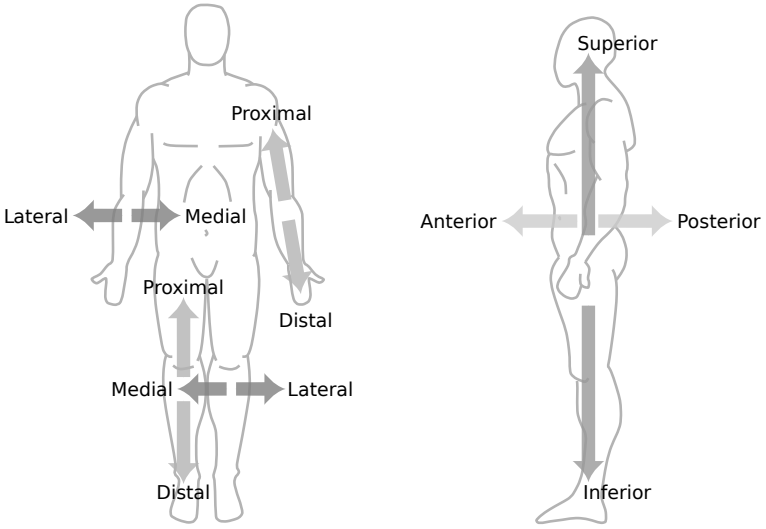

Figure 1.1: Anatomical Direction Terms [39]

The terms right and left are always considered from the perspective of the person they refer to; in this case it is the person in Figure 1.1. The terms *medial* and *lateral* solve the sort of misunderstanding in the paragraph above due to a special property: Whether one's point of reference is on the right arm or the left leg, the medial direction points inward toward the body, while the lateral direction points outward away from it. This reflects the symmetry of our bodies.

The *superior* direction points toward the top of the head, while the *inferior* direction points toward the bottom of the feet. These terms maintain their anatomical meaning during a hand stand, for instance, which is why they are used instead of more common terms like up and down. In a similar vein, superior and inferior are ambiguous when referring to the arm, which may be raised up over one's head or held down at one's side. This ambiguity is resolved by using the terms *proximal* and *distal* when referring to the limbs. The proximal

direction points toward the attachment point for the limb, while the distal direction points away from it.

Finally, the terms *anterior* and *posterior* have the same meaning as the non-latinate terms front and back, respectively. The terms in this section follow the definitions laid out in [19, pp. 8–9].

1.2.2 Anatomical Planes

The anatomical axes and planes, shown in Figure 1.2, are additional terminological tools for describing anatomical locations and bodily movements. In particular, they will be useful for describing joint motion in Section 1.2.3.

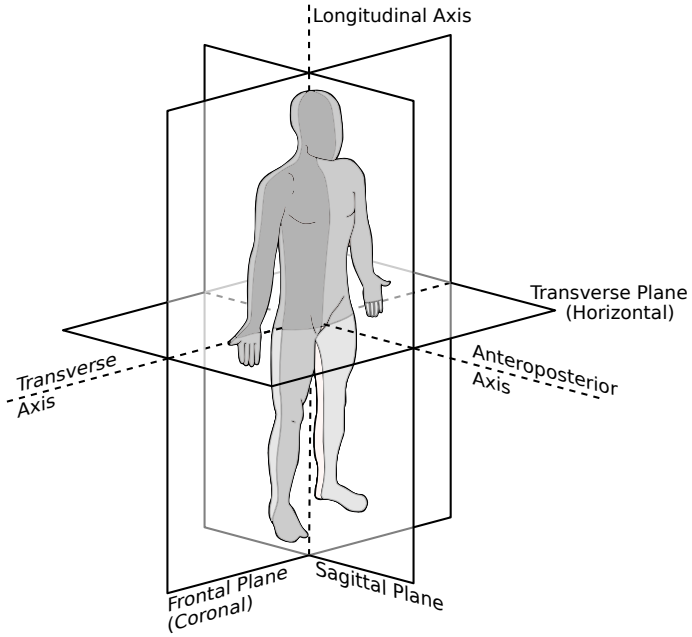

Figure 1.2: Anatomical Planes [37]

The *transverse plane*, also called the *horizontal plane*, passes through the body horizontally and is parallel to the ground. The *sagittal plane* passes through the body vertically and is oriented in the anterior direction. The *frontal plane*, sometimes called the *coronal plane*, also passes throught the body vertically, but it is oriented from left to right. These planes are pictured as intersecting at the center of the body, but they may be translated, conceptually, along the axes to which they are perpendicular. For example, the *transverse axis*, which is defined by the intersection of the frontal and transverse planes, is perpendic-

ular to the sagittal plane. The sagittal plane may be thought to translate left or right along the transverse axis such that, if the person in Figure 1.2 were to bend his right knee, this motion would be said to occur in the sagittal plane.

The *anteroposterior* axis points in a direction fitting of its name and is defined by the intersection of the transverse and sagittal planes. The *longitudinal axis* points along a superior-inferior direction and is defined by the intersection of the frontal and sagittal planes. The anatomical axes, like the anatomical planes, may be translated conceptually from their position in Figure 1.2, provided their orientation remains constant. For example, if the person in the figure were to bend his right knee, the lower part of his leg would be said to rotate about a transverse axis.

The persons represented in Figures 1.1 and 1.2 are standing in what is called the *anatomical position*. This is a reference posture that consists in standing straight with one's arms held at one's side with the palms facing anteriorly. It is a useful starting point for describing different postures or drawing anatomical reference figures. The discussion in this section follows [19, pp. 9–12].

1.2.3 Joint Motion

Joints allow our bodies to realize a wonderful variety of poses. Fortunately, as in previous sections, terminology exists which helps to categorize and describe this variety. Since the focus of the present work is on the hip and knee, discussion will be restricted to these joints.

Flexion is a joint movement which occurs in the sagittal plane and decreases the angle between the proximal and distal segments of the joint. At the hip, the proximal segment is the pelvis, and the distal segment is the femur. At the knee, the proximal segment is the femur, while the distal segment is the tibia.

Flexion of the hip consists in raising the leg anteriorly in the sagittal plane; this decreases the angle between the femur and pelvis. Knee flexion, on the other hand, consist of raising the *lower leg* or *shank* (the portion of the leg between the knee and ankle) posteriorly in the sagittal plane. This movement would appear to be the opposite of flexion at the hip, but it is consistent with the definition of flexion because it decreases the angle between the femur and tibia. See Figures 1.3 and 1.4.

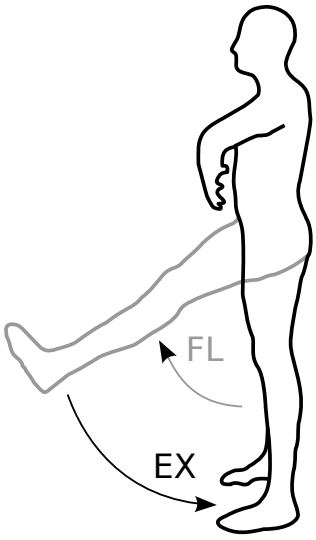

Figure 1.3: Flexion / Extension of the Hip

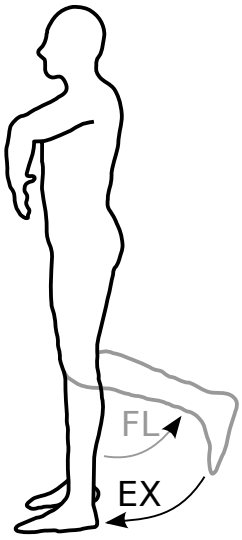

Figure 1.4: Flexion / Extension of the Knee

Extension, which increases the angle between the proximal and distal segments, is the opposite of flexion. Sometimes, both terms are referred to as a group, such as in the sentence, "This movement exhibits very little flexion or extension." The abbreviation FL/EX is helpful in such cases. At the knee, *full extension* occurs when the femur and tibia are colinear. *Hyperextension* is extension beyond this point; it has a range of about 5 to 10 degrees [24, p. 443].

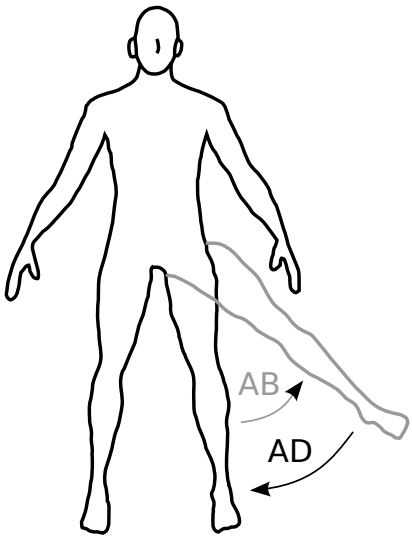

Figure 1.5: Adduction / Abduction of the Hip

If one envisions a longitudinal axis running down the middle of the body, as in Figure 1.2, *abduction* involves a movement away from this axis in the frontal plane, while *adduction* involves a movement toward it. Hip abduction, then, involves raising the leg laterally in the frontal plane, and hip adduction is the opposite movement (Figure 1.5). The knee also undergoes small amounts of AD/AB [4]. Following the scheme above, knee abduction consists of a lateral movement of the shank relative to the thigh in the frontal plane, while knee adduction is the opposite movement. The term *valgus* is sometimes used in place of abduction and *varus* in place of adduction when referring to the knee [24, p. 448].

Internal / external rotation, abbreviated IN/EX, occurs at both the hip and knee. At the hip, it involves rotation of the femur about its proximal-distal axis. Starting from the anatomical position, internal rotation of the hip causes the foot to rotate in the transverse plane such that the toes point in a medial direction. External rotation under the same conditions would cause the toes to point laterally.

Similar to the hip, IN/EX at the knee involves rotation of the tibia about its proximal-distal axis. When the knee is flexed to 90°, the proximal-distal axis of the tibia aligns with the anterior-posterior axis. In this posture, internal rotation of the knee causes the foot to rotate in the frontal plane such that the toes point in a medial direction; external rotation is again the opposite movement.

The above movements and terminology have been described largely in isolation from each other, starting from a standing posture; this follows the exposition in [19, pp. 12–14]. It is possible to combine the terms to describe a wide variety of postures, but specificity is lacking due to their qualitative nature. The remaining sections of this chapter build up mathematical and scientific techniques which may be used to quantify a wide range of human movement.

1.2.4 Motion Capture

In order to apply the techniques of kinematics to the analysis of human movement, that movement must first be quantified or measured. Since classical mechanics as a whole deals with the analysis of *rigid bodies* — objects which do not deform — an ideal measurement system would measure the exact *pose* of the bones, the structures of the human body which

are least deformable (Figure 1.6). (The pose of an object encompasses both its position and orientation.) This ideal type of measurement may be accomplished using intracortical pins or bi-plane fluoroscopy, but such methods come with ethical concerns [22]. Far more commonly used is an optical motion tracking system which can measure the pose of markers placed on the subject's skin (Figure 1.7). The pose obtained from the marker on a particular segment of the body is then assumed to coincide with the pose of the underlying bone [7].

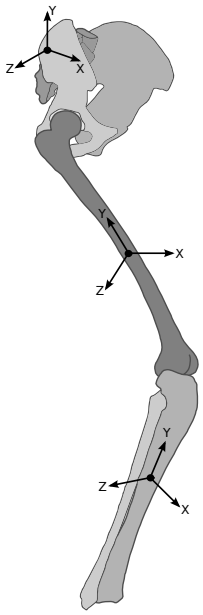

Figure 1.6: Ideal measurement would yield the pose of each bone.

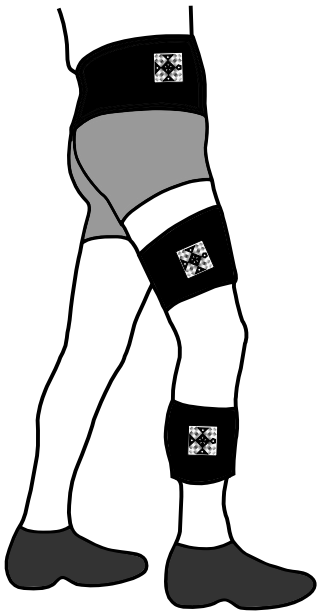

Figure 1.7: Practical measurement places markers over the skin, yielding the pose of each bodily segment.

In Figure 1.6, the pose of each bone is represented graphically by a reference frame (or coordinate frame). The position of a bone in space is given by the origin of its corresponding reference frame in cartesian coordinates. Position is a 3 *Degree of Freedom* (DoF) measurement, as position may vary independently in its X, Y, or Z coordinate, each constituting a degree of freedom. Similarly, the orientation of a bone in space is given by the axes of its corresponding reference frame. This too is a 3-DoF measurement, as a reference frame may rotate about its X, Y, or Z axes. In total, pose constitutes a 6 degree of freedom measurement [45, p. 104].

This work uses a Moiré Phase Tracking (MPT) system by Metria Innovation (Milwaukee,

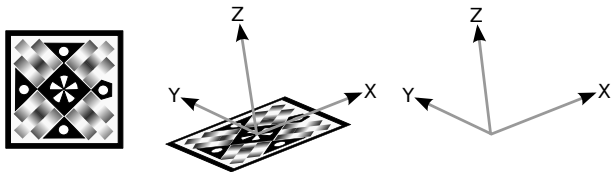

Figure 1.8: The MPT system measures the complete pose of each marker, represented here by a reference frame.

WI), whose markers are pictured in Figures 1.7 and 1.8. The MPT system is composed of a single camera with integrated light source, a set of markers, and a computer. The markers are engineered to produce distinct moiré patterns which allow the system to measure a marker's orientation relative to the plane of the camera's sensor. This information, combined with measurements in the plane of the camera's sensor, results in a 6-DoF measurement of the marker's pose [43]. Company literature reports position accuracy to be 1 part in 2500 of the distance from the marker to the camera (e.g. $\pm$1mm at 2.5m distant) and an orientation accuracy of $\pm 0.05^\circ$ [23].

The goal is to capture *movement*, and in order to do this, the camera takes a series of snapshots at a very high rate. Each snapshot results in a *frame of data* or *data frame* (the term data is used to disambiguate data frames and reference frames). One frame of data contains the pose of every marker visible to the camera in the instant the data frame was captured. The camera records data at up to 90 frames per second, resulting in a series of poses for each marker which progresses in time.

There are two caveats to the measurement process described above. First, the assumption that the pose of a skin-mounted marker tracks the underlying bone is not always valid. Skin sliding and tissue deformation cause this assumption to be violated and are grouped under the term *Soft Tissue Artifact* (STA). STA is a major hindrance to the analysis of human movement [22] and will be discussed below. Second, the description above only specifies that a marker is attached somewhere on each segment to be measured. Given this lax requirement, marker placement could be highly variable across different data collection sessions, and this would severely limit the ability to compare different data sets [7]. The next section provides a solution to this problem.

1.2.5 Technical and Anatomical Reference Frames

The reference frames associated with markers are called *Technical Frames* (TFs). Reference frames which are aligned to the subject's anatomy are called *Anatomical Frames* (AFs). While the technical frames vary in their relation to the subject's bones across collections due to varying placement of the markers, the anatomical frames are more consistent. This is because anatomical frames are constructed using *Anatomical Landmarks* (ALs) — points on the body where the underlying bone is palpable due to limited soft tissue coverage. This paragraph follows [7].

1.2.5.1 Anatomical Landmarks

Several common ALs are labeled with their abbreviated names in Figures 1.9 and 1.10. The abbreviations expand as follows: LASI and RASI, Left and Right Anterior Superior Iliac Spine; LPSI and RPSI, Left and Right Posterior Superior Iliac Spine; MEKN and LAKN, Medial and Lateral Femoral Epicondyle; MEMA and LAMA, Medial and Lateral Malleolus. For a more complete listing, see [6].

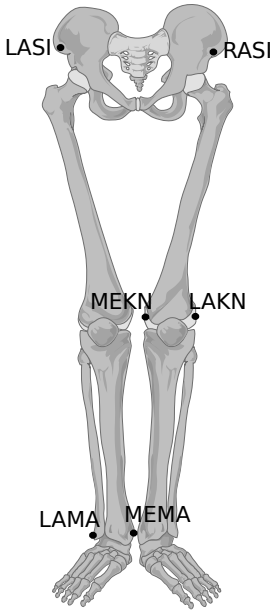

Figure 1.9: Anatomical Landmarks (Anterior View) [42]

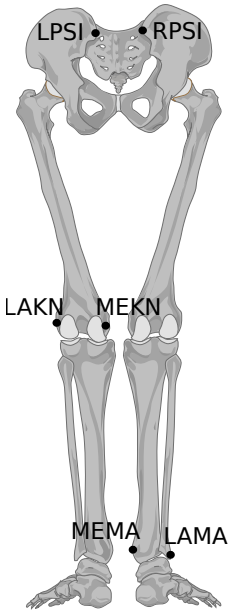

Figure 1.10: Anatomical Landmarks (Posterior View) [41]

A special pointing tool is used to locate the ALs in space; it consists of an MPT marker mounted onto a wand of dimensionally stable plastic which tapers to a point at the tip of the wand. The precise location of the pointing tool tip in the reference frame of the pointing tool marker is known from a calibration procedure. Thus, when the MPT system measures the marker's pose, the location pointing tool tip is also known.

To locate an AL, the researcher places the pointing tool tip over the AL on the subject and records the pose of the subject's markers and the pointing tool marker. The location of the AL may then be represented in the technical frame of the body segment where the AL resides; for example, the MEKN landmark would be represented as a point in the femoral technical frame — the reference frame of the thigh marker. As the subject moves, this point will continue to track the MEKN landmark because the thigh marker will track the motion of the femur. This is useful because the marker's pose relative to the femur varies across data collections, but the location of the MEKN landmark on the bone does not change.

If three ALs are located on a segment of the body, they may be used to construct a complete reference frame for that segment which is aligned to the subject's anatomy. This is an anatomical frame, and its pose relative to the bone will be fairly consistent across data collections. The mathematical construction of such anatomical frames is covered next.

1.2.5.2 Transformation Between Reference Frames

This section demonstrates by example the mathematical technique used to transform a point from representation in the coordinates of one reference frame to representation in the coordinates of another reference frame.

Figure 1.11 shows two reference frames (A and B), their origins, their axes, and a point G. Frames A and B differ in orientation, as frame B has been rotated 45° counterclockwise about its X axis. The axes of frame B represented as unit vectors in frame A ($^{A}\widehat{X}_{B}$, $^{A}\widehat{Y}_{B}$, and $^{A}\widehat{Z}_{B}$) as well as the origin of frame B (denoted $\mathring{B}$) represented as a point in frame A ($^{A}P_{\mathring{B}}$) appear in Equation 1.1. If these quantities are grouped as the columns of a matrix, and a bottom row of $\begin{bmatrix} 0 & 0 & 0 & 1 \end{bmatrix}$ is appended to it, the result is the *homogeneous transform* from frame B to frame A, ${}^{A}_{B}T$. A may be called the *from* frame and B the *to* frame of the transform. It is also helpful to think of ${}^{A}_{B}T$ as frame B represented in frame A coordinates.

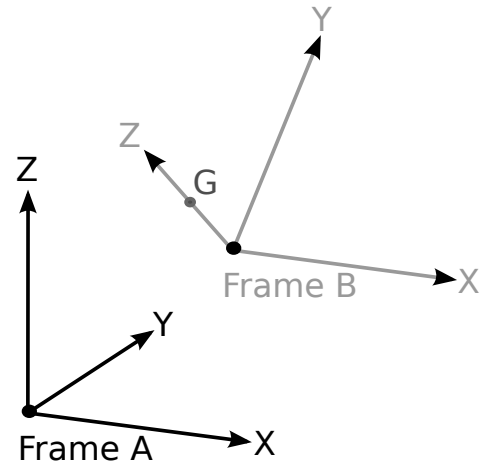

Figure 1.11: Reference Frame Example

$$ {}^{A}\widehat{X}_B = \begin{bmatrix} 1 \\ 0 \\ 0 \end{bmatrix} \quad {}^{A}\widehat{Y}_B = \begin{bmatrix} 0 \\ \frac{\sqrt{2}}{2} \\ \frac{\sqrt{2}}{2} \end{bmatrix} \quad {}^{A}\widehat{Z}_B = \begin{bmatrix} 0 \\ -\frac{\sqrt{2}}{2} \\ \frac{\sqrt{2}}{2} \end{bmatrix} \quad {}^{A}P_{\circ_B} = \begin{bmatrix} \frac{4}{5} \\ \frac{4}{5} \\ \frac{4}{5} \end{bmatrix} \tag{1.1} $$

$$ {}^{A}_{B}T = \begin{bmatrix} 1 & 0 & 0 & \frac{4}{5} \\ 0 & \frac{\sqrt{2}}{2} & -\frac{\sqrt{2}}{2} & \frac{4}{5} \\ 0 & \frac{\sqrt{2}}{2} & \frac{\sqrt{2}}{2} & \frac{4}{5} \\ 0 & 0 & 0 & 1 \end{bmatrix} \tag{1.2} $$

A Homogeneous Transform (HT) is a 4x4 matrix which combines the operations of rotation and translation into a single matrix multiplication. The first three columns of ${}^{A}_{B}T$ hold the relative orientation of the A and B reference frames and carry out the rotation part of the transform. The fourth column holds the relative position of the two frames and handles the translation part. When ${}^{A}_{B}T$ multiplies point G expressed in B coordinates

($^{B}P_{G}$), with an additional 1 appended to its vector,

$$ {}^{A}_{B}T \cdot {}^{B}P_{G} = \begin{bmatrix} 1 & 0 & 0 & \frac{4}{5} \\ 0 & \frac{\sqrt{2}}{2} & -\frac{\sqrt{2}}{2} & \frac{4}{5} \\ 0 & \frac{\sqrt{2}}{2} & \frac{\sqrt{2}}{2} & \frac{4}{5} \\ 0 & 0 & 0 & 1 \end{bmatrix} \cdot \begin{bmatrix} 0 \\ 0 \\ \frac{1}{2} \\ 1 \end{bmatrix} = \begin{bmatrix} \frac{4}{5} \\ \frac{4}{5} - \frac{\sqrt{2}}{4} \\ \frac{4}{5} + \frac{\sqrt{2}}{4} \\ 1 \end{bmatrix} = {}^{A}P_{G}, \tag{1.3} $$

it is transformed into an A coordinate representation ($^{A}P_{G}$). Note that the point has not moved; its is merely expressed in a different reference frame. Further note that, while the additional element of value 1 is not written in the multiplication ${}^{A}_{B}T \cdot {}^{B}P_{G}$, it is appended to the vector ${}^{B}P_{G}$ when that multiplication is carried out. This is a simple notational convenience.

The X component of ${}^{A}P_{G}$ is due entirely to the translation between reference frames A and B, and it appears because the fourth column of ${}^{A}_{B}T$ multiplies the 1 that was appended to ${}^{B}P_{G}$. The Y and Z components of ${}^{A}P_{G}$ have components due both to the translation between the A and B frames ($\frac{4}{5}$) and to the orientation of ${}^{A}\widehat{Z}_{B}$ multiplied by the component of ${}^{B}P_{G}$ along that axis ($\pm\frac{\sqrt{2}}{4}$). One can see how translation and rotation are both needed to account for the change in pose when transforming a point between reference frames.

1.2.5.3 Properties of Homogeneous Transforms

The example of the previous section only covers the basic function of homogeneous transforms. HTs have a variety of theoretical properties that make them a versatile tool for working with 3D data, and these properties are the subject of this section.

The HT ${}^{A}_{B}T$ may be written

$$ {}^{A}_{B}T = \begin{bmatrix} & {}^{A}_{B}R & & {}^{A}P_{\circ_{B}} \\ & & & \\ 0 & 0 & 0 & 1 \end{bmatrix}, \tag{1.4} $$

where the component ${}^{A}_{B}R$ is a special type of 3×3 matrix called a *rotation matrix*. Every rotation matrix R is orthogonal and satisfies the following relations

$$\begin{aligned} R^{\mathrm{T}}R &= I \\ R^{\mathrm{T}} &= R^{-1}. \end{aligned} \tag{1.5}$$

Inverting ${}^{A}_{B}R$ switches the order of its from and to frames,

$${}^{B}_{A}R = \left({}^{A}_{B}R\right)^{-1} = \left({}^{A}_{B}R\right)^{\mathrm{T}}, \tag{1.6}$$

and a similar formula applies to ${}^{B}_{A}T$,

$${}^{B}_{A}T = {}^{A}_{B}T^{-1}. \tag{1.7}$$

In the case of the full HT, however, the inverse and transpose operations are not equivalent. There is instead an explicit formula for the inverse of ${}^{A}_{B}T$,

$$\left({}^{A}_{B}T\right)^{-1} = \begin{bmatrix} & \left({}^{A}_{B}R\right)^{\mathrm{T}} & & -{}^{B}_{A}R \cdot {}^{A}P^{\circ}_{B} \\ 0 & 0 & 0 & 1 \end{bmatrix} = \begin{bmatrix} & {}^{B}_{A}R & & {}^{B}P^{\circ}_{A} \\ 0 & 0 & 0 & 1 \end{bmatrix} = {}^{B}_{A}T, \tag{1.8}$$

which may be compared with Equation 1.4. HTs may also be chained together,

$${}^{C}_{A}T = {}^{C}_{B}T \cdot {}^{B}_{A}T. \tag{1.9}$$

Here, C is a third reference frame.

The equation

$${}^{A}P_{G} = {}^{A}_{B}R \cdot {}^{B}P_{G} + {}^{A}P^{\circ}_{B} \tag{1.10}$$

is the affine form of Eqn 1.3. It produces the same result — point G in A coordinates — without the need to append an additional 1 to ${}^{B}P_{G}$. The affine form is not used much in this work, as the operations shown in Eqns 1.7 and 1.9 are inconvenient to perform when it is used. The affine form *is* helpful for expanding equations involving HTs, a purpose which

it serves well in Chapter 2.

The discussion above in Sections 1.2.5.2 and 1.2.5.3 draws from [45, pp. 23–39].

1.2.5.4 Transforming Anatomical Landmarks

The representation an AL measured with the pointing tool in the coordinates of an appropriate technical frame provides a nice application of the properties of HTs. The MPT motion capture system records the pose of each marker using a homogeneous transform that represents the marker's pose in camera coordinates (abbreviated *cam*). Suppose we are measuring the medial femoral epicondyle (MEKN) landmark; this would involve measuring both the pointing tool reference frame, abbreviated *pnt*, and the femoral technical frame, abbreviated *ft*, in camera coordinates. The system records the following point and HTs

$$ {}^{cam}_{pnt}T, \quad {}^{cam}_{ft}T, \quad {}^{pnt}P_{MEKN} = {}^{pnt}P_{tip}, \tag{1.11} $$

where an identity is assumed between the pointing tool tip and the AL of interest. Expressing the AL in coordinates of the femoral technical frame requires chaining and inverting HTs

$$ {}^{ft}P_{MEKN} = \left({}^{cam}_{ft}T\right)^{-1} \cdot {}^{cam}_{pnt}T \cdot {}^{pnt}P_{MEKN} \tag{1.12a} $$

$$ {}^{ft}P_{MEKN} = {}^{ft}_{cam}T \cdot {}^{cam}_{pnt}T \cdot {}^{pnt}P_{MEKN}. \tag{1.12b} $$

Here the MEKN landmark is measured in pointing tool coordinates, transformed into camera coordinates, and finally transformed into femoral technical frame coordinates. Equations 1.12a and 1.12b are identical, thanks to Equation 1.7.

1.2.5.5 Creating the Pelvic Anatomical Frame

An anatomical frame is constructed as a homogeneous transform in which its axes and origin are represented in the coordinates of the technical frame corresponding to the body segment in which it is embedded. For example, the pelvic anatomical frame (pa) is represented in pelvic technical frame (pt) coordinates by the homogeneous transform ${}^{pt}_{pa}T$. It is constructed similarly to ${}^{A}_{B}T$ above, but the starting point is slightly different. The pa frame begins

with four ALs measured in PT coordinates: the left and right anterior superior iliac spine landmarks (LASI, RASI) and their posterior counterparts (LPSI, RPSI).

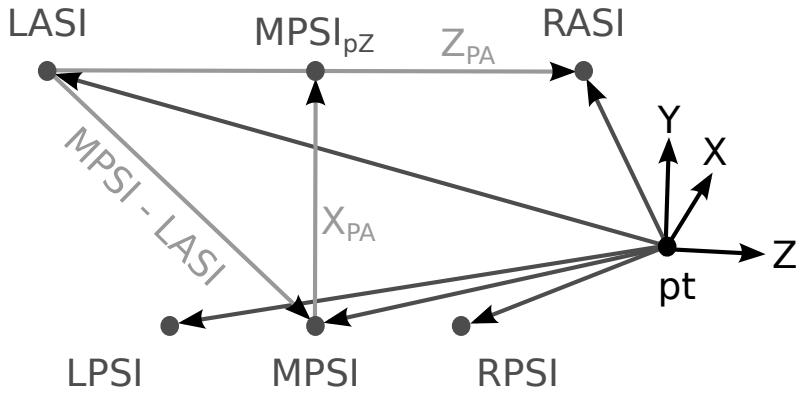

Figure 1.12: Pelvic Anatomical Frame Landmarks, Superior View

The axes of the *pa* frame are created from these four points according to the recommendations in [44]. The first recommendation is relatively simple: The Z-axis points from the LASI landmark to the RASI landmark

$$ {}^{pt}\widehat{Z}_{pa} = \left({}^{pt}P_{RASI} - {}^{pt}P_{LASI}\right) / \left\|{}^{pt}P_{RASI} - {}^{pt}P_{LASI}\right\|, \tag{1.13} $$

and this equation also normalizes the Z axis. $\|\cdot\|$ represents the 2-norm, and the hat over ${}^{pt}\widehat{Z}_{pa}$ marks it as a unit vector. The next recommendation is a little more involved; it requires the creation of the midpoint between the LPSI and RPSI landmarks, dubbed MPSI,

$$ {}^{pt}P_{MPSI} = \frac{{}^{pt}P_{LPSI} + {}^{pt}P_{RPSI}}{2}. \tag{1.14} $$

It states that the X axis lies in the plane defined by MPSI, LASI, and RASI, is orthogonal to the Z axis, and points anteriorly. All three conditions may be accomplished by defining ${}^{pt}X_{pa}$ to be the vector pointing from ${}^{pt}P_{MPSI}$ to its projection onto the Z axis, ${}^{pt}P_{MPSIpZ}$,

$$ {}^{pt}P_{MPSIpZ} = {}^{pt}P_{LASI} + {}^{pt}\widehat{Z}_{pa} \cdot \left\langle {}^{pt}P_{MPSI} - {}^{pt}P_{LASI}\,,\, {}^{pt}\widehat{Z}_{pa} \right\rangle \tag{1.15a} $$

$$ {}^{pt}\widehat{X}_{pa} = \left({}^{pt}P_{MPSIpZ} - {}^{pt}P_{MPSI}\right) / \left\|{}^{pt}P_{MPSIpZ} - {}^{pt}P_{MPSI}\right\|, \tag{1.15b} $$

and again, ${}^{pt}\widehat{X}_{pa}$ has been normalized (For projections, see [34, pp. 144–150]). ${}^{pt}\widehat{Y}_{pa}$ is given

by the cross product of the other two unit vectors,

$$ {}^{pt}\widehat{Y}_{pa} = {}^{pt}\widehat{Z}_{pa} \times {}^{pt}\widehat{X}_{pa}. \tag{1.16} $$

The last recommendation is to place the pelvic anatomical frame origin at the Hip Joint Center (HJC). The HJC is not palpable like the landmarks used to define the axes of the *pa* frame; its location may be estimated using either functional (Section 1.4) or regression (Section 1.2.5.6) methods. Whichever technique is used, the HJC location is given the symbol ${}^{pt}P_{HJC}$, leading to the full definition of the *pa* frame as a homogeneous transform

$$ {}^{pt}_{pa}T = \begin{bmatrix} | & | & | & | \\ {}^{pt}\widehat{X}_{pa} & {}^{pt}\widehat{Y}_{pa} & {}^{pt}\widehat{Z}_{pa} & {}^{pt}P_{HJC} \\ | & | & | & | \\ 0 & 0 & 0 & 1 \end{bmatrix}. \tag{1.17} $$

It can be thought of as the pose of the pelvic bone in the hip marker reference frame.

1.2.5.6 Regression Methods for HJC Estimation

Regression methods are so called because they use quantities derived from the anatomical landmarks as independent variables in a set of statistical regression equations which output an estimated HJC location. The regression method of Harrington, et al. [18] is given by the equations below,

$$ PW = \|{}^{pt}P_{RASI} - {}^{pt}P_{LASI}\| \tag{1.18a} $$

$$ {}^{pt}P_{MASI} = \frac{{}^{pt}P_{RASI} + {}^{pt}P_{LASI}}{2} \tag{1.18b} $$

$$ PD = \|{}^{pt}P_{MASI} - {}^{pt}P_{MPSI}\| \tag{1.18c} $$

$$ {}^{paC}P_{HJC}(x) = -0.24 \cdot PD - 9.9 \tag{1.18d} $$

$$ {}^{paC}P_{HJC}(y) = -0.30 \cdot PW - 10.9 \tag{1.18e} $$

$$ {}^{paC}P_{HJC}(z) = 0.33 \cdot PW + 7.3, \tag{1.18f} $$

where PW stands for Pelvic Width, PD stands for Pelvic Depth, and ${}^{pt}P_{MASI}$ is the midpoint of the RASI and LASI ALs. Eqns 1.18d, 1.18e, and 1.18f perform the regression itself, yielding an estimate of the HJC location in the paC frame, which is the pelvic anatomical frame specified by Cappozzo, et al. [6]. The paC frame differs from the pa frame defined in Section 1.2.5.5 in only one particular: Its origin is placed at ${}^{pt}P_{MASI}$. This frame is defined by the transform

$$ {}^{pt}_{paC}T = \begin{bmatrix} | & | & | & | \\ {}^{pt}\widehat{X}_{pa} & {}^{pt}\widehat{Y}_{pa} & {}^{pt}\widehat{Z}_{pa} & {}^{pt}P_{MASI} \\ | & | & | & | \\ 0 & 0 & 0 & 1 \end{bmatrix}, \tag{1.19} $$

which can transform the HJC estimate obtained by regression into pt coordinates:

$$ {}^{pt}P_{HJC} = {}^{pt}_{paC}T \cdot {}^{paC}P_{HJC}. \tag{1.20} $$

The regression equations above were derived from MRI measurements of the HJC and pelvic ALs in a cohort of 32 subjects including adults, healthy children, and children with cerebral palsy [18]. Clinical Leg Length (LL) was also measured. Multiple linear regression was performed to determine which combination of the PD, PW, and LL variables best predicted HJC location in the anteroposterior (Eqn 1.18d), superior/inferior (Eqn 1.18e), and mediolateral (Eqn 1.18f) directions, as determined by the R^2 coefficient and F-statistic. Another set of equations which includes LL was also presented in [18], but the set in Eqns 1.18d, 1.18e, and 1.18f was finally recommended due to the poor reliability of measuring LL in practice. The regression described by these equations is meant to be applied to the right hip.

There are two main drawbacks to regression methods. First, they rely on accurate palpitation of pelvic (and sometimes other) landmarks, introducing the potential for operator

error. Second, they are not subject specific, as the regression equations are derived from measurements performed on a small group of people. HJC location estimates calculated using the earlier regression methods of Bell, et al. [3] and Davis, et al. [9] were shown to have mean errors of 23mm and 29mm, respectively, relative to the "true" HJC location determined by Roentgen Stereophotogrammetry [21]. These errors are large enough to significantly affect the calculation of moments at the hip when inverse kinetics is performed [33]. Harrington's regression has demonstrated improved accuracy; HJC estimates made using the set of equations incorporating leg length were found to have a mean a mean error of 16mm relative to 3D ultrasound determination of the HJC, which is competitive with the best functional methods [27]. Unlike functional methods, regression methods rely solely on AL data which is routinely collected during gait analysis and do not require the subject to perform any additional movements. On the other hand, AL palpitation can be difficult if the landmarks are covered by a sufficient quantity of tissue.

1.2.5.7 Other Anatomical Frames

The pelvic anatomical frame has been defined, but in order to analyze joint motion at the hip and knee, the femoral and tibial anatomical frames, *fa* and *ta*, must also be defined. That is the purpose of this section, which is based on the frame definitions found in [28] and [17]. The *fa* and *ta* frames will be used in Section 1.2.6, and they are shown in Figure 1.13 along with the other technical and anatomical frames tracked in the course of analyzing the hip and knee joints.

The femoral anatomical frame, *fa*, has its origin at the midpoint between the MEKN and LAKN landmarks. Its Y axis points toward the center of the femoral head. Its Z axis points to the right and aligns with the line connecting the MEKN and LAKN landmarks subject to the constraint that it remains orthogonal to the Y axis. The X axis is mutually orthogonal to the Y and Z axes.

The tibial anatomical frame, *ta*, requires the introduction of two new landmarks. MC and LC are the most medial and lateral points on the rim of the tibial condyle; IC denotes their midpoint and serves as the origin of the *ta* frame. The Y axis of the *ta* frame is parallel to the vector connecting the midpoint of the MEMA and LAMA landmarks (the Ankle Joint

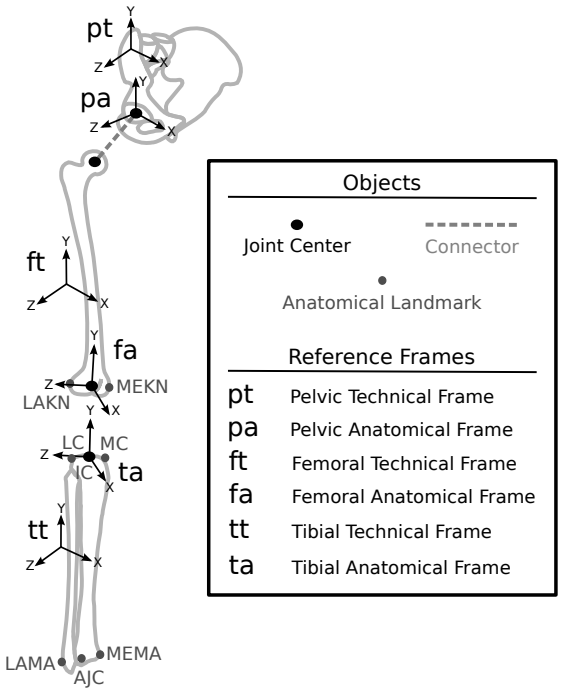

Figure 1.13: Technical and Anatomical Reference Frames

Center) to the IC landmark. The Z axis of the *ta* frame is made to align with the Z axis of the *fa* frame when the subject is standing with the knee fully extended, subject to the constraint that it remains orthogonal to the Y axis. The X axis is the cross product of the Y and Z axes and points anteriorly.

1.2.6 Quantifying Joint Motion

An earlier section (1.2.3) defined qualitative terms (adduction, flexion, etc.) for describing the variety of postures permitted by our joints. These terms correspond to the relative orientation of adjacent bones, which in turn is quantifiable thanks to the anatomical frames and the motion capture system. There is, however, one more hurdle to jump. Currently, the relative orientation of the femur and tibia is given by the 3x3 rotation matrix between the femoral and tibial anatomical frames, ${}^{ta}_{fa}R$, which may be difficult to interpret. Since the motion of a joint is quantified by a series of such matrices, it may also be impossible to graph. A new convention for representing orientation can help overcome these difficulties.

Cardan angles represent a rotation between reference frames using three angular values which correspond to a sequence of elemental rotations about a defined set of axes [36].

When the sequence of elemental rotations is properly defined for a given joint, the Cardan angles correspond to flexion/extension (FL/EX), adduction/abduction (AD/AB), and internal/external rotation (IN/EX) [17]. They are physiologically relevant, quantitative, and easy to plot [45, pp. 60–61].

This section begins by constructing a rotation between two reference frames from three Cardan angles. It proceeds to develop a formula for extracting Cardan angles from any rotation matrix. Next, these techniques are applied to the knee, showing how its joint angles may be derived from ${}^{ta}_{fa}R$. Finally joint angles are plotted for a specific movement of the hip.

1.2.6.1 Cardan Angles and Rotation Matrices

Figure 1.14 shows the rotation from frame A to frame D as a series of Cardanic rotations, labelled by the Cardan angles E_X, E_Y, and E_Z. It also shows the intermediate coordinate frames (labelled B and C) created by these rotations.

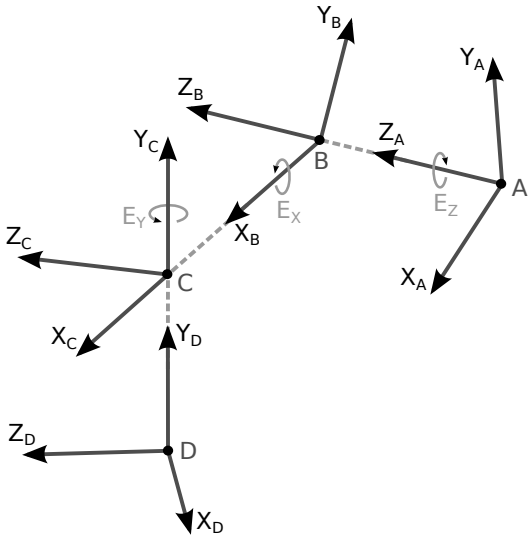

Figure 1.14: Rotation from frame A to frame D in three steps.

The sequence in which the rotations occur is important. In Figure 1.14, the sequence is Z-X-Y, indicating that E_Z occurs about the Z axis of the initial frame (A), E_X occurs about the X axis of the intermediate frame (B), and E_Y occurs about the Y axis of the final frame (D). Note that frames C and D share a Y axis. If an X-Y-Z sequence were used, E_X would

occur about the X axis of frame A, producing a very different B frame, call it B′. E_Y would then occur about the Y axis of frame B′, and E_Z would occur about the Z axis of frame D. The rotation from frame A to frame D would still occur, but the rotations would take quite different values. For the Z-X-Y sequence shown in Figure 1.14, $E_X = 10°$, $E_Y = 25°$, and $E_Z = 30°$. For the X-Y-Z sequence (not pictured), $E_X = -5.03°$, $E_Y = 29.09°$, and $E_Z = 31.11°$.

Note the negative sign on the value for E_X in the X-Y-Z sequence. A rotation about an axis may be either positive or negative. Positive rotation is in the direction that the fingers of the right hand curl when the right thumb points in the same direction as the axis about which rotation occurs. This is also called a counterclockwise rotation. Negative rotation is in the opposite direction. The light gray arrows indicating rotation in Figure 1.14 all point in the direction of positive rotation.

The X axis of frame B has an interesting property: It is mutually orthogonal to the Z axis of frame A and the Y axis of frame C. By extension, it is also orthogonal to the Y axis of frame D. As a result, the Z-X-Y sequence rotation from frame A to frame D may be described as occuring about the Z axis of frame A, the Y axis of frame D, and the axis which is mutually orthogonal to both of them. This description is convenient because it does not mention the intermediate frames.

The three Cardanic rotations may be constructed as rotation matrices, each of which performs a rotation about a single axis. The form of these matrices depends only on the axis, not on the sequence. Rotation about an X axis is performed by the rotation matrix R_X,

$$R_X = \begin{bmatrix} 1 & 0 & 0 \\ 0 & C_X & S_X \\ 0 & -S_X & C_X \end{bmatrix}, \tag{1.21}$$

where C_X abbreviates $\cos(E_X)$, and S_X abbreviates $\sin(E_X)$. The Cardan angles are labelled with the letter E to avoid confusion with these terms and because they are sometimes

called Euler angles. R_Y and R_Z perform rotations about a Y axis and a Z axis, respectively

$$R_Y = \begin{bmatrix} C_Y & 0 & -S_Y \\ 0 & 1 & 0 \\ S_Y & 0 & C_Y \end{bmatrix} \qquad R_Z = \begin{bmatrix} C_Z & S_Z & 0 \\ -S_Z & C_Z & 0 \\ 0 & 0 & 1 \end{bmatrix}. \tag{1.22}$$

Here, C_Y and S_Y are the cosine and sine of E_Y, while C_Z and S_Z are the cosine and sine of E_Z.

The sequence of rotations comes into play when R_X, R_Y, and R_Z are multiplied to form the rotation from frame A to frame D,

$$\begin{matrix} D \\ A \end{matrix} R = R_Y \cdot R_X \cdot R_Z = \begin{bmatrix} C_Z C_Y - S_Z S_Y S_X & S_Z C_Y + C_Z S_Y S_X & -S_Y C_X \\ -S_Z C_X & C_Z C_X & S_X \\ C_Z S_Y + S_Z C_Y S_X & S_Z S_Y - C_Z C_Y S_X & C_Y C_X \end{bmatrix}, \tag{1.23}$$

where the Z-X-Y sequence has been used. Now that the form of Equation 1.23 is known, it is possible to use trigonometry to recover the Cardan angles from the rotation matrix.

The easiest angle to recover is E_X since the matrix element $\begin{matrix} D \\ A \end{matrix} R(2,3)$ is S_X, which expands to $\sin(E_X)$. Taking the arcsine of this term will yield E_X. The equations for all three Cardan angles follow

$$\begin{aligned} E_X &= \operatorname{asin}\left(\begin{matrix} D \\ A \end{matrix} R(2,3) \right) \\ E_Y &= \operatorname{atan2}\left(-\begin{matrix} D \\ A \end{matrix} R(1,3), \begin{matrix} D \\ A \end{matrix} R(3,3) \right) \\ E_Z &= \operatorname{atan2}\left(-\begin{matrix} D \\ A \end{matrix} R(2,1), \begin{matrix} D \\ A \end{matrix} R(2,2) \right). \end{aligned} \tag{1.24}$$

Equations like these are used to recover the joint angles from motion capture data.

If the X-Y-Z sequence is used, the resultant rotation from frame A to frame D is written

$$ {}^{D}_{A}R = R_Z \cdot R_Y \cdot R_X = \begin{bmatrix} C_Z C_Y & C_Z S_X S_Y + S_Z C_X & -C_Z S_Y C_X + S_Z S_X \\ -S_Z C_Y & -S_Z S_X S_Y + C_Z C_X & S_Z S_Y C_X + C_Z S_X \\ S_Y & -S_X C_Y & C_X C_Y, \end{bmatrix} \tag{1.25} $$

which is quite different from Equation 1.23. Sequence makes a difference because matrix multiplication, in general, does not commute. Eqns 1.23 and 1.25 produce the same ${}^{D}_{A}R$ matrix, but the values of E_X, E_Y, and E_Z will differ between the two sequences.

1.2.6.2 Application to the Knee

The goal in applying Cardan rotations to the knee is to find the sequence for which the rotations correspond in behavior to the joint angles. That is, each of E_X, E_Y, and E_Z should correspond to one of Flexion/Extension (FL/EX), Adduction/Abduction (AD/AB), and Internal/External Rotation (IN/EX). These angles are extracted from the rotation matrix ${}^{ta}_{fa}R$, which is the rotation from femoral anatomical (fa) coordinates to tibial anatomical (ta) coordinates. The use of ${}^{ta}_{fa}R$ instead of ${}^{fa}_{ta}R$ ensures the rotations proceed from proximal to distal across the joint, and it entails that the first rotation occurs about one of the axes of the fa frame.

Figure 1.15 shows the femur and tibia, their anatomical frames, the rotation axes for the Cardan sequence used at the knee, and their corresponding joint angles. It lists the Z axis of fa (Z_{fa}) as the first rotation axis, corresponding to FL/EX. Why not use X_{fa} or Y_{fa} as the axis first rotation? When the knee is in full extension, as in Figure 1.15, rotation about X_{fa} would correspond to AD/AB, and rotation about Y_{fa} would correspond to IN/EX. However, when the knee is flexed to 90°, rotation about X_{fa} would correspond to IN/EX, and rotation about the Y_{fa} would correspond to negative AD/AB. Intermediate values of knee flexion would cause these rotations to correspond proportionally more or less to one of AD/AB or IN/EX — a nightmare to interpret. Rotation about the Z axis of fa consistently corresponds to FL/EX and is the logical choice by exclusion.

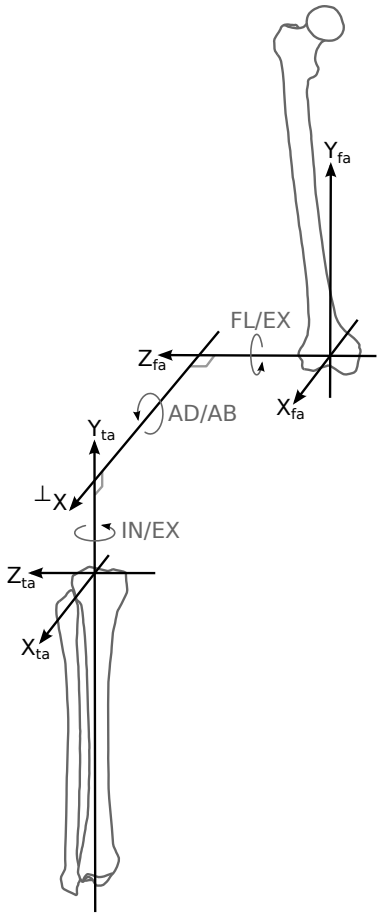

Figure 1.15: Cardan angles of the Z-X-Y sequence result in the joint angles when applied to the knee.

It is more difficult to make such a case for the remaining rotations. Figure 1.15 shows IN/EX occuring about the Y axis of ta, which makes physiological sense, as this is the proximal-distal axis of the tibia. AD/AB is shown occuring about the axis mutually orthogonal to Z_{fa} and Y_{ta}, labelled ${}^{\perp}X$. Because Z_{fa} maintains a medio-lateral orientation throughout flexion and Y_{ta} maintains a proximal-distal orientation throughout internal rotation, ${}^{\perp}X$ will maintain align with the anterior-posterior axis. This is the axis of rotation desired for AD/AB, and the sequence just described is the Z-X-Y sequence.

What about the Z-Y-X sequence? It specifies AD/AB as occuring about X_{ta}, which works physiologically. It also specifies IN/EX as occuring about the axis mutually perpendicular to X_{ta} and Z_{fa}; this axis would take on a proximal-distal orientation, as desired for the axis of IN/EX rotation. This sequence also makes physiological sense, and both the

Z-X-Y and Z-Y-X sequences have been used to describe the motion of the knee joint [8].

This work uses the Z-X-Y sequence for the knee, on the recommendation of [17]. Z-X-Y is also used at the hip, on the recommendation of [44]. Another paper has recommended the Z-X-Y sequence for both the hip and knee, based on their favorable performance in the analysis of a fencing lunge [31].

With the sequence determined, the joint angles for the knee may be extracted from ${}^{ta}_{fa}R$ using Equation 1.24. Similarly, the joint angles for the knee may be extracted from ${}^{fa}_{pa}R$ using the same equation. ${}^{fa}_{pa}R$ is the rotation from pelvic anatomical (pa) to fa coordinates. In both cases, E_Z corresponds to FL/EX, E_X corresponds to AD/AB, and E_Y corresponds to IN/EX.

1.2.6.3 Gimbal Lock

If the second in a series of Cardanic rotations has value $\pm 90°$, the first and third rotation will occur about an identical axis, and one degree of freedom will be lost. In the case of the Z-X-Y sequence, this occurs when $E_X = \pm 90°$, which orients the Y axis of the final frame so that it is coincident with the Z axis of the initial frame. This makes it impossible to distinguish the action of E_Y and E_Z, a point which becomes apparent if one forms the overall rotation matrix from the Cardan angles

$$R = R_Y \cdot R_X(90°) \cdot R_Z = \begin{bmatrix} C_Z C_Y - S_Z S_Y & S_Z C_Y + C_Z S_Y & 0 \\ 0 & 0 & 1 \\ C_Z S_Y + S_Z C_Y & S_Z S_Y - C_Z C_Y & 0 \end{bmatrix}. \tag{1.26}$$

This rotation matrix resolves by trigonometric identity to

$$R = \begin{bmatrix} \cos(E_Y + E_Z) & \sin(E_Y + E_Z) & 0 \\ 0 & 0 & 1 \\ \sin(E_Y + E_Z) & -\cos(E_Y + E_Z) & 0 \end{bmatrix}, \tag{1.27}$$

where the identities

$$\begin{aligned} \sin(\alpha+\beta) &= \sin(\alpha)\cos(\beta)+\cos(\alpha)\sin(\beta) \\ \cos(\alpha+\beta) &= \cos(\alpha)\cos(\beta)-\sin(\alpha)\sin(\beta) \end{aligned} \tag{1.28}$$

have been used [1, pg. 72].

Gimbal lock should be avoided, as it makes recovery of the true joint angles impossible. Fortunately, a healthy human being cannot attain ninety degrees of adduction or abduction at either the hip or the knee. Barring some error in reference frame definition or in data collection more generally, gimbal lock should not occur when applying the Z-X-Y sequence to the hip and knee.

1.2.6.4 Plotting Movement Data

The joint angles are amenable to plotting; they are scalar values which vary in time and remain within reasonable ranges. Furthermore, a plot of the joint angles for a particular movement gives the reader a sense of what that movement would look like. This section provides an opportunity to compare a plot of joint angles for the Star Arc movement (Figure 1.17) with a diagram illustrating its execution (Figure 1.16). The Star Arc movement is developed in [5].

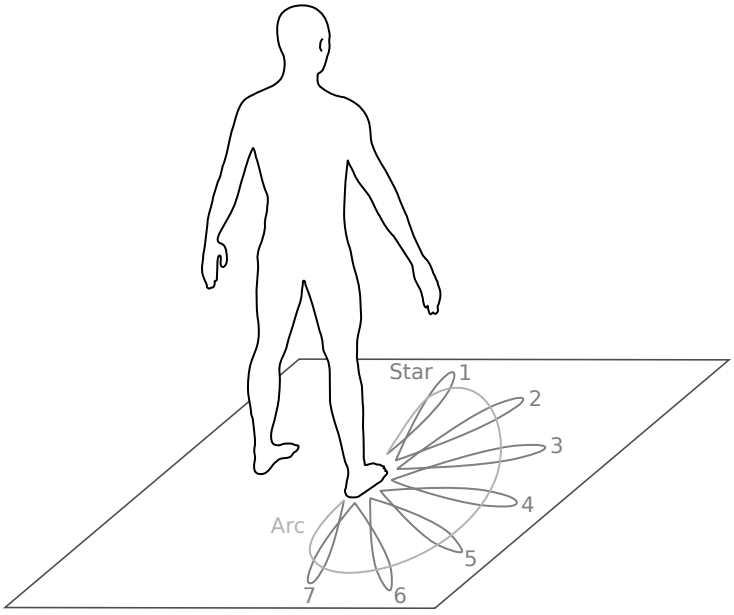

Figure 1.16: Path traced by right foot during Star Arc movement. The star has seven lobes; the arc is a circumduction of the hip.

The Star Arc movement is used as an input for functional methods which identify the Hip Joint Center (HJC); one such method is shown in Section 1.4. Functional methods start with measured movement data and work backwards to estimate some property of the joint which produced the data, in this case, the location of the HJC. The star arc movement was designed to excercise the hip through a variety of configurations so that the functional methods will have a rich data set to work from [5]. The "star" part of the star arc has seven lobes, which are labelled in Figure 1.16. The first lobe involves flexion of the hip and return to stance, while the fourth involves abduction of the hip and return to stance. Lobes two and three are gradations between one and four, with decreasing flexion and increasing abduction. Lobes five, six, and seven are mirrors of one, two, and three, with the seventh lobe involving extension and return to stance. The "arc" portion of the movement is a circumduction — a combination of FL/EX and AD/AB which produces a circular motion.

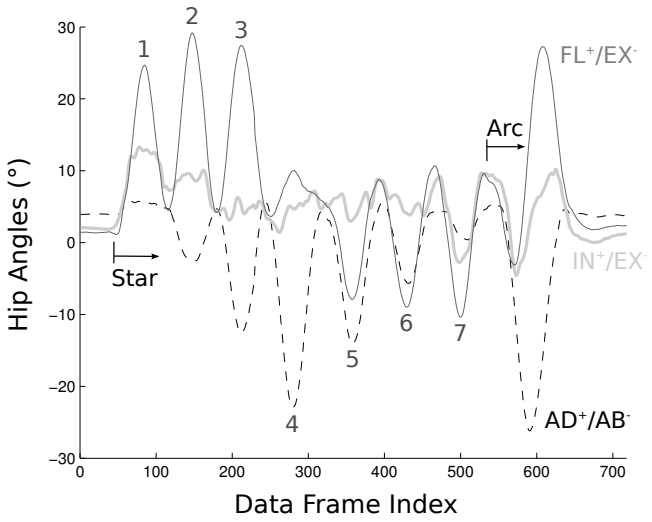

Figure 1.17: Hip Angles for the Star Arc Movement: FL^+/EX^- (gray), IN^+/EX^- (light gray), and AD^+/AB^- (dashed). The data frame index marks time — each frame lasts 1/60 seconds.

Figure 1.17 shows a plot of the joint angles for the hip which were measured during a star arc movement. Angular peaks are marked corresponding to the lobe where they were produced. The peaks in FL/EX do not show the expected steadily-decreasing pattern for lobes 1, 2, and 3. They do behave as expected for lobe 4 — minimal flexion — as well as for lobes 5, 6, and 7, where an increasing pattern is observed. Also note the sign change

between lobes 4 and 5, where the movement switches from flexion (positive) to extension (negative). The peaks in AD/AB are just as expected; they increase to a maximum at lobe 4 and steadily decrease to the end of the star movement. The large movement between lobe 7 and the end of the data is the arc movement. The FL/EX curve for this movement is a lopsided sinusoidal; it begins with extension, switches to flexion, and ends with extension returning to stance. This is consistent with an arc movement proceeding from back to front. AD/AB shows a single peak in abduction during the arc, as expected.

The IN/EX curve is not very descriptive of the star arc movement; it simply records how much the subject's leg twists during the movement.

In Figure 1.17, the joint angles are plotted against the Data Frame Index, a measure of time. The motion capture system's camera works like a movie camera: It captures motion by taking still snapshots or frames at a high rate. In this case, the rate is 60 frames per second. Each snapshot or frame records the pose of all markers visible to the camera at that instant; the collection of these poses is called a data frame or frame of data, to distinguish it from the reference frames. The data frame index is a simple counter that marks the order of the frames: 1st, 2nd, ..., 718th. The data could also be plotted against time, in this case, zero to 11.97 seconds.

1.2.7 Summary

The most important part of this section is the process of using motion capture technology to record human movement. Motion tracking markers are placed over the skin on each body segment under study; the motion capture system resolves a technical frame for each marker in every frame of motion capture data. For each body segment, an anatomical frame is constructed using anatomical landmarks which defines the pose of the underlying bone in the coordinates of the technical frame. Joint angles are recovered by calculating the rotation matrix between anatomical frames on either side of a joint and decomposing the rotation matrix into Cardan angles of the appropriate sequence. The end result is a quantitative description of joint motion which is amenable to graphical representation and human interpretation.

1.3 Background in Parameter Estimation

1.3.1 Linear Least Squares: An Example

Parameter estimation is an important mathematical tool which will be described through the following example. It is typical to see a relation of the form

$$y = f(x), \tag{1.29}$$

where the function $f()$ relates the dependent variable y to the independent variable x. Now, give $f()$ the form

$$y = f(x; g, h, v) = h + v \cdot x - \frac{g}{2} \cdot x^2, \tag{1.30}$$

where h, v, and g are unknown constants called *parameters*. This is the equation for the vertical position, y (m), of a projectile at time x (s), subject to initial height h (m), initial velocity v ($\frac{\text{m}}{\text{s}}$), and gravitational constant g ($\frac{\text{m}}{\text{s}^2}$). Suppose we are given data from a ball drop experiment,

$$\begin{aligned} x_1 &= 1.0000s \quad y_1 = 29.9720m \\ x_2 &= 2.0000s \quad y_2 = 24.3944m \\ x_3 &= 3.0000s \quad y_3 = 15.1640m \\ x_4 &= 4.0000s \quad y_4 = 2.1590m, \end{aligned} \tag{1.31}$$

and asked to find the parameters of f which most closely approximate the dependent variables $(y_i, i = 1 \ldots 4)$ given the independent variables $(x_i, i = 1 \ldots 4)$. We are assured that the time points in the data are highly accurate and cautioned that the position measurements contain small errors.

This problem is a parameter estimation problem. In this case, it amounts to solving four

equations for three parameters,

$$\begin{bmatrix} 1 & x_1 & -\frac{1}{2}x_1^2 \\ 1 & x_2 & -\frac{1}{2}x_2^2 \\ 1 & x_3 & -\frac{1}{2}x_3^2 \\ 1 & x_4 & -\frac{1}{2}x_4^2 \end{bmatrix} \begin{bmatrix} h \\ v \\ g \end{bmatrix} = \begin{bmatrix} y_1 \\ y_2 \\ y_3 \\ y_4 \end{bmatrix}, \tag{1.32}$$

and the equations are linear in the parameters. The left side matrix multiplies the *parameter vector*, and the vector containing the dependent variables is called the *data vector*. For the sake of brevity, these are given the symbols $\mathbf{A}$, $\boldsymbol{u}$, and $\boldsymbol{y}$, respectively. Because there are more equations than unknowns, Equation 1.32 is an overdetermined linear system and is therefore unlikely to have an exact solution.

Instead, we may solve for an approximate solution $\widehat{\boldsymbol{u}}$ which satisfies

$$\min_u \|\mathbf{A}\boldsymbol{u} - \boldsymbol{y}\|^2. \tag{1.33}$$

$\widehat{\boldsymbol{u}}$ is called the *least squares solution* to Equation 1.33 because it minimizes the sum of squares of the *residual vector* $\boldsymbol{r}$,

$$\begin{aligned} \mathbf{A}\boldsymbol{u} &= \boldsymbol{b} \\ \boldsymbol{r} &= \mathbf{A}\boldsymbol{u} - \boldsymbol{y} = \boldsymbol{b} - \boldsymbol{y}. \end{aligned} \tag{1.34}$$

Since any *approximate data vector* $\boldsymbol{b}$ is a linear combination of the columns of $\mathbf{A}$, it lies in the column space of $\mathbf{A}$. The $\boldsymbol{b}$ vector which minimizes $\|\boldsymbol{r}\|^2 = \|\boldsymbol{b} - \boldsymbol{y}\|^2$ is therefore the projection of $\boldsymbol{y}$ onto the column space of $\mathbf{A}$, given by

$$\widehat{\boldsymbol{b}} = \mathbf{A}(\mathbf{A}^{\mathrm{T}}\mathbf{A})^{-1}\mathbf{A}^{\mathrm{T}}\boldsymbol{y}, \tag{1.35}$$

where the hat over $\widehat{\boldsymbol{b}}$ marks it as corresponding to the least squares solution to Equation 1.33. Since $\boldsymbol{b} = \mathbf{A}\boldsymbol{u}$, the $\boldsymbol{u}$ vector which minimizes $\|\boldsymbol{r}\|^2$ is given by

$$\widehat{\boldsymbol{u}} = (\mathbf{A}^{\mathrm{T}}\mathbf{A})^{-1}\mathbf{A}^{\mathrm{T}}\,\boldsymbol{y}. \tag{1.36}$$

Equation 1.36 is a solution to the *normal equations,*

$$\mathbf{A}^{\mathrm{T}}\mathbf{A}\widehat{\boldsymbol{u}} = \mathbf{A}^{\mathrm{T}}\boldsymbol{y}, \tag{1.37}$$

which exists when $\mathbf{A}$ is of full column rank; otherwise, $\mathbf{A}^{\mathrm{T}}\mathbf{A}$ is not invertible.

The discussion above follows [2, pp. 15–16] and [34, pp. 154–158].

We now have a way to analyze the ball drop experiment. The $\mathbf{A}$ matrix is given by

$$\begin{bmatrix} 1 & 1 & -\frac{1}{2} \\ 1 & 2 & -2 \\ 1 & 3 & -4\frac{1}{2} \\ 1 & 4 & -8 \end{bmatrix}, \tag{1.38}$$

and $\widehat{\boldsymbol{u}}$ is given by

$$\begin{bmatrix} 31.8054 \\ 0.0173 \\ 3.7137 \end{bmatrix} = \begin{bmatrix} 7\frac{3}{4} & -6\frac{3}{4} & -2\frac{1}{2} \\ -6\frac{3}{4} & 6\frac{9}{20} & 2\frac{1}{2} \\ -2\frac{1}{2} & 2\frac{1}{2} & 1 \end{bmatrix} \begin{bmatrix} 1 & 1 & 1 & 1 \\ 1 & 2 & 3 & 4 \\ -\frac{1}{2} & -2 & -4\frac{1}{2} & -8 \end{bmatrix} \begin{bmatrix} 29.9720 \\ 24.3944 \\ 15.1640 \\ 2.1590 \end{bmatrix}, \tag{1.39}$$

which is Equation 1.36 writ large. This yields the parameter estimates $h = 31.8054\,(\mathrm{m}),\ v = 0.0173\ (\frac{\mathrm{m}}{\mathrm{s}}),\ g = 3.7137\ (\frac{\mathrm{m}}{\mathrm{s}^2})$. From this we may conclude that the ball was dropped with small initial velocity from a height of about 32 meters on the planet Mars, which has a gravitational constant of 3.7 $\frac{\mathrm{m}}{\mathrm{s}^2}$ [15]. The residual vector and its norm will give a clue as to how close this solution is to the measured data,

$$\widehat{\boldsymbol{y}} = \begin{bmatrix} 29.9659 \\ 24.4127 \\ 15.1457 \\ 2.1651 \end{bmatrix} \qquad \boldsymbol{r} = \begin{bmatrix} -0.0061 \\ 0.0183 \\ -0.0183 \\ 0.0061 \end{bmatrix} \qquad \|\boldsymbol{r}\| = 0.0272, \tag{1.40}$$

and a residual of 2.7cm on data ranging from 2m to 30m seems pretty good. In fact, the

data of Equation 1.31 were generated according to

$$\begin{aligned} x_i &= i \\ y_i &= 31.8 - \frac{3.7}{2}x_i^2 + \epsilon_i \\ i &= 1, 2, 3, 4, \end{aligned} \tag{1.41}$$

where ϵ_i is an error term that is normally distributed with $\mu = 0$ and $\sigma = 2$cm. The least squares solution $\widehat{\boldsymbol{u}}$ differs from the true solution $\boldsymbol{u}^*$

$$\widehat{\boldsymbol{u}} - \boldsymbol{u}^* = \begin{bmatrix} 31.8054 \\ 0.0173 \\ 3.7137 \end{bmatrix} - \begin{bmatrix} 31.8 \\ 0 \\ 3.7 \end{bmatrix} = \begin{bmatrix} 0.0054 \\ 0.0173 \\ 0.0137 \end{bmatrix} \tag{1.42}$$

by only a small amount.

1.3.1.1 Summary

Parameter estimation is a mathematical tool which allows one to estimate the unknown constants (parameters) of a function whose form is otherwise known, given a quantity of observations which is greater than the number of parameters. Each observation pairs a value of the independent variable(s) of the function with a measured data point. The goal is to find the parameters which cause the function to most closely approximate the observed data, or equivalently, which minimize the residual.

1.3.2 Nonlinear Estimation

While linear least squares does find applications in biomechanics (See Section 1.4), many interesting phenomena are nonlinear in the parameters, including the movements of general kinematic models [32]. Nonlinear parameter estimation bears many similarities to linear

parameter estimation. It begins with a nonlinear function $f()$,

$$\begin{aligned} f_i(\boldsymbol{u}) &= f(\boldsymbol{x}_i; \boldsymbol{u}) \\ \boldsymbol{f}(\boldsymbol{u}) &= [f_1(\boldsymbol{u}), f_2(\boldsymbol{u}), \ldots, f_n(\boldsymbol{u})]^T \\ r_i(\boldsymbol{u}) &= f_i(\boldsymbol{u}) - y_i \\ i &= 1, 2, \ldots, n \\ \boldsymbol{u} &\in \mathbb{R}^p,\ \boldsymbol{x}_i \in \mathbb{R}^k \end{aligned} \tag{1.43}$$

dependent on the k independent variables in $\boldsymbol{x}$ and the p parameters in $\boldsymbol{u}$. The n-observation residual vector $\boldsymbol{r}$ is the difference between the vector of function values and the data vector $\boldsymbol{y}$, and the residual, $S()$, is composed of the sum of squares of the residual vector,

$$S(\boldsymbol{u}) = \sum_i r_i(\boldsymbol{u})^2. \tag{1.44}$$

We seek a solution $\widehat{\boldsymbol{u}}$ which minimizes Equation 1.44, this time using an iterative approach.

1.3.2.1 Iterative Solution to Nonlinear Least Squares

Given an estimate $\boldsymbol{u}^{(j)}$ of $\widehat{\boldsymbol{u}}$, the function $S()$ in the vicinity of $\boldsymbol{u}^{(j)}$ may be approximated by the second-order Taylor expansion,

$$\begin{aligned} &S(\boldsymbol{u}^{(j)} + \boldsymbol{\delta}) \approx S(\boldsymbol{u}^{(j)}) + \boldsymbol{\delta}^{\mathrm{T}} \nabla S(\boldsymbol{u}^{(j)}) + \frac{1}{2} \boldsymbol{\delta}^{\mathrm{T}} \nabla^2 S(\boldsymbol{u}^{(j)}) \boldsymbol{\delta} \\ &\boldsymbol{\delta} \in \mathbb{R}^p, \end{aligned} \tag{1.45}$$

where $\nabla S(\boldsymbol{u}^{(j)})$ is the *gradient* of $S(\boldsymbol{u}^{(j)})$,

$$\nabla S(\boldsymbol{u}^{(j)}) = \begin{bmatrix} \frac{\partial S}{\partial u_1^{(j)}} \\ \frac{\partial S}{\partial u_2^{(j)}} \\ \vdots \\ \frac{\partial S}{\partial u_p^{(j)}} \end{bmatrix} = \mathbf{J}(\boldsymbol{u}^{(j)})^{\mathrm{T}} \boldsymbol{r}(\boldsymbol{u}^{(j)}). \tag{1.46}$$

The *Jacobian*

$$\mathbf{J}(\boldsymbol{u}^{(j)}) = \begin{bmatrix} \frac{\partial r_1(\boldsymbol{u}^{(j)})}{\partial u_1^{(j)}} & \cdots & \frac{\partial r_1(\boldsymbol{u}^{(j)})}{\partial u_p^{(j)}} \\ \vdots & \ddots & \vdots \\ \frac{\partial r_n(\boldsymbol{u}^{(j)})}{\partial u_1^{(j)}} & \cdots & \frac{\partial r_n(\boldsymbol{u}^{(j)})}{\partial u_p^{(j)}} \end{bmatrix} \tag{1.47}$$

allows the gradient of $S()$ to be written in terms of $f()$. Since $\boldsymbol{y}$ is constant, $\frac{\partial r_i(\boldsymbol{u})}{\partial u_l} = \frac{\partial f_i(\boldsymbol{u})}{\partial u_l}$ (See Equation 1.43). Returning to Equation 1.45, $\nabla^2 S(\boldsymbol{u}^{(j)})$ denotes the *Hessian* of $S(\boldsymbol{u}^{(j)})$

$$\nabla^2 S(\boldsymbol{u}^{(j)}) = \begin{bmatrix} \frac{\partial^2 S(\boldsymbol{u}^{(j)})}{\partial u_1^{(j)} \partial u_1^{(j)}} & \cdots & \frac{\partial^2 S(\boldsymbol{u}^{(j)})}{\partial u_1^{(j)} \partial u_p^{(j)}} \\ \vdots & \ddots & \vdots \\ \frac{\partial^2 S(\boldsymbol{u}^{(j)})}{\partial u_p^{(j)} \partial u_1^{(j)}} & \cdots & \frac{\partial^2 S(\boldsymbol{u}^{(j)})}{\partial u_p^{(j)} \partial u_p^{(j)}} \end{bmatrix} = \mathbf{J}(\boldsymbol{u}^{(j)})^{\mathrm{T}} \mathbf{J}(\boldsymbol{u}^{(j)}) + \mathbf{G}(\boldsymbol{u}^{(j)}), \tag{1.48}$$

and the matrix $\mathbf{G}(\boldsymbol{u}^{(j)})$

$$\mathbf{G}(\boldsymbol{u}^{(j)}) = \sum_{i=1}^{n} r_i(\boldsymbol{u}^{(j)}) \nabla^2 r_i(\boldsymbol{u}^{(j)}), \tag{1.49}$$

along with $\mathbf{J}(\boldsymbol{u}^{(j)})$, allow $\nabla^2 S(\boldsymbol{u}^{(j)})$ to be written in terms of $\boldsymbol{f}()$ and $\boldsymbol{r}$.

The vector $\boldsymbol{\delta}$ is called the *update*, for reasons which will soon become clear. The goal is to choose $\boldsymbol{\delta}$ such that the Taylor expansion of $S(\boldsymbol{u}^{(j)} + \boldsymbol{\delta})$ in Equation 1.45 is minimized or at least reduced relative to $S(\boldsymbol{u}^{(j)})$. The Newton step

$$\begin{aligned} \boldsymbol{\delta}_N^{(j)} &= -\left(\nabla^2 S(\boldsymbol{u}^{(j)})\right)^{-1} \nabla S(\boldsymbol{u}^{(j)}) \\ &= -\left(\mathbf{J}(\boldsymbol{u}^{(j)})^{\mathrm{T}} \mathbf{J}(\boldsymbol{u}^{(j)}) + \mathbf{G}(\boldsymbol{u}^{(j)})\right)^{-1} \mathbf{J}(\boldsymbol{u}^{(j)})^{\mathrm{T}} \boldsymbol{r}(\boldsymbol{u}^{(j)}) \end{aligned} \tag{1.50}$$

is one way to do this. Once the update $\boldsymbol{\delta}^{(j)}$ corresponding to the parameter vector estimate $\boldsymbol{u}^{(j)}$ is found, the next parameter estimate is written

$$\boldsymbol{u}^{(j+1)} = \boldsymbol{u}^{(j)} + \boldsymbol{\delta}^{(j)}. \tag{1.51}$$

We may then return to Equation 1.45 and repeat the process above with $j = j + 1$ until $S(\boldsymbol{u}^{(j)})$ reaches a minimum.

The above discussion follows [25, pp. 21–23] and [2, pp. 171–177].

1.3.2.2 Conditions for a Local Minimum

A general nonlinear function may have multiple local minima, as illustrated in Figure 1.18. While the solution procedure of the last section is designed to reach a local minimum, a

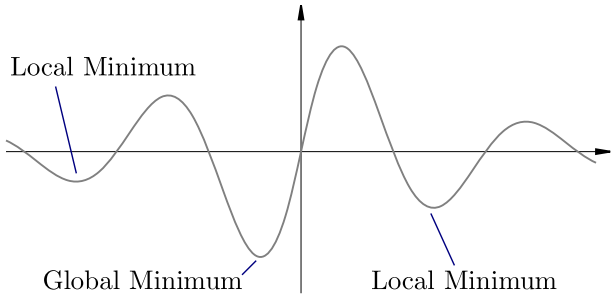

Figure 1.18: Local and Global Minima [38]

point where

$$S(\widehat{\boldsymbol{u}}) \leq S(\boldsymbol{u}), \text{ for all } \boldsymbol{u} \text{ near } \widehat{\boldsymbol{u}}. \tag{1.52}$$

A global minimum, on the other hand, satisfies

$$S(\widehat{\boldsymbol{u}}) \leq S(\boldsymbol{u}), \text{ for all } \boldsymbol{u}. \tag{1.53}$$

The problem of finding the global minimum of a nonlinear function is, in general, quite difficult [2, pp. 182–184]. Here, the focus will be on recognizing when our iterative procedure reaches a local minimum, particularly by examining three conditions for a local minimum.

The first is called the first-order necessary condition: If $S(\widehat{\boldsymbol{u}})$ is a local minimum of $S()$, then $\nabla S(\widehat{\boldsymbol{u}})$ must equal the zero vector, $\mathbf{0}$. Any point $\widehat{\boldsymbol{u}}$ which satisfies the first-order necessary condition is called a *stationary point*. Since this condition only considers first derivative information in the Taylor expansion of $S()$ (See Equation 1.45), a stationary point is not necessarily a minimum. At a saddle point, for instance, $\nabla S(\widehat{\boldsymbol{u}}) = \mathbf{0}$, but $\nabla^2 S(\widehat{\boldsymbol{u}})$ is indefinite, and it is possible to decrease $S()$ further, since $\boldsymbol{\delta}^{\mathrm{T}} \nabla^2 S(\widehat{\boldsymbol{u}}) \boldsymbol{\delta} < 0$ for some $\boldsymbol{\delta}$ [25, p. 92]. This leads to the second-order necessary condition: If $S(\widehat{\boldsymbol{u}})$ is a local minimum of $S()$, then $\nabla S(\widehat{\boldsymbol{u}})$ must equal $\mathbf{0}$, and $\nabla^2 S(\widehat{\boldsymbol{u}})$ must be positive semidefinite. That is, $\boldsymbol{\delta}^{\mathrm{T}} \nabla^2 S(\widehat{\boldsymbol{u}}) \boldsymbol{\delta} \geq 0$ for all $\boldsymbol{\delta}$.

The second-order sufficient condition is stronger than the preceding two conditions. It

states: If $\nabla S(\widehat{\boldsymbol{u}}) = \mathbf{0}$ and $\nabla^2 S(\widehat{\boldsymbol{u}})$ is positive definite ($\boldsymbol{\delta}^{\mathrm{T}} \nabla^2 S(\widehat{\boldsymbol{u}}) \boldsymbol{\delta} > 0$ for all $\boldsymbol{\delta} \neq \mathbf{0}$), then $S(\widehat{\boldsymbol{u}})$ is a strict local minimum of $S()$, which satisfies

$$S(\widehat{\boldsymbol{u}}) < S(\boldsymbol{u}), \text{ for all } \boldsymbol{u} \neq \widehat{\boldsymbol{u}} \text{ near } \widehat{\boldsymbol{u}} \tag{1.54}$$

(Compare with Equation 1.53). The conditions above will be useful later on for examining the success or failure of a nonlinear estimation routine.

The discussion in this section follows [25, pp. 12–16] and [13, pp. 10–13].

1.3.2.3 Gauss-Newton and Levenberg-Marquardt

The Newton update

$$\boldsymbol{\delta}^{(j)} = -\left(\mathbf{J}(\boldsymbol{u}^{(j)})^{\mathrm{T}} \mathbf{J}(\boldsymbol{u}^{(j)}) + \mathbf{G}(\boldsymbol{u}^{(j)})\right)^{-1} \mathbf{J}(\boldsymbol{u}^{(j)})^{\mathrm{T}} \boldsymbol{r}(\boldsymbol{u}^{(j)}) \tag{1.55}$$

requires the calculation of $\frac{1}{2}np(p+1)$ second derivatives to create $\mathbf{G}(\boldsymbol{u}^{(j)})$,

$$\mathbf{G}(\boldsymbol{u}^{(j)}) = \sum_{i=1}^{n} r_i(\boldsymbol{u}^{(j)}) \nabla^2 r_i(\boldsymbol{u}^{(j)}), \tag{1.56}$$

a symmetric $p \times p$ matrix (See Equation 1.48 for the expansion of the Hessian operator ∇^2). Unless the $\mathbf{G}$ matrix is sparse (has many 0 elements), or n and p are small, calculating $\mathbf{G}$ can be time-consuming and error-prone.

Fortunately, there are three situations in which $\mathbf{G}$ may be small relative to $\mathbf{J}^{\mathrm{T}}\mathbf{J}$: First, if the residuals $r_i(\boldsymbol{u}^{(j)}) = f_i(\boldsymbol{u}^{(j)}) - y_i$ approach zero as j increases; second, if $\boldsymbol{f}$ approaches linearity near the minimum, causing its second derivatives to become small; third, if the second derivatives of the n r_i terms are nearly equal, a mix of positive and negative residual terms will allow for cancellation [30, pp. 622–623]. In any case, if the Hessian

$$H(\boldsymbol{u}^{(j)}) = \mathbf{J}(\boldsymbol{u}^{(j)})^{\mathrm{T}} \mathbf{J}(\boldsymbol{u}^{(j)}) + \mathbf{G}(\boldsymbol{u}^{(j)}) \tag{1.57}$$

is dominated by the $\mathbf{J}^{\mathrm{T}}\mathbf{J}$ term, then the Newton step may be approximated by

$$\boldsymbol{\delta}_{GN}^{(j)} = -\left(\mathbf{J}(\boldsymbol{u}^{(j)})^{\mathrm{T}}\mathbf{J}(\boldsymbol{u}^{(j)})\right)^{-1}\mathbf{J}(\boldsymbol{u}^{(j)})^{\mathrm{T}}\boldsymbol{r}(\boldsymbol{u}^{(j)}), \tag{1.58}$$

which requires only the calculation of the first derivatives in the Jacobian. This is the Gauss-Newton (GN) step, and it is a solution the linear least squares problem

$$\min_{\boldsymbol{\delta}^{(j)}} \|\mathbf{J}(\boldsymbol{u}^{(j)})\boldsymbol{\delta}^{(j)} + \boldsymbol{r}(\boldsymbol{u}^{(j)})\|^2. \tag{1.59}$$

It may fail to reduce the residual $S()$ if $\mathbf{J}(\boldsymbol{u}^{(j)})$ is poorly conditioned or singular, or if the matrix $\left(\mathbf{J}(\boldsymbol{u}^{(j)})^{\mathrm{T}}\mathbf{J}(\boldsymbol{u}^{(j)})\right)^{-1}\mathbf{G}(\boldsymbol{u}^{(j)})$ has an eigenvalue with magnitude greater than 1 [16].

The line search Gauss-Newton direction

$$\boldsymbol{\delta}_{LGN}^{(j)} = \alpha \cdot \boldsymbol{\delta}_{GN}^{(j)}, \tag{1.60}$$

where α solves

$$\min_{\alpha}\left[S(\boldsymbol{u}^{(j)} + \alpha \cdot \boldsymbol{\delta}_{GN}^{(j)})\right], \tag{1.61}$$

improves the convergence properties of GN, but the Levenberg-Marquardt (LM) algorithm tends to work even better. Its update step is given as

$$\boldsymbol{\delta}_{LM}^{(j)} = -\left(\mathbf{J}(\boldsymbol{u}^{(j)})^{\mathrm{T}}\mathbf{J}(\boldsymbol{u}^{(j)}) + \lambda\mathbf{I}\right)^{-1}\mathbf{J}(\boldsymbol{u}^{(j)})^{\mathrm{T}}\boldsymbol{r}(\boldsymbol{u}^{(j)}), \tag{1.62}$$

where λ is a positive-valued damping parameter which affects the character of the update. When $\lambda \ll 1$, the LM update resembles the GN update; when $\lambda\mathbf{I} \gg \mathbf{J}(\boldsymbol{u}^{(j)})^{\mathrm{T}}\mathbf{J}(\boldsymbol{u}^{(j)})$,

$$\boldsymbol{\delta}_{LM}^{(j)} \approx -\frac{1}{\lambda}\mathbf{J}(\boldsymbol{u}^{(j)})^{\mathrm{T}}\boldsymbol{r}(\boldsymbol{u}^{(j)}) = -\frac{1}{\lambda}\nabla S(\boldsymbol{u}^{(j)}), \tag{1.63}$$

and the LM update resembles a steepest-descent update with a small step length. According to [25, pp. 21–22], such a step is guaranteed to produce a decrease in the residual if the step length is small enough, or equivalently, if λ is large enough. Taking many such steps does result in slow convergence, but the option to take them allows the LM algorithm to succeed

where the unmodified GN algorithm would have failed.

Although there are various methods for choosing λ, one practical way is to start iteration with a small value, such as $\lambda^{(0)} = 0.01$. If the update significantly reduces the residual, λ may be reduced by a constant factor, such as $\lambda^{(j+1)} = \frac{\lambda^{(j)}}{2}$. If the update fails to reduce the residual, λ may be increased by a constant factor, such as $\lambda^{(j+1)} = 2\lambda^{(j)}$. Fortunately, in the case of a failure, the Jacobian does not need to be recalculated; Equation 1.62 is simply solved with a new value of λ.

The discussion in this section follows [2, pp. 174–177], [13, pp. 91–98], and [30, pp. 619–627].

1.3.2.4 Numerically stable LM updates

There is a better way to calculate the LM update than Equation 1.62, but it requires some motivation. Consider the linear system $\mathbf{A}\boldsymbol{x} = \boldsymbol{b}$ with solution $\boldsymbol{x} = \mathbf{A}^{-1}\boldsymbol{b}$. If the $\boldsymbol{b}$ vector is perturbed by some source of error (measurement noise, roundoff error, etc.) effects of the perturbation will carry through to $\boldsymbol{x}$. This is written explicitly as

$$\boldsymbol{x} + \Delta\boldsymbol{x} = \mathbf{A}^{-1}(\boldsymbol{b} + \Delta\boldsymbol{b}). \tag{1.64}$$

The relative error in $\boldsymbol{x}$ is bounded by the *condition number* of $\mathbf{A}$,

$$\frac{\|\Delta\boldsymbol{x}\|}{\|\boldsymbol{x}\|} \leq \text{cond}(\mathbf{A})\frac{\|\Delta\boldsymbol{b}\|}{\|\boldsymbol{b}\|}, \tag{1.65}$$

where $\text{cond}(\mathbf{A})$ is given as the ratio of the largest and smallest singular values in $\mathbf{A}$,

$$\text{cond}(\mathbf{A}) = \frac{\sigma_{max}}{\sigma_{min}}. \tag{1.66}$$

The condition number serves as a metric for the extent to which $\mathbf{A}$ multiplies error when computing $\boldsymbol{x}$. As a rule of thumb, one may expect to lose one digit of accuracy for every power of 10 in the condition number of $\mathbf{A}$. That is, if $\text{cond}(\mathbf{A}) = 10^2$, 2 digits of accuracy would be lost, and for $\text{cond}(\mathbf{A}) = 10^4$, 4 digits of accuracy would be lost. This matters for the calculation of the LM update, since $\text{cond}(\mathbf{J}(\boldsymbol{u}^{(j)})^{\mathrm{T}}\mathbf{J}(\boldsymbol{u}^{(j)})) = \left[\text{cond}(\mathbf{J}(\boldsymbol{u}^{(j)}))\right]^2$ —

See Equation 1.62. Discussion of conditioning follows [20, pp. 56–61, 118, 139] and [34, pp. 363–365].

The LM update may be alternatively formulated as the solution to

$$\min_{\boldsymbol{\delta}} \left\| \begin{bmatrix} \boldsymbol{r}(\boldsymbol{u}^{(j)}) \\ \mathbf{0} \end{bmatrix} + \begin{bmatrix} \mathbf{J}(\boldsymbol{u}^{(j)}) \\ (\lambda \mathbf{I})^{\frac{1}{2}} \end{bmatrix} \cdot \boldsymbol{\delta} \right\|^2, \tag{1.67}$$

a linear least squares problem equivalent to Equation 1.62 which may be solved in a more numerically stable way, such as through use of the QR decomposition [30, p. 624].

The QR decomposition of an $n \times p$ matrix $\mathbf{A}$ results in

$$\mathbf{A} = \mathbf{QR}, \tag{1.68}$$

where $\mathbf{Q}$ is an $n \times p$ orthonormal matrix whose columns form a basis for the column space of $\mathbf{A}$, and $\mathbf{R}$ is a $p \times p$ upper triangular matrix. As an orthonormal matrix, $\mathbf{Q}$ has the following property,

$$\mathbf{Q}^{\mathrm{T}}\mathbf{Q} = \mathbf{I}, \tag{1.69}$$

which will allow the least squares problem to be solved in a numerically stable way. An overdetermined linear system $\mathbf{A}\boldsymbol{u} = \boldsymbol{y}$, with $\boldsymbol{u} \in \mathbb{R}^p$ and $\boldsymbol{y} \in \mathbb{R}^n$, has the normal equations

$$\mathbf{A}^{\mathrm{T}}\mathbf{A}\widehat{\boldsymbol{u}} = \mathbf{A}^{\mathrm{T}}\boldsymbol{y}, \tag{1.70}$$

which, using the QR decomposition, become

$$\mathbf{R}^{\mathrm{T}}\mathbf{Q}^{\mathrm{T}}\mathbf{Q}\mathbf{R}\widehat{\boldsymbol{u}} = \mathbf{R}^{\mathrm{T}}\mathbf{Q}^{\mathrm{T}}\boldsymbol{y}. \tag{1.71}$$

This simplifies via Equation 1.69 to

$$\mathbf{R}^{\mathrm{T}}\mathbf{R}\widehat{\boldsymbol{u}} = \mathbf{R}^{\mathrm{T}}\mathbf{Q}^{\mathrm{T}}\boldsymbol{y} \tag{1.72}$$

and, by removing $\mathbf{R}^{\mathrm{T}}$ from both sides, to

$$\mathbf{R}\widehat{\boldsymbol{u}} = \mathbf{Q}^{\mathrm{T}}\boldsymbol{y}. \tag{1.73}$$

Equation 1.73 is an upper triangular system, which may be solved for the least-squares solution $\widehat{\boldsymbol{u}}$ to the overdetermined linear system $\mathbf{A}\boldsymbol{u} = \boldsymbol{y}$ without forming $\mathbf{A}^{\mathrm{T}}\mathbf{A}$. As before, $\mathbf{A}$ is required to be of full column rank.

Discussion of the QR decomposition follows [34, pp. 167–169] and [20, pp. 119–121].

1.3.2.5 Summary

When the function of interest produces an output which is nonlinear with respect to its parameters, the parameters are no longer estimated in a single calculation, as with linear least-squares; instead an interative process is used. This involves solving a succession of linear least-squares problems, each of which is a linearization of the residual function about the current parameter estimates. While there are various ways of carrying out this process, the Levenberg–Marquardt algorithm, with update calculated by applying the QR decomposition to the linear least squares problem of Equation 1.67, is the algorithm used in the main body of this work. It avoids the computational cost of calculating the Hessian matrix required by Newton's method and has better convergence properties than the Gauss–Newton algorithm. Furthermore, its update calculations are numerically stable.

1.4 Functional Methods for HJC Estimation

This section is placed after both background chapters because it requires knowledge of both biomechanic topics and parameter estimation techniques yet remains preliminary to the chapters that follow.

1.4.1 Why Functional Methods

The centers and axes of rotation of the joints of the body, collectively called joint parameters, are used to define the position and orientation of anatomical frames [29]. Their values are sometimes derived from Anatomical Landmarks (ALs) and regression methods, as seen in

Sections 1.2.5.5, 1.2.5.7, and 1.2.5.6. These methods have some drawbacks. AL palpitation is prone to operator error, which can lead to kinematic crosstalk — the recovery of spurious joint angles due to a misaligned anatomical frame [26]. Regression methods predict HJC location using the ALs as independent variables, but this process is not subject specific.

Functional methods provide an alternative means to estimate joint parameters; they operate by applying mathematical techniques to a subject's movement data. Typically an additional movement exercising the joint of interest is collected, such as the Star Arc movement (see Section 1.2.6.4), which is used to locate the HJC [5]. Unlike AL palpitation and regression methods, functional methods are both subject specific and operator independent [29], but they are susceptible to bias due to the effects of Soft Tissue Artifact (STA) [27]. There are many different functional methods aimed at estimating the location of the HJC [11] as well as the location of the Knee Joint Center (KJC) and the location and orientation of the Knee Flexion Axis (KFA) [12].

1.4.2 Details of a Functional Method

This section presents one functional method, the Symmetrical Center of Rotation Estimation (SCoRE) [35], which estimates the location of the HJC. The development of SCoRE depends on the rigid body hypothesis, which assumes that the tracking markers rigidly follow the underlying bone of each segment. Under this assumption, the two points

$$ {}^{pt}P_{HJC} \text{ and } {}^{ft}P_{HJC}, \tag{1.74} $$

which give the HJC in the coordinates of the pelvic and femoral technical frames, will remain coincident throughout movement of the hip when transformed into camera coordinates,

$$ {}^{cam}_{pt}T \cdot {}^{pt}P_{HJC} \approx {}^{cam}_{ft}T \cdot {}^{ft}P_{HJC}. \tag{1.75} $$

The affine form (see Section 1.2.5.3) of this equation is

$$ {}^{cam}_{pt}R \cdot {}^{pt}P_{HJC} + {}^{cam}P_{\circ_{pt}} \approx {}^{cam}_{ft}R \cdot {}^{ft}P_{HJC} + {}^{cam}P_{\circ_{ft}}. \tag{1.76} $$

In both forms, the equality is only approximate, as the rigid body hypothesis is not perfectly fulfilled in practice due to the presence of STA. The SCoRE method finds the HJC locations in pt and ft coordinates which come closest to satisfying Eqn 1.75 during a recorded hip movement. Given n frames of movement data, this is accomplished by solving the least-squares problem

$$\min_{\substack{{}^{pt}P_{HJC} \\ {}^{ft}P_{HJC}}} \left\| \begin{bmatrix} {}^{cam}_{pt}R_1 & -{}^{cam}_{ft}R_1 \\ {}^{cam}_{pt}R_2 & -{}^{cam}_{ft}R_2 \\ \vdots & \vdots \\ {}^{cam}_{pt}R_n & -{}^{cam}_{ft}R_n \end{bmatrix} \begin{bmatrix} {}^{pt}P_{HJC} \\ {}^{ft}P_{HJC} \end{bmatrix} + \begin{bmatrix} \left({}^{cam}P_{\circ_{pt}} - {}^{cam}P_{\circ_{ft}} \right)_1 \\ \left({}^{cam}P_{\circ_{pt}} - {}^{cam}P_{\circ_{ft}} \right)_2 \\ \vdots \\ \left({}^{cam}P_{\circ_{pt}} - {}^{cam}P_{\circ_{ft}} \right)_n \end{bmatrix} \right\|^2 . \tag{1.77}$$

Writing

$$\mathbf{A} = \begin{bmatrix} {}^{cam}_{pt}R_1 & -{}^{cam}_{ft}R_1 \\ {}^{cam}_{pt}R_2 & -{}^{cam}_{ft}R_2 \\ \vdots & \vdots \\ {}^{cam}_{pt}R_n & -{}^{cam}_{ft}R_n \end{bmatrix} \quad \boldsymbol{y} = - \begin{bmatrix} \left({}^{cam}P_{\circ_{pt}} - {}^{cam}P_{\circ_{ft}} \right)_1 \\ \left({}^{cam}P_{\circ_{pt}} - {}^{cam}P_{\circ_{ft}} \right)_2 \\ \vdots \\ \left({}^{cam}P_{\circ_{pt}} - {}^{cam}P_{\circ_{ft}} \right)_n \end{bmatrix}, \tag{1.78}$$

the equation

$$\begin{bmatrix} {}^{pt}P_{HJC} \\ {}^{ft}P_{HJC} \end{bmatrix} = \left(\mathbf{A}^{\mathrm{T}} \mathbf{A} \right)^{-1} \mathbf{A}^{\mathrm{T}} \boldsymbol{y} \tag{1.79}$$

gives the solution to Eqn 1.77, although more numerically robust methods are available.

The contribution of each data frame to the residual vector,

$$\boldsymbol{r} = \mathrm{A} \cdot \begin{bmatrix} {}^{pt}P_{HJC} \\ {}^{ft}P_{HJC} \end{bmatrix} - \boldsymbol{y}, \tag{1.80}$$

is given by

$${}^{cam}_{pt}R \cdot {}^{pt}P_{HJC} + {}^{cam}P_{\circ_{pt}} - \left({}^{cam}_{ft}R \cdot {}^{ft}P_{HJC} + {}^{cam}P_{\circ_{ft}} \right), \tag{1.81}$$

which quantifies violation of the equality given in Eqn 1.76.

1.4.3 Properties and Performance of Functional Methods

The SCoRE method has some properties typical of functional methods. Movement data is required from both segments adjacent to the joint, in this case, the pelvis and thigh. Further, functional methods are typically tailored to either estimate a center of rotation, such as the HJC, or a center and axis of rotation, such as the KJC and KFA [11, 12, 29, 14]. Some joints, such as the wrist and ankle, are not appropriately modelled by a single center or axis of rotation. For these, optimization methods, which fit a general kinematic model to a subject's movement data, are employed [32, 40].

The SCoRE method HJC estimate was found to have an mean error of about 20mm relative to 3D ultrasound determination of the HJC when tested on a group of 19 subjects [27]. The same study found the best performing functional method, Geometric Sphere Fitting, to have a mean error of 15mm. While the SCoRE method relies on the rigid body hypothesis, sphere fitting methods use multiple markers on the thigh segment and assume that the origin of each one lies a constant distance from the HJC; this criterion is less stringent than the rigid body hypothesis [14], which may make the sphere fitting method less susceptible to the effects of STA than the SCoRE method. While functional methods are meant to improve upon regression methods, they are hampered by the effects of STA. Meanwhile, the best performing regression method examined in [27] — that of Harrington, et al. — attained a mean error of 16mm; it turns out there are no clear winners in the contest for accurate HJC location estimates.

Using functional methods instead of AL palpitation to estimate the KFA orientation has been shown to improve the repeatability of gait data and to reduce kinematic crosstalk [28, 29]. In this case, the value of functional methods is more readily apparent.

1.4.4 Summary

Functional methods use mathematical techniques to estimate joint parameter values from a subject's movement data. They are meant to improve upon anatomical landmark palpitation and regression methods and have the dual advantage of being operator independent and subject specific. Unfortunately, they are subject to bias due to the presence of soft tissue

artifact, and the best functional and regression methods for hip joint center location show similar performance. Functional methods display promising results in finding the orientation of the knee flexion axis. They are limited to finding the center and/or axis of rotation of a joint; more complicated joint models require the use of optimization techniques.

1.5 Preview of Coming Chapters

Chapters 2, 3, and 4 are formatted as individual papers intended for submission to various journals. They cover different aspects of the central focus of this work: The estimation of joint parameters at the hip and knee through the fitting of a kinematic model spanning both joints to motion data from the pelvic and lower leg segments using an optimization method.

Chapter 2 presents a detailed mathematical analysis of the kinematic model of the hip and knee, with particular focus on the parameters which define the orientation of the model's tibial anatomical frame. The analysis finds that these parameters may vary widely without affecting the residual, which quantifies the fit of the kinematic model to a subject's movement data. As a result, these parameters cannot be reasonably estimated using an optimization method and must be determined through other means.

Chapter 3 presents the results of a motion capture study, which uses the optimization method central to this work to estimate the joint parameters of 10 subjects, and the estimation process is repeated 5 times for each subject. Repeatability is reasonably good; standard deviation of the joint parameters across 5 repetitions is, on average, 3.52mm for hip joint center location, 2.44mm for femoral length, and 1.67mm for knee joint center location. A technique for orienting the tibial anatomical frame of the kinematic model is presented in Chapter 3, along with a demonstration of the non-invasive investigation of thigh soft tissue artifact using the model fitting procedure.

Chapter 4 presents a nonlinear optimization method for fitting a general kinematic model to motion data which improves upon the two-level optimization method of Sommer and Miller [32]. Both methods are set forth and compared in detail. The new method results in parameter estimates consistent with those produced by the two-level method, but at a significantly reduced computational cost. When applied to data from the motion capture

study of Chapter 3, the new method converges approximately 30 times faster than the two-level method.

Chapter 2

Parameter identifiability of a five degree of freedom kinematic model with application in human movement analysis

Ben Tesch[1,*], Brian S.R. Armstrong[1]

1 University of Wisconsin-Milwaukee

∗ **E-mail: Corresponding bctesch@uwm.edu**

2.1 Abstract

Optimization methods provide a means to estimate joint parameters in the context of human movement analysis. These methods use a nonlinear optimization routine to fit a kinematic model of the joint(s) of interest to motion capture data of the human subject under study. The model parameters which best fit the subject's data are taken as estimates of the subject's joint parameters. A five degree of freedom (DoF) model, which represents the hip as a spherical joint and the knee as a 2 DoF compound hinge joint, shows particular promise for estimating parameters of the hip and knee. In fitting this model to a subject, motion capture data is required from only two segments of the body: the pelvis and lower leg. By removing dependence on data from the thigh, a major source of soft tissue artefact is removed from the fitting procedure, and more accurate parameter estimates are expected. Unfortunately, the three parameters in the 5 DoF model which define the orientation of the tibial anatomical frame are able to vary widely without affecting the model's ability to fit a given data set. The mathematical properties of the model which allow this to happen are set forth in this paper, as is a procedure for calculating the range over which the three parameters may vary. Under reasonable assumptions about the human knee, this range is large enough to exclude the possibility of estimating the orientation of the tibial anatomical

frame. The 5 DoF model may still prove useful for estimating other joint parameters, such as the hip and knee joint centers.

2.2 Introduction

In human movement analysis, joint parameters, which include the centers and axes of rotation of the body's joints, play an important role in reconstructing the kinematics and kinetics of the body from motion data. Joint parameters are needed due to the way motion data is collected. Typically, motion tracking markers are placed over the skin of a human subject on each segment of the body that is to be measured, such as the pelvis, thigh, and lower leg; these markers are assumed to have a fixed relationship with respect to the underlying bone. An optical motion tracking system measures the location these markers in 3D space at discrete intervals as the subject moves. The resultant data is used to reconstruct the *pose* of each body segment under measurement, and the set of all such poses is called the data set. Pose is the combination of position and orientation. It is often represented mathematically by a reference frame, where the reference frame axes represent orientation and the reference frame origin represents position. The reference frame representing the pose of a body segment as reconstructed from the tracking markers is called a *technical frame*. Because the markers may be placed at different locations on a given body segment, their placement does not bear a repeatable relationship to the subject's anatomy [3].

Without a reference frame aligned to the anatomy, it is impossible to meaningfully compare data collected on different days, let alone data from different subjects. Joint parameters provide a remedy to this problem, as they may be used to define a reference frame which is aligned to the subject's anatomy [21]. Such a reference frame is called an *anatomical frame*, and for each body segment under measurement, one anatomical frame is defined in the coordinates of the segment's technical frame [3].

Accurate joint parameter estimates are crucial for obtaining valid data. Errors in hip joint center (HJC) location can lead to significant errors in calculated moments at the hip [24]. Similarly, kinematic crosstalk, the recovery of non-physiological joint angles due to a misaligned anatomical frame, can result from an inaccurate estimate of the orientation of

the knee flexion axis [15, 20].

There are several methods for determining joint parameters. Anatomical landmark (AL) palpitation is used to orient anatomical frames at the pelvis, femur, and tibia; it is also used to find joint centers at the knee and ankle [2]. The HJC may not be directly found in this way. Instead, regression equations are used to estimate its location based on measurements of the ALs at the hip and leg [5]. The lack of subject specificity in regression equations adds another source of error to the variability already present in the palpitation of ALs [9]. Functional methods use mathematical techniques to estimate joint parameters from a subject's movement data. They are subject specific and are not influenced by the same sources of error as regression equations and AL palpitation. Various functional methods have been used to find the HJC [6] as well as the knee flexion axis and knee joint center (KJC) [7]. Functional methods show promise, but they may be biased due to the presence of soft tissue artefact (STA) [19]. STA is the measurement error introduced by movement of tissue between motion tracking markers and the underlying bone. It is a major hindrance in the field of human movement analysis [11]. Of note is a new set of regression equations for the HJC [8] which is competitive with the best functional method when both are judged against 3D ultrasound localization of the HJC [19].

The five degree of freedom (DoF) model which is analyzed in this paper has an intended application in the estimation of joint parameters as part of an optimization method. Optimization methods require a kinematic model of the joint of interest and motion data which records the subject exercising this joint. The kinematic model is defined by two kinds of quantities: model parameters and joint angles. The model parameters represent quantities which do not change during movement, such as the position of the hip joint center in the pelvis or the orientation of the knee flexion axis in the femur. Joint angles encode the degrees of freedom of the model's joints and may take on a different value for each measurement of the subject's pose in the data set. Optimization methods estimate joint parameters by using a nonlinear optimization routine to adjust the model parameters and joint angles of the kinematic model so that it reproduces or "fits" the subject's movement data as closely as possible. The model parameters which best fit the subject's data are taken as estimates of the subject's joint parameters. [17, 23, 25]

The 5 DoF model which is the focus of this paper uses a spherical joint to model the hip and a 2 DoF compound hinge joint to model the knee, allowing estimation of the parameters of both joints. Because the model has 5 DoF, it may be fitted to motion data from only the pelvis and lower leg segments using the optimization routine in [23], provided both segments are tracked with 6 DoF measurement. Lack of dependence on data from the thigh segment may lead to improved parameter estimates, as such data is affected by a high degree of STA [18]. A model with a spherical hip joint and four bar linkage knee joint has previously been employed to remove dependence on data from the thigh in [14], but it appears there is some difficulty in adapting this more complicated model to individual subjects. The simpler 2 DoF compound hinge knee model is suggested by the work of Hollister, et al. who found knee motion to be well represented by fixed flexion axis and a fixed longitudinal rotation axis. The longitudinal rotation axis was both placed anterior and oriented non-orthogonally with respect to the flexion axis. [10]. Prior work has been carried out in fitting this knee model to motion data [16]. The 2 DoF compound hinge used in this work's 5 DoF model is a simplified version of the one just mentioned, as its flexion and longitudinal rotation axes are both orthogonal and intersecting.

In attempting to fit the 5 DoF model to motion data, it was found that the parameters encoding the orientation of the tibial anatomical frame may vary over a wide range without affecting the model's fit to a given data set. An optimization routine has only one criterion for adjusting model parameters: It chooses the values of the model parameters which allow the model to best fit the data set. Since many values for the parameters which orient the tibial anatomical frame fit the data equally well, these parameters are considered unidentifiable. That is, they cannot be reasonably estimated by an optimization routine. The present work analyzes this phenomenon mathematically by fitting the model to a synthetic data set. The synthetic data set is created from the model equations and contains all poses consistent with a normal range of human joint motion. A procedure is derived for calculating the range over which the unidentifiable parameters may vary while allowing the model to fit the synthetic data set exactly. Numerical results for this range are presented for reasonable values of the other model parameters, and the consequences of parameter unidentifiability for the application of the 5 DoF model are discussed.

2.3 Methods

The model is defined by a series of homogeneous transforms (HTs), and its joint angles are encoded in the model definition as Cardan angles. A brief overview of these mathematical techniques is presented prior to the definition and analysis of the model.

2.3.1 Homogeneous Transforms

Suppose there are three reference frames: a, b, and c. The HT from frame a to frame b, ${}^b_aT$, is a 4×4 matrix given by the equation

$$ {}^b_aT = \begin{bmatrix} & {}^b_aR & & {}^bP_{\mathring{a}} \\ 0 & 0 & 0 & 1 \end{bmatrix}, \tag{2.1} $$

where ${}^b_aR$ is a 3×3 rotation matrix whose columns are the basis vectors of frame a written in b coordinates, and ${}^bP_{\mathring{a}}$ is a 3-vector which represents the origin of frame a (written $\mathring{a}$) as a point in b coordinates. Given an arbitrary point o in a coordinates, ${}^aP_o$,

$$ {}^aP_o = \begin{bmatrix} x \\ y \\ z \\ 1 \end{bmatrix}, \tag{2.2} $$

to which a fourth element of value 1 has been appended, multiplication by ${}^b_aT$ will transform this point into a b coordinate representation

$$ {}^bP_o = {}^b_aT \cdot {}^aP_o. \tag{2.3} $$

Assume that any vector or point which is being multiplied by an HT has this additional 1 appended to it.

Rotation matrices and homogeneous transforms have some additional useful properties.

For any rotation matrix R, the following hold

$$\begin{aligned} R^{\mathrm{T}}R &= I \\ R^{\mathrm{T}} &= R^{-1}, \end{aligned} \tag{2.4}$$

where I is the identity matrix. For arbitrary reference frames a and b,

$${}^{a}_{b}R = \left({}^{b}_{a}R\right)^{\mathrm{T}} = \left({}^{b}_{a}R\right)^{-1}, \tag{2.5}$$

inverting a rotation matrix switches the order of its *from* and *to* frames. A similar formula applies to HTs,

$${}^{a}_{b}T = \left({}^{b}_{a}T\right)^{-1}, \tag{2.6}$$

but the inverse of an HT is not equal to its transpose; instead, the inverse is given by

$$\left({}^{b}_{a}T\right)^{-1} = \begin{bmatrix} & \left({}^{b}_{a}R\right)^{\mathrm{T}} & & -\left({}^{b}_{a}R\right)^{\mathrm{T}} \cdot {}^{b}P^{\circ}_{a} \\ 0 & 0 & 0 & 1 \end{bmatrix}. \tag{2.7}$$

Finally, both rotation matrices and HTs may be chained together,

$$\begin{aligned} {}^{c}_{a}R &= {}^{c}_{b}R \cdot {}^{b}_{a}R \\ {}^{c}_{a}T &= {}^{c}_{b}T \cdot {}^{b}_{a}T. \end{aligned} \tag{2.8}$$

For information on HTs, see also [27, ch. 1.2.5.1].

2.3.2 Cardan Angles

Cardan angles are often used in human movement analysis to define a rotation between coordinate frames by a sequence of three elemental rotations about a specific set of axes. When the sequence and axes are properly defined, and the rotation spans coordinate frames on either side of a joint, the values of the three Cardan angles will correspond to the joint angles flexion/extension (FL/EX), adduction/abduction (AD/AB), and internal/external

rotation (IN/EX), respectively [22]. The elemental rotations are shown below,

$$\begin{aligned}
\mathrm{R}\left({}^{b}_{a}E_x\right) &= \begin{bmatrix} 1 & 0 & 0 \\ 0 & C_x & S_x \\ 0 & -S_x & C_x \end{bmatrix} \\
\mathrm{R}\left({}^{b}_{a}E_y\right) &= \begin{bmatrix} C_y & 0 & -S_y \\ 0 & 1 & 0 \\ S_y & 0 & C_y \end{bmatrix} \\
\mathrm{R}\left({}^{b}_{a}E_z\right) &= \begin{bmatrix} C_z & S_z & 0 \\ -S_z & C_z & 0 \\ 0 & 0 & 1 \end{bmatrix},
\end{aligned} \tag{2.9}$$

where $\mathrm{R}(\cdot)$ is an operator which creates the appropriate elementary rotation matrix from a given Cardan angle $({}^{b}_{a}E_x, {}^{b}_{a}E_y, {}^{b}_{a}E_z)$. Also, S_z abbreviates $\sin\left({}^{b}_{a}E_z\right)$, C_x abbreviates $\cos\left({}^{b}_{a}E_x\right)$, and so on. Using what will here be called the Z-X-Y sequence, the rotation from a to b coordinates may be created from the elementary rotations,

$${}^{b}_{a}R = \mathrm{R}\left({}^{b}_{a}E_y\right) \cdot \mathrm{R}\left({}^{b}_{a}E_x\right) \cdot \mathrm{R}\left({}^{b}_{a}E_z\right). \tag{2.10}$$

This may be thought of as a rotation of ${}^{b}_{a}E_z$ degrees about the Z axis of frame a, followed by a rotation of ${}^{b}_{a}E_x$ degrees about an axis mutually perpendicular to the Z axis of frame a and the Y axis of frame b, followed by a rotation of ${}^{b}_{a}E_y$ degrees about the Y axis of frame b. ${}^{b}_{a}R$ has the form

$$\begin{bmatrix} C_zC_y - S_zS_yS_x & S_zC_y + C_zS_yS_x & -S_yC_x \\ -S_zC_x & C_zC_x & S_x \\ C_zS_y + S_zC_yS_x & S_zS_y - C_zC_yS_x & C_yC_x \end{bmatrix}. \tag{2.11}$$

The Z-X-Y sequence Cardan angles may be extracted from a rotation matrix ${}^b_aR$ using the equations

$$\begin{aligned} {}^b_aE_x &= \text{asin}\left({}^b_aR(2,3)\right) \\ {}^b_aE_y &= \text{atan2}\left(-{}^b_aR(1,3),\, {}^b_aR(3,3)\right) \\ {}^b_aE_z &= \text{atan2}\left(-{}^b_aR(2,1),\, {}^b_aR(2,2)\right). \end{aligned} \tag{2.12}$$

It is handy to define an operator $\text{E}(\cdot)$ which performs this function,

$${}^b_aE = \text{E}\left({}^b_aR\right). \tag{2.13}$$

Finally, the homogeneous transform ${}^b_aT$ has six degrees of freedom but 16 elements. The 6 DoF of ${}^b_aT$ may be represented by six elements: three for translation,

$${}^bP_{a^\circ} = \begin{bmatrix} {}^bP_{a^\circ}(x) \\ {}^bP_{a^\circ}(y) \\ {}^bP_{a^\circ}(z) \end{bmatrix}, \tag{2.14}$$

where ${}^bP_{a^\circ}(x)$ is the X component of ${}^bP_{a^\circ}$, and three for rotation,

$${}^b_aE = \begin{bmatrix} {}^b_aE_x \\ {}^b_aE_y \\ {}^b_aE_z \end{bmatrix}, \tag{2.15}$$

where ${}^b_aR$ is decomposed into the Cardan angles in ${}^b_aE$. These six elements fully define the pose of the a frame in b coordinates; they simply have a more compact form than ${}^b_aT$, which also defines the pose of the a frame in b coordinates.

2.3.3 Model Definition

Figure 2.1 shows an exploded view of the reference frames of the 5 DoF model along with some of their connections. The model is defined by a series of homogeneous transforms (HTs) between named reference frames. The HTs themselves are populated using model parameters, joint angles, and anatomical landmarks.

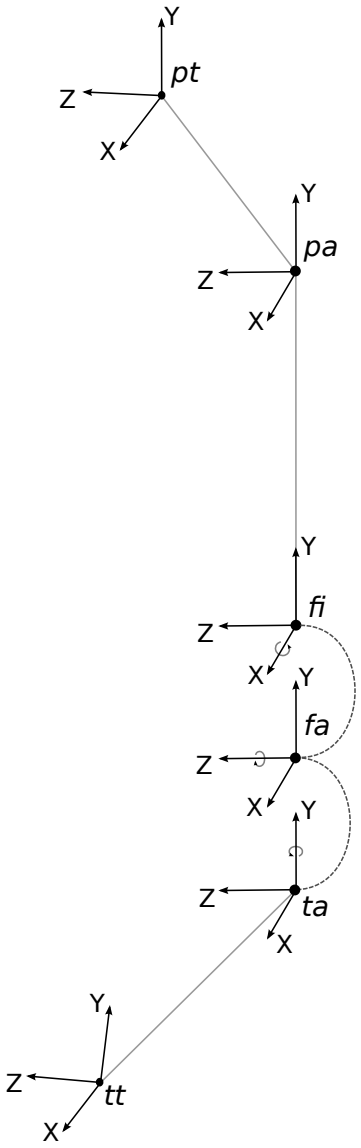

Figure 2.1: **Links and reference frames of 5 DoF model in exploded view.**

The pelvic and tibial technical frames, *pt* and *tt*, represent the pose of their respective body segments as it would be recorded by a motion capture system. These typically correspond to the position and orientation of tracking markers placed over the skin on each measured segment and do not necessarily bear a repeatable relationship to the subject's anatomy [3]. The model also contains anatomical frames, each of which represents the pose of one of the subject's bones. These include the pelvic, femoral, and tibial anatomical frames, abbreviated *pa*, *fa*, and *ta*, respectively. The goal in fitting the model to motion data is to align the anatomical frames to the subject's anatomy in a way that is repeatable

and physiologically valid.

The orientation of the pelvic anatomical frame, *pa*, in *pt* coordinates is given by the rotation matrix ${}^{pa}_{pt}R$, which is composed from the three Cardan angles in ${}^{pa}_{pt}E$ using Eqn 2.10. These values are set a-priori from pelvic anatomical landmarks according to [26]. As such, they are constants not adjusted by the fitting procedure. The origin of the *pa* frame is placed at the hip joint center (HJC); it is determined by the three values in ${}^{pa}P_{\overset{\circ}{pt}}$. These values are model parameters — their value is set by the fitting procedure, but it remains constant across the poses of the data set.

The rotation from the *pa* frame to the femoral intermediate frame, *fi*, is given by the three Cardan angles ${}^{fi}_{pa}E_x$, ${}^{fi}_{pa}E_y$, and ${}^{fi}_{pa}E_z$. These are joint angles; they may each take on a different value for every pose in the data set. Because they create ${}^{fi}_{pa}R$ by the Z-X-Y sequence, ${}^{fi}_{pa}E_z$ encodes a rotation about the Z axis of the *pa* frame corresponding to hip flexion/extension (FL/EX), ${}^{fi}_{pa}E_y$ encodes a rotation about the Y axis of the *fi* frame corresponding to hip internal/external rotation (IN/EX), and hip adduction/abduction (AD/AB) is given by ${}^{fi}_{pa}E_x$, which encodes a rotation about an axis mutually perpendicular to the Z axis of *pa* and the Y axis of *fi* [4]. These are the three DoF of the spherical joint which models the hip.

The translation ${}^{fi}P_{\overset{\circ}{pa}}$ has only one non-zero component, ${}^{fi}P_{\overset{\circ}{pa}}(y)$, a model parameter. This constrains the HJC ($\overset{\circ}{pa}$) to lie along the Y axis of the *fi* frame. Since the origin of the *fi* frame lies at the knee joint center (KJC), ${}^{fi}P_{\overset{\circ}{pa}}(y)$ encodes the length of the femur. The *fi* frame serves two functions: It allows hip IN/EX to occur about the vector pointing from the KJC to the HJC, and it allows the knee flexion axis to have a non-orthogonal orientation with respect to that vector. Since the knee flexion axis is the Z axis of the femoral anatomical frame (*fa*), this second function is accomplished by defining the rotation from *fi* to *fa*,

$$ {}^{fa}_{fi}R = \mathrm{R}\left({}^{fa}_{fi}E_x\right), \tag{2.16} $$

to be an elementary rotation about the X axis of the *fi* frame (See Eqn 2.9). The origin of the *fa* frame is also placed at the KJC; consequently, the translation ${}^{fa}P_{\overset{\circ}{fi}}$ is given by the zero vector, $\mathbf{0}$.

The rotation from the femoral anatomical frame (fa) to the tibial anatomical frame (ta) is created according to the equation

$$\begin{aligned} {}^{ta}_{fa}R &= \mathrm{R}\left({}^{ta}_{fa}E_y\right) \cdot \mathrm{R}\left({}^{ta}_{fa}E_z\right) \\ &= \begin{bmatrix} C_z C_y & S_z C_y & -S_y \\ -S_z & C_z & 0 \\ C_z S_y & S_z S_y & C_y \end{bmatrix}, \end{aligned} \tag{2.17}$$

where ${}^{ta}_{fa}E_z$ and ${}^{ta}_{fa}E_y$ are joint angles. They represent the 2 DoF of the compound hinge knee joint: rotation of ${}^{ta}_{fa}E_z$ degrees about the Z axis of fa, corresponding to FL/EX, followed by rotation of ${}^{ta}_{fa}E_y$ degrees about the Y axis of ta corresponding to IN/EX. The fa and ta frames share an origin at the KJC, and so ${}^{ta}P_{\circ}_{fa} = \mathbf{0}$.

The pose of the ta frame relative to the tt frame is defined by the six model parameters in ${}^{tt}_{ta}E$ and ${}^{tt}P_{\circ}_{ta}$. ${}^{tt}P_{\circ}_{ta}$ gives the location of the KJC in tt coordinates. The model parameters ${}^{tt}_{ta}E_x$, ${}^{tt}_{ta}E_y$, and ${}^{tt}_{ta}E_z$ are the focus of this paper. They create ${}^{tt}_{ta}R$ via the Y-X-Z sequence (see Eqn 2.40) and are able to vary over a significant range without affecting the model's fit to a given data set.

2.3.4 A Synthetic Data Set

While the 5 DoF model is fitted to motion capture data in its intended application, such data is inappropriate for an exact mathematical analysis. It contains errors due to soft tissue artifact (STA), and no single recorded data set will contain all the poses that may be encountered in practice. In order to avoid these shortcomings, two models are created: the data model and the exploratory model. The data model is used to create a synthetic data set, referred to subsequently as the data set. The data set contains all poses of the data model,

$${}^{tt}_{pt}T_{(d)}, \tag{2.18}$$

produced by varying its joint angles within a range consistent with the normal limits of human joint motion. The exploratory model is used to explore the range over which the unidentifiable parameters, ${}^{tt}_{ta}E$, may vary relative to those of the data model, without af-

fecting the ability of the exploratory model to exactly fit every pose in the data set.

For the most part, the exploratory and data models have the same definition. All model parameters except ${}^{tt}_{ta}E$ have the same value in both models, and the joint angles are set independently in each model. For quantities which may differ between models, a subscript *(m)* or *(d)* will mark a quantity as belonging to the exploratory or data model, respectively. ${}^{tt}_{pt}T_{(d)}$ is generated by the equation for the data model

$$ {}^{tt}_{pt}T_{(d)} = {}^{tt}_{ta}T_{(d)} \cdot {}^{ta}_{fa}T_{(d)} \cdot {}^{fa}_{fi}T \cdot {}^{fi}_{pa}T_{(d)} \cdot {}^{pa}_{pt}T. \tag{2.19} $$

Likewise, ${}^{tt}_{pt}T_{(m)}$ is generated by the equation for the exploratory model

$$ {}^{tt}_{pt}T_{(m)} = {}^{tt}_{ta}T_{(m)} \cdot {}^{ta}_{fa}T_{(m)} \cdot {}^{fa}_{fi}T \cdot {}^{fi}_{pa}T_{(m)} \cdot {}^{pa}_{pt}T. \tag{2.20} $$

Even though ${}^{tt}P_{\circ}_{ta}$ has the same value for both models, ${}^{tt}_{ta}T$ receives a subscript *(m)* or *(d)* because the model parameters ${}^{tt}_{ta}E$ are allowed to differ between models. Similarly, ${}^{fi}P_{\circ}_{pa}$ has the same value in both models, but ${}^{fi}_{pa}T$ receives a subscript because the joint angles may differ between models.

The goal of the analysis is to determine the range over which ${}^{tt}_{ta}E_{(m)}$ and ${}^{tt}_{ta}E_{(d)}$ may differ relative to each other while the exploratory model fits all poses in the data set. This range will be called the region of unidentifiability. All values of ${}^{tt}_{ta}E$ in this range fit the data set equally well, and the optimization routine lacks a criterion to choose between them.

2.3.5 Conditions for Pose Equality

The analysis starts by finding the conditions under which one pose of the exploratory model may be made equivalent to a pose of the data model. It is desirable to simplify these conditions as much as possible, reducing the work in later stages of analysis. The exploratory and data models produce an equivalent pose when

$$ {}^{tt}_{pt}T_{(m)} = {}^{tt}_{pt}T_{(d)}. \tag{2.21} $$

Eqn 2.21 may be expanded,

$$\begin{aligned} &{}^{tt}_{ta}T_{(m)} \cdot {}^{ta}_{fa}T_{(m)} \cdot {}^{fa}_{fi}T \cdot {}^{fi}_{pa}T_{(m)} \cdot {}^{pa}_{pt}T \\ &= {}^{tt}_{ta}T_{(d)} \cdot {}^{ta}_{fa}T_{(d)} \cdot {}^{fa}_{fi}T \cdot {}^{fi}_{pa}T_{(d)} \cdot {}^{pa}_{pt}T, \end{aligned} \tag{2.22}$$

allowing the cancellation of ${}^{pa}_{pt}T$,

$$\begin{aligned} &{}^{tt}_{ta}T_{(m)} \cdot {}^{ta}_{fa}T_{(m)} \cdot {}^{fa}_{fi}T \cdot {}^{fi}_{pa}T_{(m)} \\ &= {}^{tt}_{ta}T_{(d)} \cdot {}^{ta}_{fa}T_{(d)} \cdot {}^{fa}_{fi}T \cdot {}^{fi}_{pa}T_{(d)}. \end{aligned} \tag{2.23}$$

The possibility of further simplification is evident in the affine form of Eqn 2.23. That may be reached using a more expanded form of the HTs,

$$\begin{aligned} {}^{tt}_{ta}T_{(m)} &= \begin{bmatrix} & {}^{tt}_{ta}R_{(m)} & & {}^{tt}P^{\circ}_{ta} \\ 0 & 0 & 0 & 1 \end{bmatrix} \quad {}^{tt}_{ta}T_{(d)} = \begin{bmatrix} & {}^{tt}_{ta}R_{(d)} & & {}^{tt}P^{\circ}_{ta} \\ 0 & 0 & 0 & 1 \end{bmatrix} \\ {}^{ta}_{fa}T_{(m)} &= \begin{bmatrix} & {}^{ta}_{fa}R_{(m)} & & \mathbf{0} \\ 0 & 0 & 0 & 1 \end{bmatrix} \quad {}^{ta}_{fa}T_{(d)} = \begin{bmatrix} & {}^{ta}_{fa}R_{(d)} & & \mathbf{0} \\ 0 & 0 & 0 & 1 \end{bmatrix} \\ {}^{fa}_{fi}T &= \begin{bmatrix} & {}^{fa}_{fi}R & & \mathbf{0} \\ 0 & 0 & 0 & 1 \end{bmatrix} \\ {}^{fi}_{pa}T_{(m)} &= \begin{bmatrix} & {}^{fi}_{pa}R_{(m)} & & {}^{fi}P^{\circ}_{pa} \\ 0 & 0 & 0 & 1 \end{bmatrix} \quad {}^{fi}_{pa}T_{(d)} = \begin{bmatrix} & {}^{fi}_{pa}R_{(d)} & & {}^{fi}P^{\circ}_{pa} \\ 0 & 0 & 0 & 1 \end{bmatrix}, \end{aligned} \tag{2.24}$$

to arrive at

$$\begin{aligned} &{}^{tt}P^{\circ}_{ta} + {}^{tt}_{ta}R_{(m)} \cdot {}^{ta}_{fa}R_{(m)} \cdot {}^{fa}_{fi}R \cdot \left({}^{fi}_{pa}R_{(m)} + {}^{fi}P^{\circ}_{pa} \right) \\ &= {}^{tt}P^{\circ}_{ta} + {}^{tt}_{ta}R_{(d)} \cdot {}^{ta}_{fa}R_{(d)} \cdot {}^{fa}_{fi}R \cdot \left({}^{fi}_{pa}R_{(d)} + {}^{fi}P^{\circ}_{pa} \right). \end{aligned} \tag{2.25}$$

${}^{tt}P^{\circ}_{ta}$ cancels out, and the parenthetical terms in Eqn 2.25 may be expanded separately to yield two equations,

$$\begin{aligned} &{}^{tt}_{ta}R_{(m)} \cdot {}^{ta}_{fa}R_{(m)} \cdot {}^{fa}_{fi}R \cdot {}^{fi}_{pa}R_{(m)} \\ &= {}^{tt}_{ta}R_{(d)} \cdot {}^{ta}_{fa}R_{(d)} \cdot {}^{fa}_{fi}R \cdot {}^{fi}_{pa}R_{(d)} \end{aligned} \tag{2.26a}$$

$$\begin{aligned} &{}^{tt}_{ta}R_{(m)} \cdot {}^{ta}_{fa}R_{(m)} \cdot {}^{fa}_{fi}R \cdot {}^{fi}P_{\circ_{pa}} \\ &= {}^{tt}_{ta}R_{(d)} \cdot {}^{ta}_{fa}R_{(d)} \cdot {}^{fa}_{fi}R \cdot {}^{fi}P_{\circ_{pa}}, \end{aligned} \tag{2.26b}$$

which indicate identity of pose between the exploratory and data models when they are both satisfied.

Suppose a particular pose of the data model is chosen, fixing the right hand sides of Eqns 2.26a and 2.26b. Further suppose that, despite different values for ${}^{tt}_{ta}R_{(m)}$ and ${}^{tt}_{ta}R_{(d)}$, values for ${}^{ta}_{fa}E_{y(m)}$ and ${}^{ta}_{fa}E_{z(m)}$ (which create ${}^{ta}_{fa}R_{(m)}$ via Eqn 2.17) may be found which cause Eqn 2.26b to be satisfied. Then, setting

$${}^{fi}_{pa}R_{(m)} = \left({}^{fa}_{fi}R\right)^{-1} \cdot \left({}^{ta}_{fa}R_{(m)}\right)^{-1} \cdot \left({}^{tt}_{ta}R_{(m)}\right)^{-1} \cdot {}^{tt}_{ta}R_{(d)} \cdot {}^{ta}_{fa}R_{(d)} \cdot {}^{fa}_{fi}R \cdot {}^{fi}_{pa}R_{(d)}, \tag{2.27}$$

will also satisfy Eqn 2.26a. Since the three joint angles of the spherical joint ($ {}^{fi}_{pa}E_{x(m)}$, ${}^{fi}_{pa}E_{y(m)}$, and ${}^{fi}_{pa}E_{z(m)}$) are free to vary, they may create an arbitrary rotation matrix ${}^{fi}_{pa}R_{(m)}$ via Eqn 2.10. Consequently, Eqn 2.27 is always feasible, and the exploratory model may produce a pose identical to that of the data model if Eqn 2.26b is satisfied.

Thanks to this simplification, the region of unidentifiability is given by the range over which ${}^{tt}_{ta}E_{(m)}$ and ${}^{tt}_{ta}E_{(d)}$ may differ relative to each other while Eqn 2.26b remains satisfied for every pose in the data set.

2.3.6 The Range of ${}^{tt'}P_{\circ_{pa}}$

If a new frame *tt'* is defined as having the orientation of the *tt* frame and the origin of the *ta* frame, then either side of Eqn 2.26b may be written

$${}^{tt'}P_{\circ_{pa}} = {}^{tt}_{ta}R \cdot {}^{ta}_{fa}R \cdot {}^{fa}_{fi}R \cdot {}^{fi}P_{\circ_{pa}}. \tag{2.28}$$

Examining the range of this quantity will elucidate the circumstances under which Eqn 2.26b is satisfied.

Only the Y component of ${}^{fi}P_{\circ}_{pa}$ is non-zero, and it is given the variable ϕ,

$$ {}^{fi}P_{\circ}_{pa} = \begin{bmatrix} 0 \\ \phi \\ 0 \end{bmatrix}, \tag{2.29} $$

since it represents the length of the femur (think ϕ for femur). ${}^{fa}_{fi}R$ is an elementary rotation about the X axis (See Eqn 2.9),

$$ {}^{fa}_{fi}R = \mathrm{R}\left({}^{fa}_{fi}E_x\right), \tag{2.30} $$

and for compactness we define $\chi = {}^{fa}_{fi}E_x$. ${}^{fa}P_{\circ}_{pa}$ may now be written

$$ {}^{fa}P_{\circ}_{pa} = \begin{bmatrix} 0 \\ \cos(\chi)\phi \\ -\sin(\chi)\phi \end{bmatrix} = \begin{bmatrix} 0 \\ C_\chi\phi \\ -S_\chi\phi \end{bmatrix}. \tag{2.31} $$

Since χ and ϕ are both model parameters, ${}^{fa}P_{\circ}_{pa}$ is a vector of constant length ϕ.

The range of ${}^{tt'}P_{\circ}_{pa}$ is principally determined by the joint angles ${}^{ta}_{fa}E_z$ and ${}^{ta}_{fa}E_y$, which form ${}^{ta}_{fa}R$ by Eqn 2.17; they rotate the vector ${}^{fa}P_{\circ}_{pa}$ about the origin of the *ta* frame. This can be seen in the quantity ${}^{ta}P_{\circ}_{pa} = {}^{ta}_{fa}R \cdot {}^{fa}P_{\circ}_{pa}$,

$$ {}^{ta}P_{\circ}_{pa} = \begin{bmatrix} \cos({}^{ta}_{fa}E_y)\sin({}^{ta}_{fa}E_z)C_\chi\phi + \sin({}^{ta}_{fa}E_y)S_\chi\phi \\ \cos({}^{ta}_{fa}E_z)C_\chi\phi \\ \sin({}^{ta}_{fa}E_y)\sin({}^{ta}_{fa}E_z)C_\chi\phi - \cos({}^{ta}_{fa}E_y)S_\chi\phi \end{bmatrix}. \tag{2.32} $$

The range of ${}^{ta}P_{\circ}_{pa}$ consists of the points on the surface of a sphere with radius ϕ whose Y component lies on the interval $[-C_\chi\phi, C_\chi\phi]$. When χ does not equal 0 or some multiple of π, this range is smaller than $[-\phi, \phi]$, and some points on the spherical surface are unreachable. The unreachable points form two spherical caps with height $\phi\,(1 - C_\chi)$ and base radius $|S_\chi\phi|$. Figure 2.2 shows the reachable portion of the spherical surface lying above the XZ plane for $\phi = 0.4$ meters and $\chi = 10°$. The portion of the surface lying below the XZ plane is a mirror image of the portion lying above it.

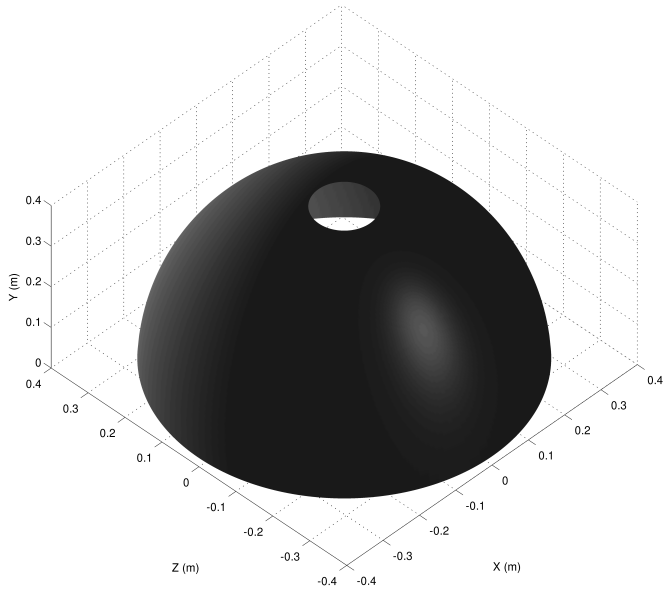

Figure 2.2: **Surface traced by ${}^{ta}P_{\circ}$ for $\phi = 0.4$ meters and $\chi = 10°$.**

The model parameters in ${}^{tt}_{ta}E$ form ${}^{tt}_{ta}R$, which allows for the range of ${}^{tt'}P_{\circ}$ to be rotated relative to the range of ${}^{ta}P_{\circ}$. ${}^{tt'}P_{\circ}$ still traces out points on the surface of a sphere with radius ϕ, but now it cannot reach the points on this surface whose component along the vector ${}^{tt}_{ta}R \cdot \begin{bmatrix} 0 & 1 & 0 \end{bmatrix}^{\mathrm{T}}$ lies outside $[-C_\chi\phi, C_\chi\phi]$. This is relevant to the question of parameter identifiability, as the exploratory model cannot fit all of the poses of the data model if some of them produce a ${}^{tt'}P_{\circ}$ vector that the exploratory model cannot reach. When this occurs will depend on the value of χ, the range of the data model joint angles, and the relative orientation of ${}^{tt}_{ta}R_{(m)}$ and ${}^{tt}_{ta}R_{(d)}$.

2.3.7 Simple Cases of Unidentifiability

There are two ways to demonstrate unidentifiability in the ${}^{tt}_{ta}E$ parameters which apply even without limitations on the joint angles of the data model. Both are presented here as an introduction to the methods used to determine the region of unidentifiability.

The exploratory model is able to fit a particular pose of the data model when Eqn 2.26b

is satisfied. Eqn 2.26b may be rewritten

$$\begin{aligned}
&\left[\left({}^{tt}_{ta}R_{(d)}\right)^{-1}\cdot {}^{tt}_{ta}R_{(m)}\right]\cdot {}^{ta}_{fa}R_{(m)}\cdot {}^{fa}_{fi}R\cdot {}^{fi}P_{\circ}_{pa}\\
&=\left[{}^{ta}_{tt}R_{(d)}\cdot {}^{tt}_{ta}R_{(m)}\right]\cdot {}^{ta}_{fa}R_{(m)}\cdot {}^{fa}_{fi}R\cdot {}^{fi}P_{\circ}_{pa}\\
&=\left[{}^{ta(d)}_{ta(m)}R\right]\cdot {}^{ta}_{fa}R_{(m)}\cdot {}^{fa}_{fi}R\cdot {}^{fi}P_{\circ}_{pa}\\
&={}^{ta}_{fa}R_{(d)}\cdot {}^{fa}_{fi}R\cdot {}^{fi}P_{\circ}_{pa}
\end{aligned} \tag{2.33}$$

where square brackets have been used to highlight the term of interest, ${}^{ta(d)}_{ta(m)}R$. This rotation matrix allows analysis to focus on the relative orientation of the *ta* frames of the exploratory and data models instead of covering all six parameters in ${}^{tt}_{ta}E_{(m)}$ and ${}^{tt}_{ta}E_{(d)}$. Defining

$$\begin{aligned}
{}^{ta}P_{\circ}_{pa(m)} &= {}^{ta}_{fa}R_{(m)}\cdot {}^{fa}_{fi}R\cdot {}^{fi}P_{\circ}_{pa}\\
{}^{ta}P_{\circ}_{pa(d)} &= {}^{ta}_{fa}R_{(d)}\cdot {}^{fa}_{fi}R\cdot {}^{fi}P_{\circ}_{pa},
\end{aligned} \tag{2.34}$$

Eqn 2.33 may be written

$${}^{ta(d)}_{ta(m)}R\cdot {}^{ta}P_{\circ}_{pa(m)} = {}^{ta}P_{\circ}_{pa(d)}, \tag{2.35}$$

where

$${}^{ta}P_{\circ}_{pa(m)} = \begin{bmatrix}\cos({}^{ta}_{fa}E_{y(m)})\sin({}^{ta}_{fa}E_{z(m)})C_{\chi}\phi + \sin({}^{ta}_{fa}E_{y(m)})S_{\chi}\phi\\ \cos({}^{ta}_{fa}E_{z(m)})C_{\chi}\phi\\ \sin({}^{ta}_{fa}E_{y(m)})\sin({}^{ta}_{fa}E_{z(m)})C_{\chi}\phi - \cos({}^{ta}_{fa}E_{y(m)})S_{\chi}\phi\end{bmatrix} \tag{2.36}$$

and

$${}^{ta}P_{\circ}_{pa(d)} = \begin{bmatrix}\cos({}^{ta}_{fa}E_{y(d)})\sin({}^{ta}_{fa}E_{z(d)})C_{\chi}\phi + \sin({}^{ta}_{fa}E_{y(d)})S_{\chi}\phi\\ \cos({}^{ta}_{fa}E_{z(d)})C_{\chi}\phi\\ \sin({}^{ta}_{fa}E_{y(d)})\sin({}^{ta}_{fa}E_{z(d)})C_{\chi}\phi - \cos({}^{ta}_{fa}E_{y(d)})S_{\chi}\phi\end{bmatrix}. \tag{2.37}$$

The region of unidentifiability is defined by the values of ${}^{ta(d)}_{ta(m)}R$ for which Eqn 2.35 can be satisfied for all values of ${}^{ta}P_{\circ}_{pa(d)}$. The simplest case is found by setting $\chi = 0$. In this case, ${}^{ta}P_{\circ}_{pa(d)}$ traces all points on the surface of a sphere with radius ϕ, as does ${}^{ta}P_{\circ}_{pa(m)}$. The exploratory model may then fit any pose of the data model, regardless of the value of ${}^{ta(d)}_{ta(m)}R$. For a model with $\chi = 0$, the parameters ${}^{tt}_{ta}E$ are completely unidentifiable.

The next case applies even when $\chi \neq 0$. If we set ${}^{ta(d)}_{ta(m)}R = \mathrm{R}(E_y)$ (an elementary

rotation about the Y axis, see Eqn 2.9) and use the relations

$$\begin{aligned} \sin(a+b) &= \sin(a)\cos(b) + \cos(a)\sin(b) \\ \cos(a+b) &= \cos(a)\cos(b) - \sin(a)\sin(b), \end{aligned} \tag{2.38}$$

then ${}^{ta(d)}_{ta(m)}R \cdot {}^{ta}P_{\circ_{pa(m)}}$ becomes

$$\begin{bmatrix} \cos({}^{ta}_{fa}E_{y(m)} + E_y)\sin({}^{ta}_{fa}E_{z(m)})C_\chi\phi + \sin({}^{ta}_{fa}E_{y(m)} + E_y)S_\chi\phi \\ \cos({}^{ta}_{fa}E_{z(m)})C_\chi\phi \\ \sin({}^{ta}_{fa}E_{y(m)} + E_y)\sin({}^{ta}_{fa}E_{z(m)})C_\chi\phi - \cos({}^{ta}_{fa}E_{y(m)} + E_y)S_\chi\phi \end{bmatrix}. \tag{2.39}$$

This quantity has the same range as ${}^{ta}P_{\circ_{pa(d)}}$ regardless of the value chosen for E_y. Since the points unreachable by ${}^{ta}P_{\circ_{pa(m)}}$ are those whose component along the Y axis of *ta* lies outside of $[-C_\chi\phi, C_\chi\phi]$, rotating the *ta* frame of the exploratory model about its Y axis will not affect its fit to the data set.

For the sake of later analysis, ${}^{ta(d)}_{ta(m)}R$ is formed using the Y-X-Z sequence,

$${}^{ta(d)}_{ta(m)}R = \mathrm{R}\left({}^{(d)}_{(m)}E_z\right) \cdot \mathrm{R}\left({}^{(d)}_{(m)}E_x\right) \cdot \mathrm{R}\left({}^{(d)}_{(m)}E_y\right), \tag{2.40}$$

resulting in the matrix

$${}^{ta(d)}_{ta(m)}R = \begin{bmatrix} C_zC_y + S_zS_xS_y & S_zC_x & -C_zS_y + S_zS_xC_y \\ -S_zC_y + C_zS_xS_y & C_zC_x & S_zS_y + C_zS_xC_y \\ C_xS_y & -S_x & C_xC_y \end{bmatrix}, \tag{2.41}$$

where S_x abbreviates $\sin\left({}^{(d)}_{(m)}E_x\right)$, and so on. Since the rotation parameterized by ${}^{(d)}_{(m)}E_y$ is first in the sequence, it occurs about the Y axis of the *ta* frame of the exploratory model and corresponds to the mechanism of unidentifiability described above. A related feature of the Y-X-Z sequence is that the second column of ${}^{ta(d)}_{ta(m)}R$, which gives the Y axis of *ta(m)* in *ta(d)* coordinates, only depends on the Cardan angles ${}^{(d)}_{(m)}E_x$ and ${}^{(d)}_{(m)}E_z$.

The above two cases of unidentifiability apply even when the data model joint angles ${}^{ta}_{fa}E_{z(d)}$ and ${}^{ta}_{fa}E_{y(d)}$ are allowed vary from 0° to 360°. Additional mechanisms of unidentifi-

ability will arise if the range of these joint angles is limited.

2.3.8 Accounting for Knee Range of Motion

The range of poses in the data set is given by the range of values taken on by the joint angles of the data model. Since the ability of the exploratory model to fit a given pose of the data model does not depend on the joint angles of the spherical joint, ${}^{fi}_{pa}E$, these will be neglected in considering the range of the data set. The remaining joint angles are ${}^{ta}_{fa}E_{z(d)}$ and ${}^{ta}_{fa}E_{y(d)}$, which model flexion/extension (FL/EX) and internal/external rotation (IN/EX) of the human knee, respectively.

In this analysis, knee FL/EX is limited to a range from 5° of hyper extension to 130° of flexion, following [13, p. 443]. This results in a range of $[-130°, 5°]$ for ${}^{ta}_{fa}E_{z(d)}$, since flexion receives a negative value in the chosen Cardan convention.

Internal/external rotation has a limited range which is dependent upon knee flexion. Blankevoort, et al. tested this range on several knee specimens by measuring the amount of IN/EX produced by the tibia at various degrees of flexion when loaded with a torque of ±3 Nm. The data for specimen 2 have been adapted from the graph in Figure 5 of [1] and are reproduced in Table 2.1. They are used in this work to define the positive and negative limits on the range of ${}^{ta}_{fa}E_{y(d)}$ in the data set.

Table 2.1: **Positive and negative limits of IN/EX at various degrees of FL/EX**

Flexion Angle	IN/EX limit	Flexion Angle	IN/EX limit
0°	−7.3°	0°	8.2°
−5°	−12.6°	–	–
−10°	−14.9°	−10°	14.0°
−17.5°	−17.2°	−20°	20.0°
−30°	−19.1°	−34°	23.1°
−58°	−20.5°	−63°	24.0°
−84°	−21.9°	−88°	24.5°
−92°	−21.4°	−95°	25.4°
−120°	−21.4°	−120°	25.4°

The last row in Table 2.1 is not in the original data but was added to allow the data to be extrapolated to the interval ${}^{ta}_{fa}E_{z(d)} \in [-130°, 5°]$ with the help of splines. The splines

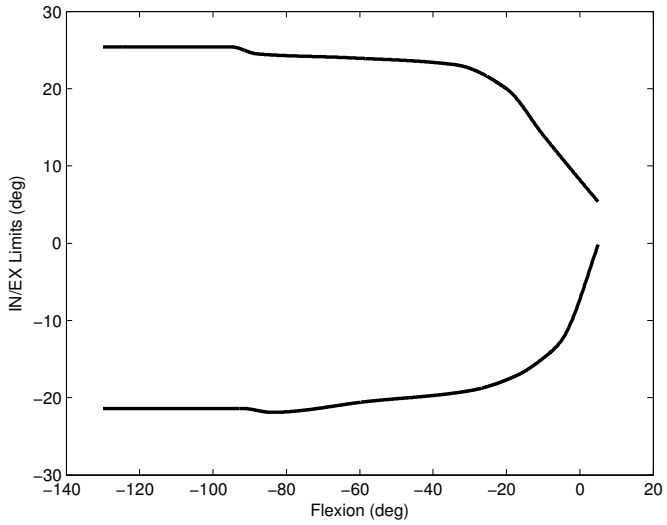

Figure 2.3: **Positive and negative limits of ${}^{ta}_{fa}E_y$ for ${}^{ta}_{fa}E_z \in [-130°, 5°]$**

are represented with function notation, where

$$\mathrm{S_P}\left({}^{ta}_{fa}E_{z(d)}\right) \tag{2.42}$$

gives the positive limit of ${}^{ta}_{fa}E_{y(d)}$ for a given flexion angle,

$$\mathrm{S_N}\left({}^{ta}_{fa}E_{z(d)}\right) \tag{2.43}$$

gives the negative limit, and the two quantities

$$\begin{aligned} &\mathrm{S_P}'\left({}^{ta}_{fa}E_{z(d)}\right) \\ &\mathrm{S_N}'\left({}^{ta}_{fa}E_{z(d)}\right) \end{aligned} \tag{2.44}$$

are the first derivatives of the functions above. $\mathrm{S_P}\left({}^{ta}_{fa}E_{z(d)}\right)$ and $\mathrm{S_N}\left({}^{ta}_{fa}E_{z(d)}\right)$ are both plotted in Figure 2.3.

When the limits on FL/EX and IN/EX are taken into account, the vector ${}^{ta}P^{\circ}_{pa(d)}$ traces out the surface shown in Figure 2.4. This is still a portion of the surface of a sphere with radius ϕ, but now it looks like a peel from a slice of fruit. It is, however, a good approximation to the range of values that ${}^{ta}P^{\circ}_{pa(d)}$ could possibly have in a measured data set.

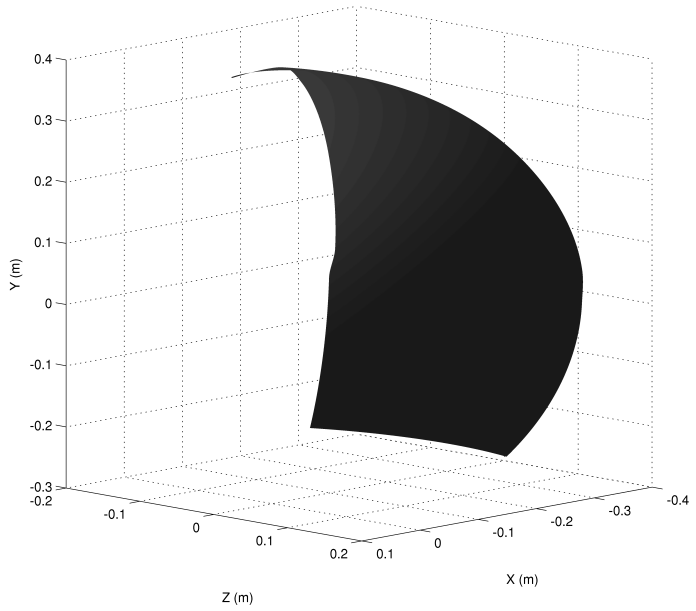

Figure 2.4: **Surface traced by ${}^{ta}P_{\mathring{pa}}$ for $\phi = 0.4$ meters and $\chi = 4°$ with knee range of motion taken into account.**

2.3.9 Bracketing the Region of Unidentifiability

The exploratory model is able to produce a pose identical to that of the data model when Eqn 2.35,

$$ {}^{ta(d)}_{ta(m)}R \cdot {}^{ta}P_{\mathring{pa}(m)} = {}^{ta}P_{\mathring{pa}(d)}, $$

is satisfied. The region of unidentifiability is given by the definitions of ${}^{ta(d)}_{ta(m)}R$ which allow the range of the left hand side of Eqn 2.35 to overlap the range of the right hand side. Recall from the discussion following Eqn 2.32 that ${}^{ta}P_{\mathring{pa}(m)}$ cannot reach points whose component along the Y axis of *ta* lies outside $[-C_\chi\phi, C_\chi\phi]$. The last points reachable by ${}^{ta}P_{\mathring{pa}(m)}$ form two circles of radius $|S_\chi\phi|$ centered about the Y axis of *ta* and lying in the XZ plane; one has Y coordinate of $C_\chi\phi$, the other has Y coordinate $-C_\chi\phi$. These are called the positive and negative feasible limit circles. The positive feasible limit circle is found by setting

${}^{ta}_{fa}E_{z(m)} = 0$ in Eqn 2.36, yielding

$$ {}^{ta}P_{\overset{\circ}{pa}(m)} = \begin{bmatrix} \sin\left({}^{ta}_{fa}E_{y(m)}\right) S_\chi\phi \\ C_\chi\phi \\ -\cos\left({}^{ta}_{fa}E_{y(m)}\right) S_\chi\phi \end{bmatrix}, \tag{2.45} $$

and the negative feasible limit circle is found by setting ${}^{ta}_{fa}E_{z(m)} = 180°$. ${}^{ta(d)}_{ta(m)}R$ causes the positive feasible limit circle to be centered around the point

$$ V_{c\chi\phi} = {}^{ta(d)}_{ta(m)}R \cdot \begin{bmatrix} 0 \\ C_\chi\phi \\ 0 \end{bmatrix} \tag{2.46} $$

and the negative feasible limit circle to be centered around $-V_{c\chi\phi}$. The border of the region of unidentifiability is given by all of the definitions of ${}^{ta(d)}_{ta(m)}R$ which cause one of the feasible limit circles to lie tangent to the outside edge of the data set in such a way that $\pm V_{c\chi\phi}$ is bounded away from the data set. This section develops a procedure to find such definitions of ${}^{ta(d)}_{ta(m)}R$, beginning with a mathematical description of the outside edge of the data set.

2.3.9.1 Outlining the data set

This outside edge of the data set is given by four contours, all of which are produced by ${}^{ta}P_{\overset{\circ}{pa}(d)}$ (See Eqn 2.37) at the maximal limits of ${}^{ta}_{fa}E_{y(d)}$ and ${}^{ta}_{fa}E_{z(d)}$. Contour A is given by the full range of flexion and the positive IN/EX limit,

$$ \begin{aligned} {}^{ta}_{fa}E_{z(d)} &\in [-130°, 5°] \\ {}^{ta}_{fa}E_{y(d)} &= \mathrm{S_P}\left({}^{ta}_{fa}E_{z(d)}\right). \end{aligned} \tag{2.47} $$

Contour B is given by the full range of flexion and the negative IN/EX limit,

$$ \begin{aligned} {}^{ta}_{fa}E_{z(d)} &\in [-130°, 5°] \\ {}^{ta}_{fa}E_{y(d)} &= \mathrm{S_N}\left({}^{ta}_{fa}E_{z(d)}\right). \end{aligned} \tag{2.48} $$

Contour C is given by the maximum range of IN/EX at the positive limit of flexion,

$$\begin{aligned} {}^{ta}_{fa}E_{z(d)} &= 5^\circ \\ {}^{ta}_{fa}E_{y(d)} &\in [\mathrm{S_N}\left(5^\circ\right), \mathrm{S_P}\left(5^\circ\right)], \end{aligned} \tag{2.49}$$

and contour D is given by the maximum range of IN/EX at the negative limit of flexion,

$$\begin{aligned} {}^{ta}_{fa}E_{z(d)} &= -130^\circ \\ {}^{ta}_{fa}E_{y(d)} &\in [\mathrm{S_N}\left(-130^\circ\right), \mathrm{S_P}\left(-130^\circ\right)]. \end{aligned} \tag{2.50}$$

Contours A and B are parametric curves in ${}^{ta}_{fa}E_{z(d)}$, while contours C and D are parametric in ${}^{ta}_{fa}E_{y(d)}$. It is handy to give them the following functional forms

$$\begin{aligned} &\mathrm{C_A}\left({}^{ta}_{fa}E_{z(d)}\right) \qquad \mathrm{C_B}\left({}^{ta}_{fa}E_{z(d)}\right) \\ &\mathrm{C_C}\left({}^{ta}_{fa}E_{y(d)}\right) \qquad \mathrm{C_D}\left({}^{ta}_{fa}E_{y(d)}\right). \end{aligned} \tag{2.51}$$

The points on contour A are given by the equation

$$\mathrm{C_A}\left(\zeta\right) = \begin{bmatrix} \cos\left(\mathrm{S_P}(\zeta)\right)\sin(\zeta)C_\chi\phi + \sin\left(\mathrm{S_P}(\zeta)\right)S_\chi\phi \\ \cos\left(\zeta\right)C_\chi\phi \\ \sin\left(\mathrm{S_P}(\zeta)\right)\sin(\zeta)C_\chi\phi - \cos\left(\mathrm{S_P}(\zeta)\right)S_\chi\phi \end{bmatrix}, \tag{2.52}$$

where ζ stands for ${}^{ta}_{fa}E_{z(d)}$. The tangent vector to this contour at ζ is given by

$$\nabla\,\mathrm{C_A}\left(\zeta\right) = \begin{bmatrix} \left[\cos(\zeta)\cos\left(\mathrm{S_P}(\zeta)\right) - \sin(\zeta)\sin\left(\mathrm{S_P}(\zeta)\right)\mathrm{S_P}'(\zeta)\right]C_\chi\phi + \cos\left(\mathrm{S_P}(\zeta)\right)\mathrm{S_P}'(\zeta)S_\chi\phi \\ -\sin(\zeta)C_\chi\phi \\ \left[\cos(\zeta)\sin\left(\mathrm{S_P}(\zeta)\right) + \sin(\zeta)\cos\left(\mathrm{S_P}(\zeta)\right)\mathrm{S_P}'(\zeta)\right]C_\chi\phi + \sin\left(\mathrm{S_P}(\zeta)\right)\mathrm{S_P}'(\zeta)S_\chi\phi \end{bmatrix}. \tag{2.53}$$

The equations for $\mathrm{C_B}\left(\zeta\right)$ and $\nabla\,\mathrm{C_B}\left(\zeta\right)$ are given by replacing $\mathrm{S_P}(\zeta)$ and $\mathrm{S_P}'(\zeta)$ with $\mathrm{S_N}(\zeta)$ and $\mathrm{S_N}'(\zeta)$ in Eqns 2.52 and 2.53. Contours C and D are both given by Eqn 2.37 with ${}^{ta}_{fa}E_{z(d)}$ and ${}^{ta}_{fa}E_{y(d)}$ set according to Eqn 2.49 and 2.50, respectively. The tangent vector

equation for contours C and D is given by

$$\begin{bmatrix} -\sin(\zeta)\sin(\gamma)\,C_\chi\phi + \cos(\gamma)\,S_\chi\phi \\ 0 \\ \sin(\zeta)\cos(\gamma)\,C_\chi\phi + \sin(\gamma)\,S_\chi\phi \end{bmatrix}, \tag{2.54}$$

where γ stands for ${}^{ta}_{fa}E_{y(d)}$, and ζ is set to 5° for $\nabla \mathrm{C_C}(\gamma)$ and to -130° for $\nabla \mathrm{C_D}(\gamma)$.

2.3.9.2 A Caveat

Contours A and B have an intersection near $\zeta = 0^\circ$, even though the data set has a non-zero width at this point. This violates the assumption that contours A and B give the outer edges of the data set. For representative model parameters $\chi = 4^\circ$ and $\phi = 0.4$ meters, the intersection of contours A and B is given by

$$\mathrm{C_A}(-0.5265^\circ) = \mathrm{C_B}(0.5328^\circ) = \begin{bmatrix} 0.0005 \\ 0.3990 \\ -0.0281 \end{bmatrix} \tag{2.55}$$

The point given by ${}^{ta}P_{\circ_{pa(d)}}$ for ${}^{ta}_{fa}E_{z(d)} = {}^{ta}_{fa}E_{y(d)} = 0$ is nearby this intersection and also in the data set; its value is

$${}^{ta}P_{\circ_{pa(d)}} = \begin{bmatrix} 0 \\ 0.3990 \\ -0.0279 \end{bmatrix}. \tag{2.56}$$

The data set is plotted for ζ from -0.6° to 0.6° in Figure 2.5. Points which bound the portion of the data set not encompassed by contours A and B are highlighted, including points near the two listed above. The area not bounded by the contours has a maximum extent in the X direction of about 6.5mm and a maximum extent in the Z direction of about 0.4mm; there is no appreciable variation in the Y direction. Taking this area into account would greatly complicate the analysis. However, it is so small that it will have minimal effect on the determination of the region of unidentifiability. On the balance of these two considerations, it is neglected.

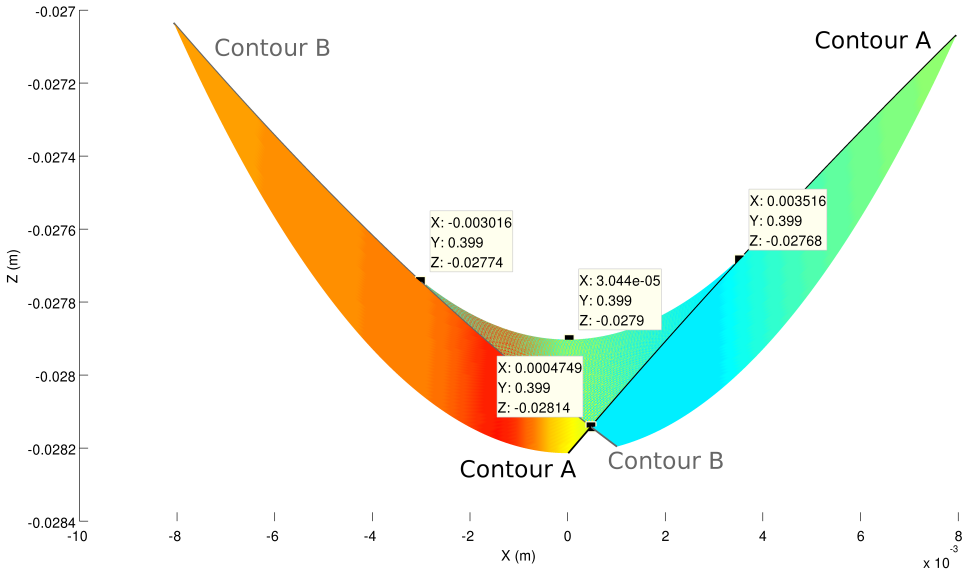

Figure 2.5: **Data set surface and contours A (black line) and B (gray line) for ζ from $-0.6°$ to $0.6°$.** Data tips surround region of surface not bounded by contours A and B. Points near intersection of contours A and B and near ${}^{ta}P_{\overset{\circ}{pa}(d)}$ at zero FL/EX and IN/EX also shown.

2.3.9.3 Finding $V_{c\chi\phi}$ and ${}^{ta(d)}_{ta(m)}R$

This section develops the procedure to find a value of $V_{c\chi\phi}$ which causes the positive feasible limit circle to lie tangent to any of the contours outlining the data set, given a point on the contour. This procedure is set forth using contour A, but it generalizes to all four contours. This section also describes a method for finding a definition of ${}^{ta(d)}_{ta(m)}R$ which produces $V_{c\chi\phi}$.

When the positive feasible limit circle is tangent to the contour A at some point $\mathrm{C_A}(\zeta)$, there is a vector $\mathbf{v}$ corresponding to a value of ${}^{ta}_{fa}E_{y(m)}$ in Eqn 2.45 with the properties

$$V_{c\chi\phi} = \mathrm{C_A}(\zeta) + \mathbf{v} \tag{2.57a}$$

$$\|\mathbf{v}\| = |S_\chi \phi| \tag{2.57b}$$

$$\mathbf{v} \perp \nabla \mathrm{C_A}(\zeta) \tag{2.57c}$$

$$\mathbf{v} \perp V_{c\chi\phi}. \tag{2.57d}$$

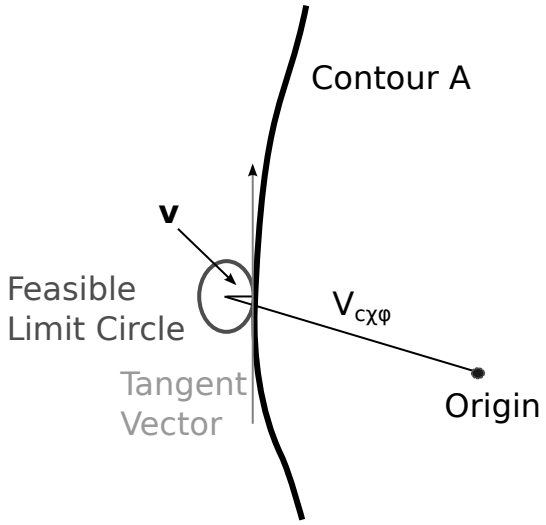

Figure 2.6: **Diagram of positive feasible limit circle tangent to contour A.**

This situation is shown graphically in Figure 2.6. Given a value of ζ, $\mathbf{v}$ may be found based on its own properties as well as those of the contour and tangent vector. Once $\mathbf{v}$ is found, $V_{c\chi\phi}$ follows from Eqn 2.57a.

Since $\mathrm{C_A}(\zeta)$ connects the origin of the data model's *ta* frame to a point on the surface of a sphere centered around the same origin, and $\nabla \mathrm{C_A}(\zeta)$ lies in the plane which is tangent to that sphere at point $\mathrm{C_A}(\zeta)$,

$$\mathrm{C_A}(\zeta) \perp \nabla \mathrm{C_A}(\zeta). \tag{2.58}$$

By defining

$$\mathbf{v}_0 = \frac{|S_\chi \phi| \cdot \mathrm{C_A}(\zeta)}{\|\mathrm{C_A}(\zeta)\|}, \tag{2.59}$$

we arrive at a vector with the properties of Eqns 2.57b and 2.57c. Both properties are retained if $\mathbf{v}_0$ is rotated about $\nabla \mathrm{C_A}(\zeta)$ by an angle θ,

$$\mathbf{v}_{rot}(\theta) = \mathbf{v}_0 \cos(\theta) + \left(\frac{\nabla \mathrm{C_A}(\zeta)}{\|\nabla \mathrm{C_A}(\zeta)\|} \times \mathbf{v}_0 \right) \sin(\theta), \tag{2.60}$$

which is made convenient by Rodrigues' formula. Solving the equation

$$\|\mathrm{C_A}(\zeta) + \mathbf{v}_{rot}(\theta)\| = C_\chi \phi \tag{2.61}$$

for θ will yield a candidate solution, $\mathbf{v}_{rot}(\theta)$, for the desired vector $\mathbf{v}$. There are two solutions to Eqn 2.61, both produce a vector $V_{c\chi\phi}$ (through Eqn 2.57a) which causes the positive feasible limit circle to lie tangent to contour A. One of these solutions allows unreachable points of the exploratory model to lie within the feasible region of the data set, while the other does not. This second solution, which keeps $V_{c\chi\phi}$ bounded away from the data set, is the desired solution. In the case of contour A, the desired $\mathbf{v}$ vector is found near $\theta = -90°$ for ${}^{ta}_{fa}E_{z(d)} < 0$ and near $\theta = 90°$ for ${}^{ta}_{fa}E_{z(d)} > 0$. For countour B, the opposite is true. For contours C and D, the desired $\mathbf{v}$ vector is found near $\theta = -90°$.

Once $\mathbf{v}$ and consequently $V_{c\chi\phi}$ have been found by the procedure above, it is desirable to find a definition of ${}^{ta(d)}_{ta(m)}R$ which produces $V_{c\chi\phi}$ (See Eqn 2.46). Since ${}^{ta(d)}_{ta(m)}R$ is defined via a Y-X-Z sequence (See Eqn 2.40), $V_{c\chi\phi}$ may be written

$$V_{c\chi\phi} = \begin{bmatrix} S_z C_x C_\chi \phi \\ C_z C_x C_\chi \phi \\ -S_x C_\chi \phi \end{bmatrix}, \tag{2.62}$$

where S_z abbreviates $\sin\left({}^{(d)}_{(m)}E_z\right)$, and so on. From the discussion surrounding Eqn 2.39, the Cardan angle ${}^{(d)}_{(m)}E_y$ may vary freely without causing ${}^{ta(d)}_{ta(m)}R$ to exit the region of unidentifiability. The other two Cardan angles may be derived from the vector $V_{c\chi\phi}$ according to

$$\begin{aligned} {}^{(d)}_{(m)}E_z &= \operatorname{atan2}\left(V_{c\chi\phi}(x), V_{c\chi\phi}(y)\right) \\ C_z &= \cos\left({}^{(d)}_{(m)}E_z\right) \quad S_z = \sin\left({}^{(d)}_{(m)}E_z\right) \\ {}^{(d)}_{(m)}E_x &= \begin{cases} \operatorname{atan2}\left(-V_{c\chi\phi}(z), V_{c\chi\phi}(y)/C_z\right), & \text{if } |C_z| > |S_z| \\ \operatorname{atan2}\left(-V_{c\chi\phi}(z), V_{c\chi\phi}(x)/S_z\right), & \text{otherwise.} \end{cases} \end{aligned} \tag{2.63}$$

The definition of ${}^{ta(d)}_{ta(m)}R$ which causes the *negative* feasible limit circle to lie tangent to the feasible region of the data set may be found with only one adjustment to the entire procedure

above: The cardan angles for ${}^{ta(d)}_{ta(m)}R$ are derived using the equations

$$\begin{aligned}
{}^{(d)}_{(m)}E_z &= \operatorname{atan2}\left(-V_{c\chi\phi}(x), -V_{c\chi\phi}(y)\right) \\
C_z &= \cos\left({}^{(d)}_{(m)}E_z\right) \quad S_z = \sin\left({}^{(d)}_{(m)}E_z\right) \\
{}^{(d)}_{(m)}E_x &= \begin{cases} \operatorname{atan2}\left(V_{c\chi\phi}(z), -V_{c\chi\phi}(y)/C_z\right), & \text{if } |C_z| > |S_z| \\ \operatorname{atan2}\left(V_{c\chi\phi}(z), -V_{c\chi\phi}(y)/S_z\right), & \text{otherwise,} \end{cases}
\end{aligned} \tag{2.64}$$

which treat all components of $V_{c\chi\phi}$ as if they have the opposite sign.

In either case, ${}^{ta(d)}_{ta(m)}R$ is formed from ${}^{(d)}_{(m)}E_x$ and ${}^{(d)}_{(m)}E_z$ according to Eqn 2.40, with ${}^{(d)}_{(m)}E_y$ free to vary.

2.3.10 Exploring the Region of Unidentifiability

Now that the limits of the region of unidentifiability can be found, they may be used to explore its full extent. Some definitions will make this easier. If ${}^{ta(d)}_{ta(m)}R$ is defined such that it causes the positive feasible limit circle of the exploratory model to lie tangent to contour A at $\mathrm{C_A}(\zeta)$, the vector $V_{PA}(\zeta)$ is given by the second column of ${}^{ta(d)}_{ta(m)}R$ – a unit vector pointing in the direction of $V_{c\chi\phi}$. Similarly, $V_{NB}(\zeta)$ is given as the second column of ${}^{ta(d)}_{ta(m)}R$ when that matrix causes the negative feasible limit circle to lie tangent to contour B at ζ. Since $V_{c\chi\phi}$ was defined in the positive direction in Eqn 2.46, $V_{NB}(\zeta)$ is a unit vector pointing toward the center of the positive feasible limit circle. As before, $\zeta = {}^{ta}_{fa}E_{z(d)}$.

$V_{PA}(\zeta)$ and $V_{NB}(\zeta)$ correspond to limiting cases for the definition of ${}^{ta(d)}_{ta(m)}R$ within the region of unidentifiability. A larger portion of that region can be explored by interpolating between these cases, the procedure for which follows next. For a given ζ, the angle between $V_{PA}(\zeta)$ and $V_{NB}(\zeta)$ is given by

$${}^{NB}_{PA}A(\zeta) = \operatorname{acos}\left(V_{PA}(\zeta)^{\mathrm{T}} \cdot V_{NB}(\zeta)\right), \tag{2.65}$$

while the unit vector

$${}^{NB}_{PA}K(\zeta) = \frac{V_{PA}(\zeta) \times V_{NB}(\zeta)}{\|V_{PA}(\zeta) \times V_{NB}(\zeta)\|} \tag{2.66}$$

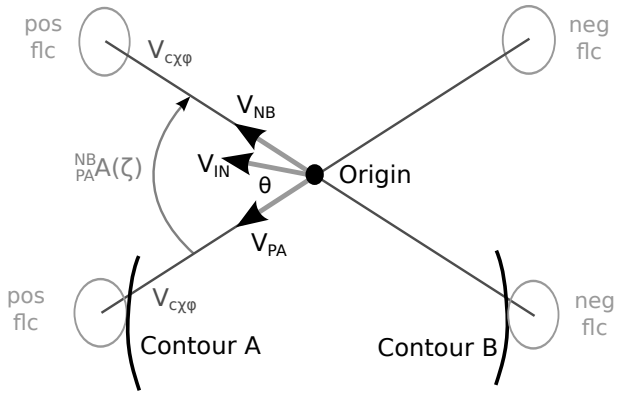

Figure 2.7: **Diagram of interpolation between V_{PA} and V_{NB}.** *flc* stands for feasible limit circle.

is mutually orthogonal to $V_{PA}(\zeta)$ and $V_{NB}(\zeta)$. An intermediate vector $V_{IN}(\zeta, \theta)$ given by the rotation of $V_{PA}(\zeta)$ about ${}^{NB}_{PA}K(\zeta)$,

$$V_{IN}(\zeta, \theta) = V_{PA}(\zeta)\cos(\theta) + \left({}^{NB}_{PA}K(\zeta) \times V_{PA}(\zeta)\right)\sin(\theta), \tag{2.67}$$

over the interval

$$\theta \in [0, {}^{NB}_{PA}A(\zeta)] \tag{2.68}$$

interpolates between $V_{PA}(\zeta)$ and $V_{NB}(\zeta)$. For each θ, it can be used to produce a ${}^{ta(d)}_{ta(m)}R$ matrix which lies within the region of unidentifiability. This is done by plugging $V_{IN}(\zeta, \theta)$ into Eqn 2.63 in place of $V_{c\chi\phi}$ and using the resultant Cardan angles in Eqn 2.40.

A simple diagram of the procedure above is shown in Figure 2.7. The procedure works for opposite contours on the edge of the feasible region of the data set: either contours A and B or contours C and D. It may also be applied to the vector pairs $V_{PB}(\zeta)$ and $V_{NA}(\zeta)$. For contours C and D, the rotation caused by $\gamma = {}^{ta}_{fa}E_{y(d)}$ has an opposite directional effect for $\zeta > 0$ compared with $\zeta < 0$. Since $\zeta = 5°$ for contour C and $-130°$ for contour D, it is helpful to allow separate γ values for these two contours. Thus, $V_{PC}(\gamma_C)$ may be compared with $V_{ND}(\gamma_D)$, and $V_{PD}(\gamma_D)$ with $V_{NC}(\gamma_C)$. Consequently, the functions ${}^{ND}_{PC}A(\gamma_C, \gamma_D)$ and ${}^{PD}_{NC}A(\gamma_C, \gamma_D)$ take two arguments, but they are otherwise defined as in Eqn 2.65.

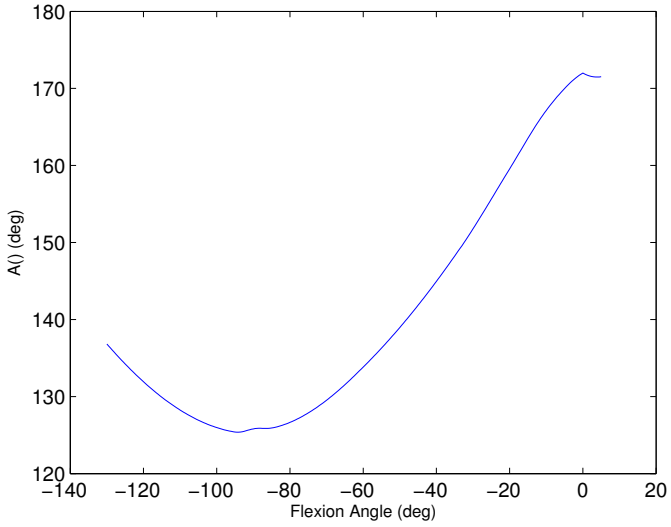

Figure 2.8: ${}^{NB}_{PA}A(\zeta)$ **for** $\zeta \in [-130°, 5°]$**.**

2.4 Results

Applying some reasonable values to the quantities χ and ϕ, this section will provide numerical results which quantify the extent of the region of unidentifiability.

ϕ represents the length of the femur. Measurement of one of the author's femurs from lateral condyle to greater trochanter yields a value of approximately 40cm. Expressed in meters, this gives $\phi = 0.4$. Recall that $\chi = {}^{fa}_{fi}E_x$; it represents the angle between the knee flexion axis and the vector pointing from the KJC to the HJC. These quantities are expected to be close to perpendicular [20], resulting in the estimate $\chi = 0$. This case has been covered in the discussion following Eqn 2.37, and it isn't very interesting. We proceed with a nearby but non-zero value $\chi = 4°$.

Figure 2.8 shows the value of ${}^{NB}_{PA}A(\zeta)$ for $\zeta = {}^{ta}_{fa}E_{z(d)}$ varying from $-130°$ to $5°$. ${}^{NB}_{PA}A(\zeta)$ represents the amount of rotation permitted in ${}^{ta(d)}_{ta(m)}R$ between the positive feasible limit circle lying tangent to contour A and the negative feasible limit circle lying tangent to contour B. Figure 2.9 shows a scatter plot of the Cardan angles ${}^{(d)}_{(m)}E_x$ and ${}^{(d)}_{(m)}E_z$ as one interpolates between these limits for $\zeta = -45°$. The angles ${}^{(d)}_{(m)}E_x \approx 24°$ and ${}^{(d)}_{(m)}E_z \approx -45°$ correspond to $V_{PA}(-45°)$, while the angles ${}^{(d)}_{(m)}E_x \approx 14°$ and ${}^{(d)}_{(m)}E_z \approx 137°$ correspond to $V_{NB}(-45°)$; ${}^{NB}_{PA}A(-45°) \approx 142°$.

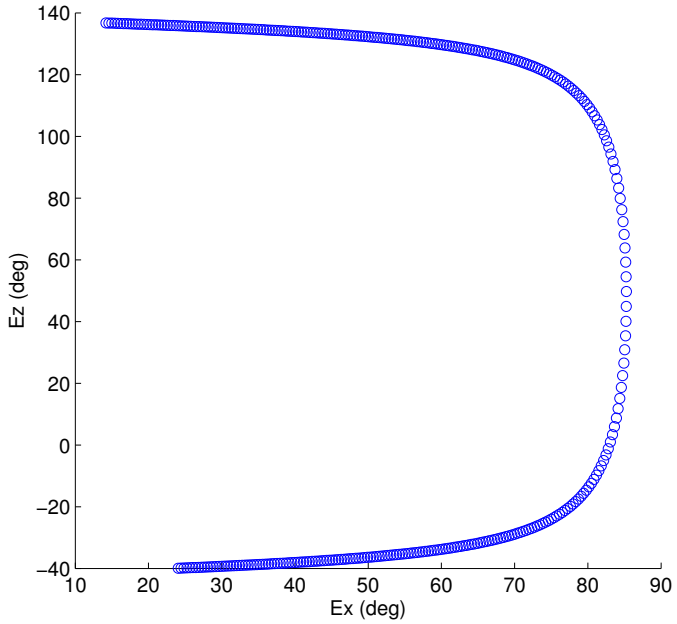

Figure 2.9: **Cardan angles ${}^{(d)}_{(m)}E_x$ and ${}^{(d)}_{(m)}E_z$ which produce a ${}^{ta(d)}_{ta(m)}R$ matrix within the region of unidentifiability.** Found by interpolation between contours A and B at $\zeta = -45°$.

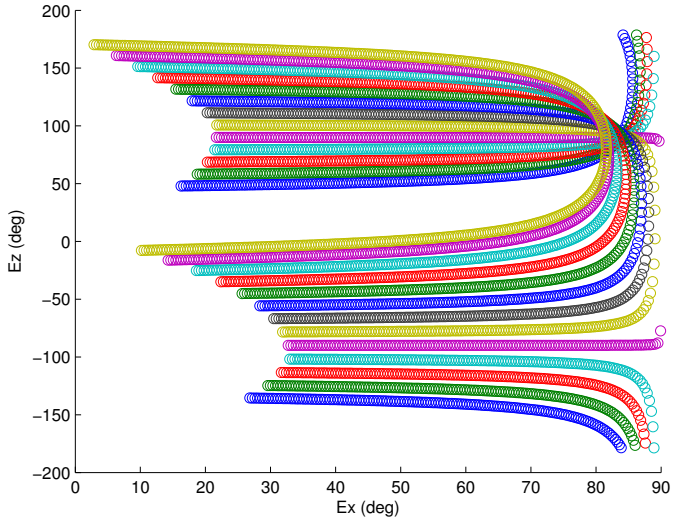

Figure 2.10: **Cardan angles ${}^{(d)}_{(m)}E_x$ and ${}^{(d)}_{(m)}E_z$ which produce a ${}^{ta(d)}_{ta(m)}R$ matrix within the region of unidentifiability.** Found by interpolation between contours A and B at multiple values of ζ.

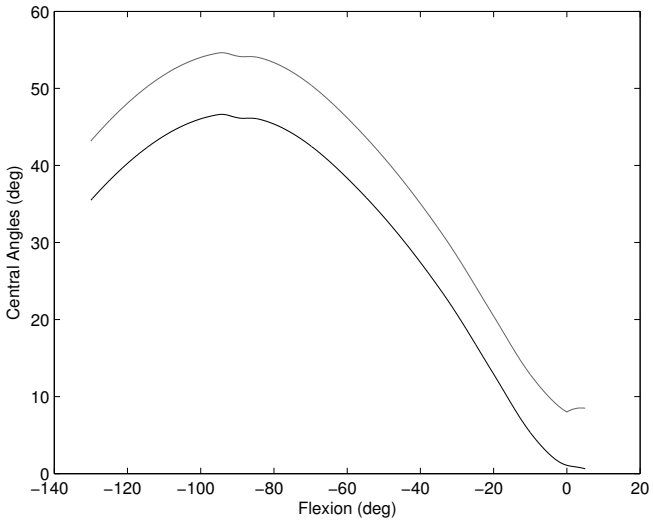

Figure 2.11: **Angle between $V_{PA}(\zeta)$ and $V_{PB}(\zeta)$ (gray) as well as between $\mathrm{C_A}(\zeta)$ and $\mathrm{C_B}(\zeta)$ (black).**

Figure 2.10 shows a stack of scatter plots of ${}^{(d)}_{(m)}E_x$ and ${}^{(d)}_{(m)}E_z$, derived by interpolation as above, for ζ ranging from $-120°$ to $-10°$ at 10 degree intervals. The point of this figure is that ${}^{ta(d)}_{ta(m)}R$ may vary quite broadly without affecting the ability of the exploratory model to fit the data set. Interpolating between $V_{NA}(\zeta)$ and $V_{PB}(\zeta)$ would show even more of this range, adding negative values for ${}^{(d)}_{(m)}E_x$.

It is helpful to compare the angle between $\mathrm{C_A}(\zeta)$ and $\mathrm{C_B}(\zeta)$ with the angle between $V_{PA}(\zeta)$ and $V_{PB}(\zeta)$, as Figure 2.11 does. The difference between the two for a given flexion angle shows how far the exploratory model must be bounded away from the data set. This value ranges between approximately 7 and 8 degrees. It is not always 8 degrees, as one might expect from the value $\chi = 4°$, due to the curvature of $\mathrm{C_A}(\zeta)$ and $\mathrm{C_B}(\zeta)$.

The angle ${}^{ND}_{PC}A(\gamma_C, \gamma_D)$ gives a sense of how far ${}^{ta(d)}_{ta(m)}R$ may vary between the positive feasible limit circle lying tangent to contour C and the negative one lying tangent to contour D. For $\gamma_C = 2°$ and $\gamma_D = -14°$, ${}^{ND}_{PC}A$ is about $37°$. This value is expected, as ζ has a range of $135°$, and $180° - 135° - 8° = 37°$. A plot of the Cardan angles found by interpolation between $V_{PC}(2°)$ and $V_{ND}(-14°)$ is shown in Figure 2.12. The values for γ were chosen so that interpolation would cause ${}^{(d)}_{(m)}E_z$ to change much and ${}^{(d)}_{(m)}E_x$ to change little.

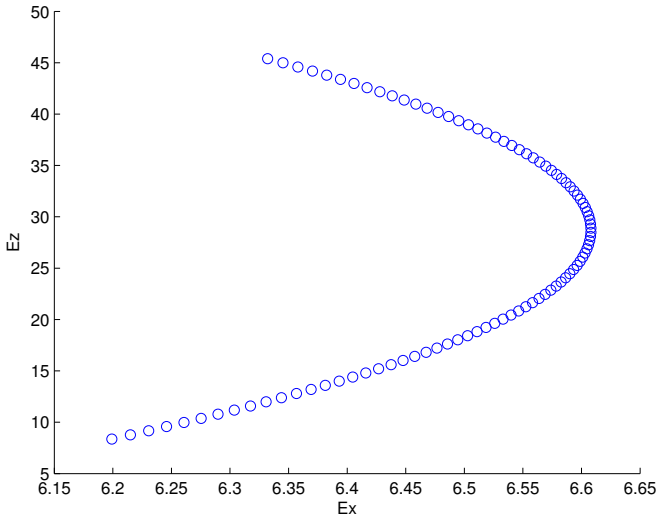

Figure 2.12: **Cardan angles ${}^{(d)}_{(m)}E_x$ and ${}^{(d)}_{(m)}E_z$ which produce a ${}^{ta(d)}_{ta(m)}R$ matrix within the region of unidentifiability.** Found by interpolation between contours C and D.

2.5 Discussion

The 5 DoF model has an intended application in the estimatiion of joint parameters at the hip and knee as part of an optimization method. This section focuses on the consequences of parameter unidentifiability for this application of the 5 DoF model. Recall that an optimization method estimates a subject's joint parameters by finding the model parameters which allow the kinematic model to best reproduce, or fit, the subject's movement data. In the analysis above, the model parameters of the data model represent the true joint parameters of the subject, while the data set takes the place of the subject's movement data. The exploratory model stands in for the model that would be fitted to the subject's movement data.

Much of the analysis above focused on the rotation matrix ${}^{ta(d)}_{ta(m)}R$, which is defined as

$$ {}^{ta(d)}_{ta(m)}R = \left({}^{tt}_{ta}R_{(d)}\right)^{-1} \cdot {}^{tt}_{ta}R_{(m)}. \tag{2.69} $$

It represents the relative difference in orientation between the *ta* frames of the exploratory and data models; by extension, it also represents the relative differences in the model parameters ${}^{tt}_{ta}E_{(m)}$ and ${}^{tt}_{ta}E_{(d)}$. The point of the above analysis is to show that these parameters

may vary widely between the exploratory and data models without affecting the ability of the exploratory model to reproduce all of the poses in the data set. The implication for the model's application is that the ${}^{tt}_{ta}E$ parameters may vary widely relative to their true value without affecting the criterion used by the optimization method to adjust the value of the model parameters — the model's fit to the subject's data. As a result, the true value of these parameters cannot be found by an optimization method which uses the 5 DoF model as it is currently specified.

The ${}^{tt}_{ta}E$ parameters define the orientation of the tibial anatomical frame, *ta*. The orientation of this frame has physiological relevance, as its Y axis is the axis of internal/external rotation (IN/EX) for the knee. Improper orientation of this axis could result in kinematic crosstalk for the joint angles at the knee. Also, the Z axis of the *ta* frame aligns with the flexion axis of the knee when IN/EX is 0°. Even if the Y axis is oriented properly, a poor definition of the Z axis would cause an offset to the knee IN/EX curve.

The 5 DoF model could potentially be used for global optimization, a technique which imposes joint constraints on a set of movement data in an attempt to reduce the effects of STA [12]. By the discussion surrounding Eqn 2.27, the definition of ${}^{tt}_{ta}R$ affects all of the model's joint angles. Even though an inaccurate or even completely non-physiological value for ${}^{tt}_{ta}R$ allows the model to fit a given data set, it will also create biases in ${}^{fi}_{pa}E_x$, ${}^{fi}_{pa}E_y$, ${}^{fi}_{pa}E_z$, ${}^{ta}_{fa}E_y$, and ${}^{ta}_{fa}E_z$. Using the 5 DoF model for global optimization would result in erroneous joint angle values unless an accurate definition of ${}^{tt}_{ta}R$ is available through other means.

Unlike the joint angles, there is nothing in the above analysis to suggest that the unidentifiability of ${}^{tt}_{ta}E_x$, ${}^{tt}_{ta}E_y$, and ${}^{tt}_{ta}E_z$ causes bias to the other model parameters. If the other model parameters are not biased by a definition of ${}^{tt}_{ta}R$ which allows the model to fit the data set, then the 5 DoF model could still be used to estimate them. Further work is needed to confirm such a possibility.

Chapter 3

A technique for estimating joint parameters at the hip and knee without thigh marker data

Ben Tesch[1,*], Brian S.R. Armstrong[1], Kristian M. O'Connor[1]

1 University of Wisconsin-Milwaukee

∗ **E-mail: Corresponding bctesch@uwm.edu**

3.1 Abstract

In this paper, a kinematic model of the hip and knee is fitted to motion data from the pelvis and lower leg segments using a nonlinear optimization routine. This allows the parameters of both joints to be estimated without reference to marker data from the thigh segment, which is prone to a high degree of Soft Tissue Artifact (STA). Ten subjects perform five trials of two movements which are designed to produce consistent joint parameter estimates. Repeatability is reasonably good; the ten subject average of the five trial joint parameter standard deviation is 3.52mm for the hip joint center location, 2.44mm for the femoral length, and 1.67mm for the knee joint center location. The model may be fitted to any movement produced by a subject once the subject's joint parameters have been estimated. When fitted to a movement, the model provides an estimate of the pose of the femur which may be used to observe STA at the thigh. This feature is demonstrated for a repeated internal and external rotation of the hip, during which the knee is hyperextended, making the lower leg segment a second observer thigh STA. Because the model fitting procedure is able to compensate for unintentional knee flexion, its estimate of STA at the thigh improves upon the estimate obtained directly from the lower leg segment. Limitations and potential applications of the technique presented in this paper are discussed.

3.2 Introduction

Properly defined Anatomical Frames (AFs) are essential for obtaining valid and repeatable kinematics and kinetics from motion capture data. AFs are commonly defined by the manual palpitation of Anatomical Landmarks (ALs), but the variability of this process can lead to poorly reconstructed kinematics [4]. Functional methods can improve upon the reliability of ALs by estimating certain joint parameters, such as the Hip Joint Center (HJC) or Knee Flexion Axis (KFA), by a mathematical procedure performed on a subject's movement data [17]. These parameters are then used in the definition of AFs. Functional methods are operator independent, but they require an additional movement, such as knee flexion, to be performed and may be biased by the effects of Soft Tissue Artifact (STA) [15]. Optimization methods also estimate joint parameters from movement data, but they do so by "fitting" a kinematic model to the data. This involves using a nonlinear optimization routine to find the values for the model's parameters which allow the model to best reproduce the movements in the data [14].

Optimization methods have an interesting property: They may fit a kinematic model spanning multiple joints to motion data from only the most proximal and distal segments in the model. For example, van den Bogert et al. [21] were able to fit an ankle model which represents the talocrural and subtalar joints as revolutes to motion data from markers on the lower leg and the shoe — the talus itself was not tracked. This work applies the same principle to the lower limb by fitting a kinematic model of the hip and knee to motion data from the pelvis and lower leg. This has the benefit of removing dependence on data from the thigh, which is generally more affected by STA than lower leg data [13]. The hip is modelled as a spherical joint, and the knee as a 2 Degree of Freedom (DoF) compound hinge; the work of Hollister et al. [8] suggests that physiological knee motion is well represented by such a joint.

Pavan et al. [12] have previously used a combined hip and knee model to remove dependence on thigh marker data, and they provide the insight that this kind of model may be used to observe STA at the thigh. Their knee model consists of a four bar linkage with varying ligament lengths, and there was some difficulty in adapting it to individual subjects.

The simpler knee model employed in this work, fitted to subject data with the optimization routine of [18], yields improvements in this area.

3.3 Materials and methods

3.3.1 Notation

Homogeneous Transforms (HTs) are convenient tools for representing the relative pose of coordinate frames. In this work, they are used to define the kinematic model and to represent motion capture data, and their notation is covered at the outset.

Given a point q and three coordinate frames a, b, and c, the 3-vector

$$ {}^{a}P_{q} = \begin{bmatrix} x \\ y \\ z \end{bmatrix} \tag{3.1} $$

represents the point q in frame a coordinates. The 4×4 matrix ${}^{b}_{a}T$ transforms ${}^{a}P_{q}$ into a b coordinate representation,

$$ \begin{bmatrix} {}^{b}P_{q} \\ 1 \end{bmatrix} = {}^{b}_{a}T \cdot \begin{bmatrix} {}^{a}P_{q} \\ 1 \end{bmatrix}, \tag{3.2} $$

provided a fourth element of value 1 is appended to the 3-vectors. For convenience, this is written

$$ {}^{b}P_{q} = {}^{b}_{a}T \cdot {}^{a}P_{q}, \tag{3.3} $$

and the addition of the fourth element is implied. ${}^{b}_{a}T$ is a Homogeneous Transform (HT) with the following structure,

$$ {}^{b}_{a}T = \begin{bmatrix} & {}^{b}_{a}R & & {}^{b}P_{\circ_a} \\ 0 & 0 & 0 & 1 \end{bmatrix}, \tag{3.4} $$

where ${}^{b}_{a}R$ is a 3×3 orthogonal rotation matrix which defines the relative orientation of the a and b frames; the relative position of these frames is given by ${}^{b}P_{\circ_a}$, which represents the

origin of frame a (written $\overset{\circ}{a}$) in frame b coordinates. HTs may be chained together,

$$ {}^{c}_{a}T = {}^{c}_{b}T \cdot {}^{b}_{a}T, \tag{3.5} $$

and inverted,

$$ {}^{a}_{b}T = {}^{b}_{a}T^{-1}. \tag{3.6} $$

A rotation matrix has nine elements but only 3 DoF; its elements are not independent from each other and are unsuitable as model parameters. Instead, the rotation matrices of the kinematic model are composed from a sequence of three elemental rotations about a defined set of axes [20]. The quantities which give the angular values of these rotations are called Cardan angles. The operator R() is defined below; it turns a Cardan angle into its associated elemental rotation,

$$ \begin{aligned} \mathrm{R}\left(E_x\right) &= \begin{bmatrix} 1 & 0 & 0 \\ 0 & C_x & S_x \\ 0 & -S_x & C_x \end{bmatrix} \\ \mathrm{R}\left(E_y\right) &= \begin{bmatrix} C_y & 0 & -S_y \\ 0 & 1 & 0 \\ S_y & 0 & C_y \end{bmatrix} \\ \mathrm{R}\left(E_z\right) &= \begin{bmatrix} C_z & S_z & 0 \\ -S_z & C_z & 0 \\ 0 & 0 & 1 \end{bmatrix}, \end{aligned} \tag{3.7} $$

where the Cardan angle E_x corresponds to an elementary rotation about the X axis, C_y stands for $\cos(E_y)$, and S_z stands for $\sin(E_z)$. The rotation matrix ${}^{b}_{a}R$ may be composed from three Cardan angles,

$$ {}^{b}_{a}R = \mathrm{R}\left({}^{b}_{a}E_y\right) \cdot \mathrm{R}\left({}^{b}_{a}E_x\right) \cdot \mathrm{R}\left({}^{b}_{a}E_z\right), \tag{3.8} $$

where the Z-X-Y sequence has been used. This corresponds to a rotation of E_z radians

about the Z axis of frame a, followed by a rotation of E_x radians about an axis mutually perpendicular to the Z axis of frame a and the Y axis of frame b, followed by a rotation of E_y radians about the Y axis of frame b. When defined in this way,

$$ {}^b_aR = \begin{bmatrix} C_zC_y - S_zS_yS_x & S_zC_y + C_zS_yS_x & -S_yC_x \\ -S_zC_x & C_zC_x & S_x \\ C_zS_y + S_zC_yS_x & S_zS_y - C_zC_yS_x & C_yC_x \end{bmatrix}, \tag{3.9} $$

where $C_z = \cos({}^b_aE_z)$, $S_y = \sin({}^b_aE_y)$, and so on; this is equivalent to the JCS 2 sequence in [3] and is used to encode joint angles. The matrix ${}^b_aR$ may be decomposed into Z-X-Y sequence Cardan angles using the relations

$$ \begin{aligned} {}^b_aE_x &= \text{asin}\left({}^b_aR(2,3)\right) \\ {}^b_aE_y &= \text{atan2}\left(-{}^b_aR(1,3),\, {}^b_aR(3,3)\right) \\ {}^b_aE_z &= \text{atan2}\left(-{}^b_aR(2,1),\, {}^b_aR(2,2)\right), \end{aligned} \tag{3.10} $$

where $\text{atan2}(\cdot,\cdot)$ is the two argument arctangent function.

The rotation and translation parts of a HT each have 3 DoF, and the 6-vector given by

$$ {}^b_aG = \begin{bmatrix} {}^b_aE \\ {}^bP^{\circ}_a \end{bmatrix} = \begin{bmatrix} {}^b_aE_x \\ {}^b_aE_y \\ {}^b_aE_z \\ {}^bP^{\circ}_a(x) \\ {}^bP^{\circ}_a(y) \\ {}^bP^{\circ}_a(z) \end{bmatrix} \tag{3.11} $$

and the HT ${}^b_aT$ both fully define the relative pose of the a and b frames.

3.3.2 Motion Capture Setup

Measurements are taken with a Moiré Phase Tracking (MPT) system by Metria Innovation (Milwaukee, WI). The MPT system is composed of a single camera with integrated light

source, a set of markers, and a computer. Engineered moiré patterns produced by each marker allow the system to measure the marker's orientation relative to the plane of the camera's sensor. This information, combined with measurements in the plane of the camera's sensor, results in a 6 DoF measurement of the marker's pose and the ability to specify a complete technical frame for each marker. This property is sketched in Figure 3.1. The MPT system has been previously validated against a standard stereophotogrammetry system in the context of human movement analysis by [22]. In this study, measurements are collected at a capture rate of 60 frames per second.

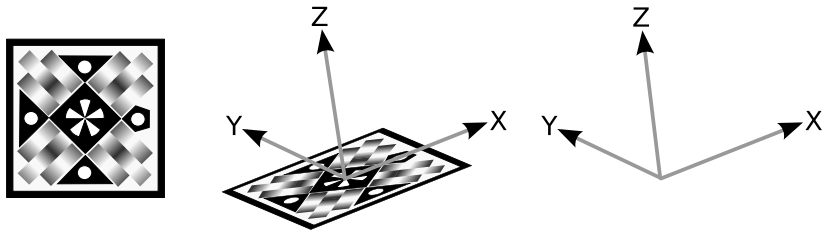

Figure 3.1: **Each marker is tracked with 6 DoF measurement and resolves to a technical frame.**

Due to the single-camera nature of the MPT system, marker placement follows a different strategy than used in a standard stereophotogrammetry setup. In particular, markers should directly face the camera when the subject is at stance; if a marker tilts too far away from the camera's line of sight during movement, its pose will not be recorded. Markers are attached with hook and loop fastener to neoprene bands worn by subject. The bands are wrapped around the pelvis, thigh, and lower leg; markers are placed on these bands over the iliac crest, at mid-thigh, and over the gastrocnemius. During the collection of pilot data, visual observations indicated that the iliac crest marker was perturbed by the gluteus medius and tensor fasciae latae during the functional movements (For which, see Section 3.3.3). To mitigate this phenomenon, another marker is placed over the sacrum. In order to allow this marker to face the camera, a thick triangular spacer is held over the subject's sacrum by the neoprene band on the pelvis. The anterior face of this spacer is padded, while small but strong magnets are embedded in its posterior face. Complementary magnets are embedded in the base of a T-shaped bracket which holds a marker over the spacer on the outside of the neoprene band. Similarly, a padded block is held over the medial surface of the tibia

by the neoprene band on the lower leg. A short arm attached to the proximal surface of this block holds a marker anterior to the subject's leg so that it can be seen by the camera; this marker should be less affected by STA than the marker over the gastrocnemius. Marker placement is shown in Figure 3.2.

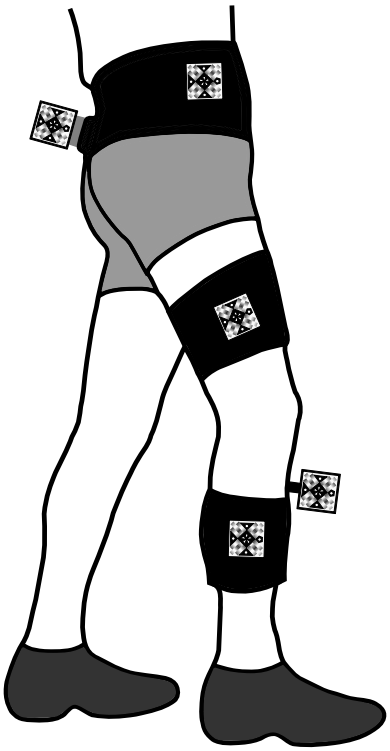

Figure 3.2: **Markers placed on subject with the aid of neoprene bands, padded blocks, and hook and loop fasteners.**

For each frame of motion capture data, the MPT system records the pose of each marker in the coordinate frame of the camera with the following HTs,

$$ {}^{cam}_{pt}\overline{T}_i,\ {}^{cam}_{ft}\overline{T}_i,\ {}^{cam}_{tt}\overline{T}_i, \tag{3.12} $$

where the bar over each HT marks it as a measured quantity. *pt*, *ft*, and *tt* are abbreviations for the pelvic, femoral, and tibial technical frames, respectively. These coordinate frames correspond in pose to the markers on the pelvis, thigh, and lower leg. ${}^{cam}_{ft}\overline{T}$ will find application in investigating thigh STA. The data set to which the model is fitted contains

the relative pose of the pt and tt frames

$$ {}^{tt}_{pt}\overline{T}_i = {}^{cam}_{tt}\overline{T}_i^{-1} \cdot {}^{cam}_{pt}\overline{T}_i, \tag{3.13} $$

for $i = 1, 2, \ldots, n_{df}$, where i is the data frame index, and n_{df} is the total number of data frames.

Several Anatomical Landmarks are collected. At the pelvis are the left and right anterior superior iliac spine landmakrs, as well as the left and right posterior superior iliac spine landmarks. These are used to orient the pelvic anatomical frame. The medial and lateral femoral condyle landmarks are collected in the coordinates of the tt frame,

$$ {}^{tt}P_{MFC},\ {}^{tt}P_{LFC}, \tag{3.14} $$

while the subject stands with the knee in full extension. The medial and lateral malleoli are also collected; they are given by the quantities

$$ {}^{tt}P_{MMA}\ and\ {}^{tt}P_{LMA}. \tag{3.15} $$

Data was collected on ten subjects, all of whom gave informed consent. This study also received approval from the IRB of the University of Wisconsin–Milwaukee.

3.3.3 Functional Movements

Each subject performs two functional movements which are concatenated to form the data set used for model fitting. The first of these is the Star Arc movement, which is designed to locate the HJC [1]. The "star" portion of the movement has seven lobes; for each lobe, the hip is exercised so that the lower limb moves away from and returns to the anatomical position in a particular plane. One of the planes is produced by pure flexion of the hip, a second by abduction, and a third by extension. The other four planes are evenly spaced between these three. The "arc" portion of the movement starts at the anatomical position, followed by hip flexion, circumduction, and hip extension to end at the anatomical position; this causes the foot to trace out a D shape over the floor. The knee is held in an extended

position throughout both parts, which total 800 frames of data. The second functional movement is a cyclical repetition of combined hip and knee flexion followed by combined hip and knee extension. Its execution resembles operating an imaginary bicycle pedal with one leg while standing on the other. This movement is collected in 700 frames of data; its purpose is to produce a reasonable range of knee flexion while simultaneously exercising the hip. In pilot data, it did a better job of constraining the estimated femur length than knee flexion with a stationary hip joint. Both functional movements are repeated five times per subject to gauge the repeatability of the estimated joint parameters.

3.3.4 Model Definition

The kinematic model of the hip and knee is defined mathematically by a series of Homogeneous Transforms (HTs) between named coordinate frames. These HTs, in turn, are constructed from three kinds of scalar quantities: *model parameters*, *constants*, and *joint angles*. The joint angles are Cardan angles which encode the degrees of freedom of the model's spherical and compound hinge joints; they may take on a different value in each frame of motion capture data. The model parameters hold the same value throughout all data frames and represent quantities which are considered not to change during movement, such as the length of the femur or the position of the Hip Joint Center (HJC) in the pelvis. Constants are fixed values which are not adjusted by the optimization routine, unlike the model parameters and joint angles.

The model's reference frames are shown in Figure 3.3. When the subject is standing in the anatomical position, the Y axis of each reference frame points in the superior direction, the Z axis points to the right, and the X axis points in the anterior direction. For the atatomical frames of the knee joint (*fa* and *ta* in the figure), this is only approximate, as their Z axes are aligned to the flexion axis of the knee.

The pelvic and tibial technical frames, abbreviated *pt* and *tt*, correspond in pose to the technical frames of the pelvic and lower leg markers. The orientation of the pelvic anatomical frame (*pa*) is parameterized by the three quantities in ${}^{pa}_{pt}E$. These are constants, set from the Anatomical Landmarks (ALs) at the pelvis according to [23]. The origin of the *pa* frame

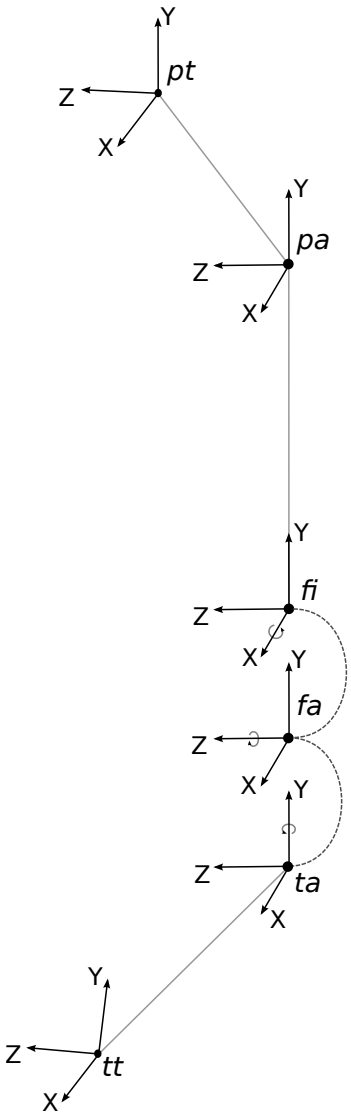

Figure 3.3: **Reference frames and links of kinematic model in exploded view.**

(denoted $\overset{\circ}{pa}$) is placed at the HJC; it is defined by the three model parameters in ${}^{pa}P_{\underset{pt}{\circ}}$.

The femoral intermediate frame, *fi*, has its origin at the Knee Joint Center (KJC). The HJC is constrained to lie along the Y axis of the *fi* frame; this is accomplished by making ${}^{fi}P_{\underset{pa}{\circ}}(y)$ a model parameter and setting ${}^{fi}P_{\underset{pa}{\circ}}(x)$ and ${}^{fi}P_{\underset{pa}{\circ}}(z)$ to zero. The rotation ${}^{fi}_{pa}R$ traverses the spherical joint and is composed from the Cardan angles in ${}^{fi}_{pa}E$ according to the Z-X-Y sequence (See Eqn 3.8), as recommended by [23]. ${}^{fi}_{pa}E_z$ corresponds to hip flexion/extension (FL/EX), ${}^{fi}_{pa}E_x$ corresponds to adduction/abduction (AD/AB), and ${}^{fi}_{pa}E_y$ corresponds to internal/external rotation (IN/EX).

The Z axis of the femoral anatomical frame (fa) corresponds to the Knee Flexion Axis (KFA). Since the Y axis of fi points from the KJC to the HJC, ${}^{fa}_{fi}R$ is defined as an elementary rotation about the X axis of fi,

$$ {}^{fa}_{fi}R = \mathrm{R}({}^{fa}_{fi}E_x), \tag{3.16} $$

in order to allow the KFA to have a non-orthogonal orientation relative to Y axis of fi. This quantity is expected to have a small value [16] and will provide an indication of the model's physiological consistency. The translation ${}^{fa}P_{\underset{fi}{\circ}}$ is set to the zero vector, $\mathbf{0}$, placing the origin of the fa frame at the KJC.

The Y axis of the tibial anatomical frame (ta) corresponds to the Knee axis of Longitudinal Rotation (KLR). The KLR and KFA are the body fixed axes recommended for the knee joint coordinate system in [6]. Creating ${}^{ta}_{fa}R$ from the Cardan angles in ${}^{ta}_{fa}E$ by the Z-X-Y sequence (See Eqn 3.8) causes ${}^{ta}_{fa}E_z$ to correspond to FL/EX occurring about the KFA and ${}^{ta}_{fa}E_y$ to correspond to IN/EX occurring about the KLR. These two pair variables constitute the 2 DoF of the compound hinge knee joint. ${}^{ta}_{fa}E_x$ is set to 0, making the KFA and KLR perpendicular to each other. Furthermore, ${}^{ta}P_{\underset{fa}{\circ}}$ is set to $\mathbf{0}$, placing the origin of ta at the KJC and causing the KLR and KFA to intersect.

The origin of the ta frame, coincident with the KJC, is given in tt coordinates by the three model parameters in ${}^{tt}P_{\underset{ta}{\circ}}$. The orientation of the ta frame is defined by the three quantities in ${}^{tt}_{ta}E$. Due to mathematical properties of the model, which are presented in [19], these quantities may take on a wide range of values without affecting the fit of the kinematic model to a subject's movement data. Consequently, they cannot be reasonably estimated using an optimization routine and are defined by the following procedure.

${}^{tt}_{ta}R$ is constructed according to the Y-X-Z sequence,

$$ {}^{tt}_{ta}R = \mathrm{R}\left({}^{tt}_{ta}E_z\right) \cdot \mathrm{R}\left({}^{tt}_{ta}E_x\right) \cdot \mathrm{R}\left({}^{tt}_{ta}E_y\right), \tag{3.17} $$

and takes on the form

$$ {}^{tt}_{ta}R = \begin{bmatrix} C_zC_y + S_zS_xS_y & S_zC_x & -C_zS_y + S_zS_xC_y \\ -S_zC_y + C_zS_xS_y & C_zC_x & S_zS_y + C_zS_xC_y \\ C_xS_y & -S_x & C_xC_y \end{bmatrix}, \tag{3.18} $$

where $C_z = \cos\left({}^{tt}_{ta}E_z\right)$, $S_x = \cos\left({}^{tt}_{ta}E_x\right)$, and so on. The second column of this matrix, which gives the Y axis of the ta frame in tt coordinates (call it ${}^{tt}\widehat{V}_{KLR}$), only depends on two Cardan angles: ${}^{tt}_{ta}E_x$ and ${}^{tt}_{ta}E_z$. ${}^{tt}\widehat{V}_{KLR}$ is defined by the unit vector pointing from the Ankle Joint Center (AJC) to the KJC,

$$ {}^{tt}\widehat{V}_{KLR} = \frac{{}^{tt}P_{\underset{ta}{\circ}} - {}^{tt}P_{AJC}}{\|{}^{tt}P_{\underset{ta}{\circ}} - {}^{tt}P_{AJC}\|}, \tag{3.19} $$

where the AJC is given by the malleolar midpoint,

$$ {}^{tt}P_{AJC} = \frac{1}{2}\left({}^{tt}P_{MMA} + {}^{tt}P_{LMA}\right), \tag{3.20} $$

and the KJC is given by the model parameters in ${}^{tt}P_{\underset{ta}{\circ}}$. ${}^{tt}_{ta}E_x$ and ${}^{tt}_{ta}E_z$ are derived from ${}^{tt}\widehat{V}_{KLR}$ with the relations

$$ \begin{aligned} {}^{tt}_{ta}E_x &= \operatorname{asin}\left(-{}^{tt}\widehat{V}_{KLR}(z)\right) \\ {}^{tt}_{ta}E_z &= \operatorname{atan2}\left({}^{tt}\widehat{V}_{KLR}(x),\ {}^{tt}\widehat{V}_{KLR}(y)\right), \end{aligned} \tag{3.21} $$

and definition of ${}^{tt}_{ta}E_y$ is covered in Section 3.3.5.

For each frame of motion capture data, the model equation,

$$ {}^{tt}_{pt}\widehat{T}_i = {}^{tt}_{ta}T \cdot {}^{ta}_{fa}T_i \cdot {}^{fa}_{fi}T \cdot {}^{fi}_{pa}T_i \cdot {}^{pa}_{pt}T, \tag{3.22} $$

produces the model's estimate of the relative pose of the pt and tt frames. The hat distinguishes this estimated quantity from the analogous measured quantity ${}^{tt}_{pt}\overline{T}_i$. Notice that only the transforms formed from pair variables have a subscript data frame index, as the other transforms do not vary with movement.

3.3.5 Optimization Routine

The two-level optimization method of [18] is used to find the model parameter and joint angle values which best fit the subject's data. The inner level of this method operates on each data frame individually and finds the joint angle values which minimize that frame's residual,

$$SSQ_i = \|{}^{tt}_{pt}\widetilde{G}_i\|^2, \tag{3.23}$$

which is the sum of squares of that frame's residual vector,

$${}^{tt}_{pt}\widetilde{G}_i = {}^{tt}_{pt}\widehat{G}_i - {}^{tt}_{pt}\overline{G}_i. \tag{3.24}$$

Here, the relative pose of the *pt* and *tt* frames given by the model ($^{tt}_{pt}\widehat{T}_i$) and the data ($^{tt}_{pt}\overline{T}_i$), have been decomposed into the 6-vectors $^{tt}_{pt}\widehat{G}_i$ and $^{tt}_{pt}\overline{G}_i$ — See Eqn 3.11. The outer level of the optimization routine searches for the model parameter values which minimize the overall residual,

$$SSQ = \sum_{i}^{n_{df}} SSQ_i, \tag{3.25}$$

which is the sum of squares of the overall residual vector,

$$\begin{bmatrix} {}^{tt}_{pt}\widetilde{G}_1 \\ {}^{tt}_{pt}\widetilde{G}_2 \\ \vdots \\ {}^{tt}_{pt}\widetilde{G}_{n_{df}} \end{bmatrix}. \tag{3.26}$$

The model parameter values resulting from this search are taken as estimates of the subject's joint parameters.

As knee flexion, modelled by the joint angle $^{ta}_{fa}E_z$, approaches 0°, hip and knee IN/EX, modelled by $^{fi}_{pa}E_y$ and $^{ta}_{fa}E_y$, have an increasingly similar effect on $^{tt}_{pt}\widehat{T}$. To avoid unidentifiability in these parameters, $^{ta}_{fa}E_y$ is set to 0 when flexion is less than 15°, which occurs when $^{ta}_{fa}E_z > -15°$. This constraint does not seem unreasonable for unloaded, open chain movements, as this sort of rotation is more likely to come from the hip at low knee flexion. When

this constraint is active, it forces the model's knee joint to act as a plain revolute, which provides enough constraint on the value of ${}^{tt}_{ta}E_y$ to enable its estimation by the optimization routine. ${}^{tt}_{ta}E_y$ is included as a model parameter.

Since the primary movement of the knee is flexion, the position of the KJC along the KFA is poorly constrained by movement data. To compensate for this, a penalty function, *pen*, is appended to the overall residual vector. It is given by the equation

$$pen = {}^{ta}P_{MFC}(z) + {}^{ta}P_{LFC}(z), \tag{3.27}$$

which constrains the KJC to lie in between the projections of the medial and lateral femoral epicondyles onto the Z axis of the *ta* frame. The MFC and LFC ALs are collected when the subject is standing with the leg extended, in which condition knee IN/EX is set to zero and the Z axis of *ta* aligns with the Z axis of *fa* — the KFA. A similar constraint is found in [9]. The penalty function acts as a constraint by raising the overall residual when this condition is not met, and it is given a weight, or multiplying factor, of 50 relative to the other residual components.

Initial estimates of the model parameters are derived from the anatomical landmarks, with the initial HJC location given by the regression equations of [7]. Initial joint angle estimates are derived from the subject's data in the usual way, with the *pa* and *ta* frames defined by the initial model parameter estimates and a thigh anatomical frame defined in *ft* coordinates according to [2]. Knee IN/EX (${}^{ta}_{fa}E_y$) and AD/AB (${}^{ta}_{fa}E_x$) are initially set to zero in all frames.

3.4 Results and Discussion

3.4.1 Repeatibility of Joint Parameter Estimates

Each subject performs five *trials*, where a trial is the execution of both functional movements involved in model fitting. The optimization routine is run on every trial, producing five estimates of each joint parameter per subject. The standard deviations of these estimates are shown in Table 3.1 for each subject.

Subject			HJC	FMR	${}^{fa}_{fi}\mathbf{E_x}$	KJC	${}^{tt}_{ta}\mathbf{E_y}$
ID	(cm)	(kg)	(mm)	(mm)	(°)	(mm)	(°)
S1	165	64	(3.51)	(3.72)	-4.87 (0.41)	(3.18)	(1.36)
S2	178	82	(4.42)	(3.62)	-1.22 (0.20)	(2.49)	(0.88)
S2b	”	”	(1.92)	(1.79)	-2.43 (0.14)	(1.29)	(1.33)
S3	168	64	(2.45)	(0.91)	-3.18 (0.38)	(1.64)	(0.41)
S4	163	57	(2.57)	(0.90)	-0.30 (0.20)	(1.43)	(1.31)
S5	175	79	(1.97)	(1.50)	-1.95 (0.17)	(0.76)	(0.53)
S6	180	84	(3.28)	(2.76)	0.25 (0.22)	(1.14)	(0.59)
S7	178	68	(3.51)	(3.42)	-3.20 (0.11)	(0.71)	(0.49)
S8	180	77	(4.33)	(3.04)	-1.27 (0.50)	(0.63)	(1.90)
S9	191	95	(3.95)	(2.45)	-1.36 (0.36)	(2.51)	(1.44)
S10	198	114	(6.81)	(2.73)	-6.96 (0.57)	(2.55)	(1.11)

Table 3.1: **Subject information, mean value of ${}^{fa}_{fi}E_x$, and standard deviation in () for all model parameters.** FMR is femur length — ${}^{fi}_{pa}P_{\circ}(y)$. KJC (${}^{tt}_{ta}P_{\circ}$) and HJC (${}^{pa}_{pt}P_{\circ}$) standard deviations are 3-D.

Subjects 1 and 4 are female; the rest are male. Two collections were performed on subject 2, due to a concern about data quality in the first collection. The second collection yielded more consistent results. HJC location has a particularly high variance for subject 10, probably due to the high degree of soft tissue coverage at the pelvis for this subject. Further, the iliac crest marker was used for subject 10, as the sacral marker seemed to be perturbed by the gluteus maximus during movement. The iliac crest marker was also used for subject 9, as it appeared to track the pelvis well, owing to this subject's stature and low soft tissue coverage under the marker. The sacral marker was used for all other subjects. The block-mounted lower leg marker was used for every subject.

The joint parameter estimates are reasonably consistent overall. The HJC shows the largest variation among the parameters, and this is decomposed into directional components in Figure 3.4. Variation is highest in the Superior/Inferior (S/I) direction. The single outlier in the R/L direction comes from subject 10.

${}^{fa}_{fi}E_x$ quantifies the degree to which the optimal KFA deviates from orthogonality with respect to the vector pointing from the KJC to the HJC; it is expected to have a small value [16]. It is not surprising that this quantity has the highest magnitude for subject 10. A large magnitude is also recorded for this quantity in the case of Subject 1, along with the highest variation in femur length and KJC location and the highest overall residual. These factors

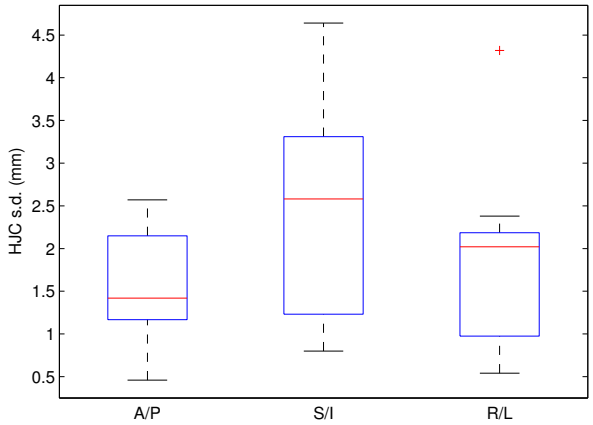

Figure 3.4: **Box plot of HJC standard deviation in the Anterior/Posterior, Superior/Inferior, and Right/Left directions.**

Subject		50^{th}	75^{th}	90^{th}	95^{th}	99^{th}	RMS
S6	(mm)	0.68	1.23	2.24	3.02	4.64	1.42
	(°)	0.0067	0.015	0.029	0.041	0.064	0.019
S4	(mm)	1.31	2.52	4.00	4.91	7.13	2.37
	(°)	0.013	0.029	0.051	0.065	0.098	0.03
S1	(mm)	1.83	3.32	5.26	6.73	12.69	3.48
	(°)	0.016	0.037	0.070	0.090	0.18	0.045

Table 3.2: **Percentiles and RMS of position and orientation residuals for three subjects.** S1 and S6 have the highest and lowest overall residuals; S4 is close to the average.

indicate poor data quality, most likely due to STA at the pelvis. The other subjects have reasonable values for ${}^{fa}_{fi}E_x$ and lower residuals than subjects 1 and 10. Percentiles and RMS for the position and orientation residuals of three subjects are shown in Table 3.2. Subject 1 represents a high residual, subject 6 a low residual, and subject 4 an average residual. In general, the model fits the data well.

3.4.2 Investigating Thigh STA

The functional movements of Section 3.3.3 are designed to exercise the hip and knee in such a way that the model parameters are well constrained by the movement data; not all movements are suitable for this task. That said, once the model parameters have been estimated for a given subject, the model may be fitted to any movement the subject performs if only the joint angles are adjusted in the fitting procedure. Conceptually, this is a form

of global optimization [10]; it is carried out by running the inner loop of the optimization routine on the new target movement. Once fitted to a given movement, the *fa* and *fi* frames of the model serve as observers of thigh STA through the transform

$$ {}^{fi}_{ft}\widehat{T}_i = {}^{fi}_{pa}T_i \cdot {}^{pa}_{pt}T \cdot {}^{pt}_{cam}\overline{T}_i \cdot {}^{cam}_{ft}\overline{T}_i \tag{3.28} $$

or

$$ {}^{fa}_{ft}\widehat{T}_i = {}^{fa}_{fi}T \cdot {}^{fi}_{ft}\widehat{T}_i. \tag{3.29} $$

In order to test this application of the model, an additional movement is performed consisting of repeated internal and external rotation of the hip with the knee hyper-extended. This movement demonstrates a particular form of thigh STA: The thigh marker is known to follow the rotation of the femur only poorly [5]. Further, because the knee is hyper-extended, thigh STA may also be observed directly from the lower leg segment through the transform

$$ {}^{ta}_{ft}T_i = {}^{ta}_{tt}T \cdot {}^{tt}_{cam}\overline{T}_i \cdot {}^{cam}_{ft}\overline{T}_i, \tag{3.30} $$

providing a basis of comparison for the model estimate of thigh STA.

If ${}^{fi}_{ft}\widehat{T}_i$ is decomposed into ${}^{fi}_{ft}\widehat{G}_i$ using the Z-X-Y Cardan sequence, the rotation ${}^{fi}_{ft}\widehat{E}_y$ will occur about the Y axis of the *fi* frame, which points from the KJC to the HJC. This quantity is ideal for observing the anticipated mechanism of thigh STA; it is plotted in Figure 3.5 alongside ${}^{fi}_{pa}E_y$ (hip IN/EX) for the hip rotation movement performed by Subject 3.

The thigh marker fails to follow the rotation of the femur by a surprising amount, and this phenomenon is correlated to hip IN/EX, as expected. Surprisingly, the correlation coefficient ($r = 0.997$) is quite high. When observed without model fitting through ${}^{ta}_{ft}E_y$, the pattern is almost identical and shows a similar correlation to hip IN/EX ($r = 0.980$). The Cardan sequence which creates ${}^{ta}_{ft}E_y$ helps compensate for some of the involuntary knee flexion that would otherwise muddle the observation obtained directly from the data. No such compensation is present in the translation component ${}^{ta}P_{\underset{ft}{\circ}}(x)$, which, like its counterpart in the model, ${}^{fi}\widehat{P}_{\underset{ft}{\circ}}(x)$, is also affected by the poor tracking of the thigh marker. Figures 3.6 and 3.7 show plots of these quantities alongside hip IN/EX. The correlation

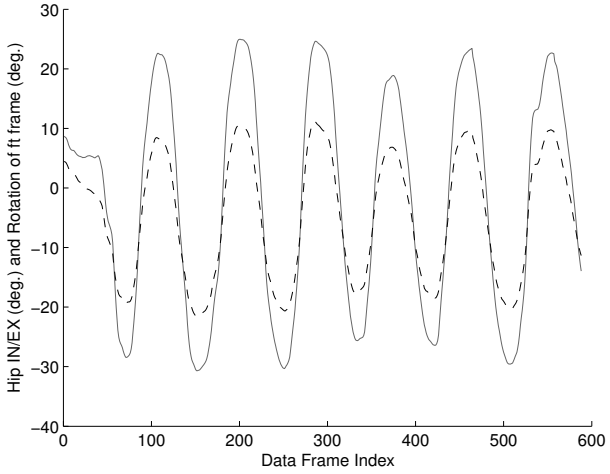

Figure 3.5: **Plot of ${}^{fi}_{ft}\widehat{E}_y\,(^\circ)$ (black dashes) and ${}^{fi}_{pa}E_y\,(^\circ)$ (gray line) vs. data frame index during hip rotation.**

is evident in both figures, but it is cleanest in Figure 3.7, as the model fitting procedure compensates for unintentional knee flexion.

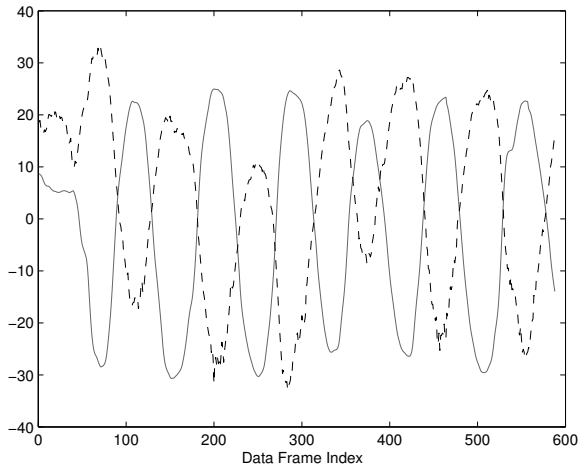

Figure 3.6: **Plot of ${}^{ta}_{\circ}P_{ft}(x)\,(mm)$ (black dashes) and ${}^{fi}_{pa}E_x(^\circ)$ (gray line) vs. data frame index during hip rotation.** $r = -0.856$.

3.5 Limitations and Applications

A major weakness of functional and optimization methods is their susceptibility to bias when STA is present. This is the motivation for removing dependence on thigh marker data

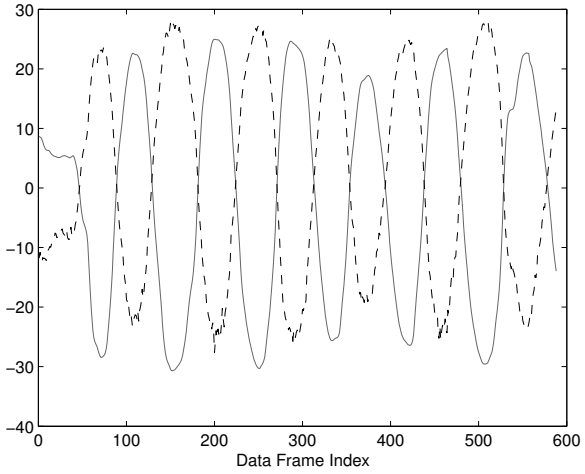

Figure 3.7: **Plot of ${}^{fi}\widehat{P}_{\underset{ft}{\circ}}(x)\ (mm)$ (black dashes) and ${}^{fi}_{pa}E_x(^\circ)$ (gray line) vs. data frame index during hip rotation.** $r = -0.996$.

through model fitting. That said, pelvic STA is still a concern and is thought to be the main source of measurement error affecting the optimization method presented here. The mounting of the pelvic marker over the sacrum is an attempt to minimize STA due to muscle firing, but skin sliding is still possible, especially if the neoprene band is perturbed during the functional movements. Other mounting strategies for the pelvic marker may help to reduce potential sources of error.

Error may also arise from incomplete correspondence of the kinematic model to the true motion of the human hip and knee. The knee model of this work is based on that of Hollister et al. [8], who found knee motion to be well represented by a compound hinge knee joint allowing FL/EX and IN/EX. Their model has two properties lacking in this work's model: The Knee axis of Longitudinal Rotation (KLR) is placed anterior to the Knee Flexion Axis (KFA) and allowed to take a non-orthogonal orientation with repsect to the KFA. A separate kinematic model was created with two additional parameters enabling such placement of the KLR, but the estimation of these parameters from motion data resulted in inconsistent and non-physiological results, as well as poor conditioning of the optimization routine. Forcing the KLR and KFA to be perpendicular is not too large of a simplification; Hollister, et al. measured the angle between these axes to vary from 87° to 90° across 6 specimens, with an average of 88°. The effect of removing the anterior placement of the KLR is unknown.

When the pair variable ${}^{ta}_{fa}E_y$ is unconstrained, the model parameters which define the orientation of the *ta* frame (${}^{tt}_{ta}E$) may take on many different values without affecting the fit of the model to the data set [19]. This phenomenon has two related consequences. First, different orientations of the *ta* frame will produce different joint angle profiles for the same data set, and this also affects the pose of the *fa* frame. Second, the parameters which orient the *ta* frame cannot be estimated through optimization. As a result, non-physiological joint angle values and inaccurate *fa* frame poses cannot be ruled out. This limits the general applicability of the kinematic model to global optimization and thigh STA investigation.

When knee flexion is below 15°, ${}^{ta}_{fa}E_y$ is set to 0, forcing the knee model to act as a plain revolute joint (See Section 3.3.5). In this condition, the caveats of the previous paragraph do not apply. The model seems useful for investigating thigh STA in movements with low knee flexion, such as the one in Section 3.4.2. This kind of movement plays an important role in the dynamic calibration method of [11]. In this method, the subject is asked to mimic the hip motion which occurs during walking while keeping the knee hyperextended; this is called the Artefact Assessment Movement (AAM). During the AAM, thigh STA is measured in a coordinate frame embedded in the lower leg, and a table is created which indexes corrections to thigh STA by the joint angles at the hip. When the subject performs a gait trial, the hip joint angles are measured and the corrections to thigh STA are found in the table and applied. The results look promising. The technique presented this work could potentially benefit the measurement of thigh STA during the AAM of the dynamic calibration method by compensating for involuntary movements of the knee.

Acknowledgements

Thanks to Lauren Benson and T. Gus Almonroeder for their generous assistance with data collection and their sharing of expertise.

Chapter 4

A one-level optimization method for the estimation of joint parameters

Ben Tesch[1,*], Brian S.R. Armstrong[1]

1 University of Wisconsin-Milwaukee

∗ **E-mail: Corresponding bctesch@uwm.edu**

4.1 Abstract

This paper presents an optimization method which may be used to estimate the parameters of anatomical joints by fitting a kinematic model to movement data. It departs from the two-level optimization method of Sommer and Miller by estimating all of the model's parameter and joint angle values with a single-level nonlinear optimization routine. This allows the one-level method to calculate parameter estimates showing good agreement with those of the two-level method at significantly reduced computational cost; a speedup of about 30× has been observed. Details of both methods are presented, along with numerical results from a motion capture study.

4.2 Introduction

This paper presents a modification to the two-level optimization method of Sommer and Miller [6]. Optimization methods form a category of joint parameter estimation techniques which operate by fitting a kinematic model to movement data. In this process, the parameters and joint angles of a kinematic model are adjusted by a nonlinear optimization routine to find the values which allow the model to best reproduce, or fit, a subject's movement data [4]. These methods require that the relative pose of the most proximal and distal body

segments included in the model is measured with 6 Degrees of Freedom (DoF), and that the model has 5 or fewer DoF; the model may span multiple joints. Taking advantage of these properties, the authors of this work have fitted a kinematic model containing a spherical hip joint and a 2 DoF compound hinge knee joint to movement data from the pelvis and lower leg segments [7]. This allows estimation of the joint parameters of the hip and knee without recourse to thigh segment data, which is strongly affected by soft tissue artifact [3]. In the context of fitting that model to movement data, a modification to the two-level optimization method was developed; it is called the one-level optimization method. Both the one and two level methods are elucidated and compared to each other in this work, with details and numerical results coming from the combined hip and knee model.

4.3 Methods

The kinematic model is defined by three kinds of scalar quantities: model parameters, joint angles (or pair variables), and constants. Constants are fixed values set a priori and not adjusted during optimization. Model parameters are adjusted by the optimization routine but retain the same value in every frame of movement data. Joint angles are also adjusted and may take on a different value for each frame of movement data. A frame of movement data, for our purposes here, consists of a single measurement of the relative pose of the segments under study at a discrete instant in time; it is given by the 6-vector

$$\overline{\boldsymbol{y}}_f = \begin{bmatrix} \overline{\boldsymbol{y}}_{f,1} \\ \overline{\boldsymbol{y}}_{f,2} \\ \overline{\boldsymbol{y}}_{f,3} \\ \overline{\boldsymbol{y}}_{f,4} \\ \overline{\boldsymbol{y}}_{f,5} \\ \overline{\boldsymbol{y}}_{f,6} \end{bmatrix} = \begin{bmatrix} {}^{\mathrm{tt}}_{\mathrm{pt}}E_{\mathrm{x}} \\ {}^{\mathrm{tt}}_{\mathrm{pt}}E_{\mathrm{y}} \\ {}^{\mathrm{tt}}_{\mathrm{pt}}E_{\mathrm{z}} \\ {}^{\mathrm{tt}}P^{\circ}_{\mathrm{pt}}(x) \\ {}^{\mathrm{tt}}P^{\circ}_{\mathrm{pt}}(y) \\ {}^{\mathrm{tt}}P^{\circ}_{\mathrm{pt}}(z) \end{bmatrix}. \tag{4.1}$$

Here, $\overline{\boldsymbol{y}}$ is the data vector, and f is the data frame index; $f = 1, 2, \ldots, n_{df}$, where n_{df} is the number of data frames. The labels tt and pt correspond to the tibial technical frame and pelvic technical frame, respectively; these are coordinate frames which give the pose of

their respective segments as measured by the motion capture system during data collection. ${}^{\mathrm{tt}}_{\mathrm{pt}}E_{\mathrm{x}}$, ${}^{\mathrm{tt}}_{\mathrm{pt}}E_{\mathrm{y}}$, and ${}^{\mathrm{tt}}_{\mathrm{pt}}E_{\mathrm{z}}$ are Cardan angles [8] which encode the relative orientation of the pt and tt frames. ${}^{\mathrm{tt}}P_{\circ}_{\mathrm{pt}}$ is a three element translation vector which gives the origin of the pt frame in the coordinates of the tt frame; its X, Y, and Z components appear in equation (4.1).

The model parameters and constants are placed in the vectors $\boldsymbol{p}$ and $\boldsymbol{q}$, respectively. These values are a mix of Cardan angles and translation vector components which define properties not expected to change during movement, such as the length of the femur, or the orientation of the pelvic bone in the pt frame. The joint angles are all Cardan angles; they parameterize the degrees of freedom of the model's joints. They are placed in the vector $\boldsymbol{a}$, which is indexed similarly to $\overline{\boldsymbol{y}}$, except it has 5 joint angles per data frame — three for the hip and two for the knee. The model function,

$$\widehat{\boldsymbol{y}}_f = m(\boldsymbol{q}, \boldsymbol{p}, \boldsymbol{a}_f), \tag{4.2}$$

yields a 6-vector which gives the relative pose of the model's pt and tt frames as defined by the model parameters, the constants, and the joint angles of data frame f. Both optimization routines adjust $\boldsymbol{a}$ and $\boldsymbol{p}$ to minimize the sum of squares of the residual vector,

$$\widetilde{\boldsymbol{y}} = \widehat{\boldsymbol{y}} - \overline{\boldsymbol{y}}, \tag{4.3}$$

where

$$\overline{\boldsymbol{y}} = \begin{bmatrix} \overline{\boldsymbol{y}}_1 \\ \overline{\boldsymbol{y}}_2 \\ \vdots \\ \overline{\boldsymbol{y}}_{n_{df}} \end{bmatrix}, \tag{4.4}$$

and a similar definition applies to $\widetilde{\boldsymbol{y}}$, $\widehat{\boldsymbol{y}}$, and $\boldsymbol{a}$.

4.3.1 Two-Level Optimization Method

The outer level of the two-level optimization method uses a Levenberg–Marquardt (L–M) algorithm with update step

$$\begin{aligned} \min_{\boldsymbol{s}} \left\| \begin{bmatrix} \widetilde{\boldsymbol{y}}^{\bullet} \\ \mathbf{0} \end{bmatrix} + \begin{bmatrix} \mathbf{J}_{2o} \\ \sqrt{\lambda}\mathbf{I} \end{bmatrix} \boldsymbol{s} \right\|^2 \\ \left\{ \boldsymbol{p} \right\}_{k+1} = \boldsymbol{s} + \left\{ \boldsymbol{p} \right\}_{k}, \end{aligned} \tag{4.5}$$

where where $\mathbf{J}_{2o}$ is the Jacobian, λ is the L–M damping paramter, $\mathbf{I}$ is the identity matrix, $\boldsymbol{s}$ is calculated using the QR factorization, and k is an iteration index. For this particular form of update step, see [5, p. 624]. The residual vector is given as

$$\widetilde{\boldsymbol{y}}^{\bullet} = \widehat{\boldsymbol{y}}^{\bullet} - \overline{\boldsymbol{y}}, \tag{4.6}$$

where the superscript bullet on $\widehat{\boldsymbol{y}}^{\bullet}$ indicates that it is calculated by the inner level of the two-level optimization method. $\mathbf{J}_{2o}$ is given by

$$\mathbf{J}_{2o} = \begin{bmatrix} \frac{\partial \widehat{\boldsymbol{y}}^{\bullet}_{1,1}}{\partial \boldsymbol{p}_1} & \cdots & \frac{\partial \widehat{\boldsymbol{y}}^{\bullet}_{1,1}}{\partial \boldsymbol{p}_8} \\ \vdots & \vdots & \vdots \\ \frac{\partial \widehat{\boldsymbol{y}}^{\bullet}_{n_{df},6}}{\partial \boldsymbol{p}_1} & \cdots & \frac{\partial \widehat{\boldsymbol{y}}^{\bullet}_{n_{df},6}}{\partial \boldsymbol{p}_8} \end{bmatrix}; \tag{4.7}$$

it is a $(6 \cdot n_{df}) \times 8$ matrix. Derivatives of $\widehat{\boldsymbol{y}}^{\bullet}$ and derivatives of the residual vector are equivalent, since $\overline{\boldsymbol{y}}$ is constant — See equation (4.6).

The inner level of the two-level method is used to calculate $\widehat{\boldsymbol{y}}^{\bullet}$. It operates one data frame at a time, solving for the joint angles which minimize the framewise residual,

$$\|\widetilde{\boldsymbol{y}}_f\|^2, \tag{4.8}$$

by an L–M routine with update step

$$\begin{aligned} \min_{\boldsymbol{s}} \left\| \begin{bmatrix} \widetilde{\boldsymbol{y}}_f \\ \mathbf{0} \end{bmatrix} + \begin{bmatrix} \mathbf{J}_{2\mathrm{i}} \\ \sqrt{\lambda}\mathbf{I} \end{bmatrix} \boldsymbol{s} \right\|^2 \\ \left\{ \boldsymbol{a}_f \right\}_{k+1} = \boldsymbol{s} + \left\{ \boldsymbol{a}_f \right\}_k , \end{aligned} \tag{4.9}$$

where $\mathbf{J}_{2\mathrm{i}}$, a 6×5 matrix, is given by

$$\mathbf{J}_{2\mathrm{i}} = \begin{bmatrix} \frac{\partial \widehat{\boldsymbol{y}}_{f,1}}{\partial \boldsymbol{a}_{f,1}} & \cdots & \frac{\partial \widehat{\boldsymbol{y}}_{f,1}}{\partial \boldsymbol{a}_{f,5}} \\ \vdots & \ddots & \vdots \\ \frac{\partial \widehat{\boldsymbol{y}}_{f,6}}{\partial \boldsymbol{a}_{f,1}} & \cdots & \frac{\partial \widehat{\boldsymbol{y}}_{f,6}}{\partial \boldsymbol{a}_{f,5}} \end{bmatrix} . \tag{4.10}$$

Once the inner level converges to the optimal joint angle values, $\boldsymbol{a}_f^{\bullet}$, the equation

$$\widehat{\boldsymbol{y}}_f^{\bullet} = m(\boldsymbol{q}, \boldsymbol{p}, \boldsymbol{a}_f^{\bullet}) \tag{4.11}$$

yields $\widehat{\boldsymbol{y}}_f^{\bullet}$. Each iteration of the inner level requires the calculation of $\mathbf{J}_{2\mathrm{i}}$, where analytical derivatives are assumed, the solution of an 11×5 system of linear equations, and one each of a model function evaluation and 6-vector subtraction to calculate the updated value of $\widetilde{\boldsymbol{y}}_f$. Since $\boldsymbol{a}_f$ serves as the initial estimate for the joint angles, it makes sense to perform the update $\boldsymbol{a}_f = \boldsymbol{a}_f^{\bullet}$ once a solution has been reached, improving the initial joint angle estimate for the next evaluation of $\widehat{\boldsymbol{y}}_f^{\bullet}$.

Approximating the derivatives of $\mathbf{J}_{2\mathrm{o}}$ with the centered finite difference formula requires $16 \cdot n_{df}$ evaluations of $\widehat{\boldsymbol{y}}_f^{\bullet}$ as well as $8 \cdot n_{df}$ subtractions and scalar multiplications of a 6-vector. As premature termination of the inner loop would cause numerical errors in the calculation of $\mathbf{J}_{2\mathrm{o}}$, it is desirable for the inner level to fully converge. Convergence to a gradient norm of less than 10^{-10} occurs in about 7 iterations, although this figure varies across data frames. The update step of equation (4.5) requires the solution of a $(8 + 6 \cdot n_{df}) \times 8$ system of linear equations, as well as an additional n_{df} evaluations of $\widehat{\boldsymbol{y}}_f^{\bullet}$ and n_{df} 6-vector subtractions to calculate the updated residual vector,$\widetilde{\boldsymbol{y}}^{\bullet}$.

4.3.2 One-Level Optimization Method

The one-level optimization method estimates the model parameter and joint angle values using a L–M algorithm with update step

$$\begin{aligned} &\min_{\boldsymbol{s}} \left\| \begin{bmatrix} \widetilde{\boldsymbol{y}} \\ \mathbf{0} \end{bmatrix} + \begin{bmatrix} \mathbf{J}_1\mathbf{D} \\ \sqrt{\lambda}\mathbf{I} \end{bmatrix} \boldsymbol{s} \right\|^2 \\ &\begin{Bmatrix} \boldsymbol{p} \\ \boldsymbol{a} \end{Bmatrix}_{k+1} = \mathbf{D}\boldsymbol{s} + \begin{Bmatrix} \boldsymbol{p} \\ \boldsymbol{a} \end{Bmatrix}_{k}, \end{aligned} \tag{4.12}$$

where $\mathbf{D}$ is $(8+5\cdot n_{df})\times(8+5\cdot n_{df})$ diagonal matrix called the parameter scaling matrix. The values of its diagonal elements are given by one divided by the 2-norm of the corresponding column of the Jacobian [2, §4.2]. The product $\mathbf{D}\boldsymbol{s}$ forms the update which modifies the model parameters and all of the joint angles. $\mathbf{J}_1$ has the form

$$\begin{bmatrix} \frac{\partial \widehat{\boldsymbol{y}}_{1,1}}{\partial \boldsymbol{p}_1} & \cdots & \frac{\partial \widehat{\boldsymbol{y}}_{1,1}}{\partial \boldsymbol{p}_8} & \frac{\partial \widehat{\boldsymbol{y}}_{1,1}}{\partial \boldsymbol{a}_{1,1}} & \cdots & \frac{\partial \widehat{\boldsymbol{y}}_{1,1}}{\partial \boldsymbol{a}_{1,5}} & 0 & \cdots & 0 & 0 & \cdots \\ \vdots & \vdots & \vdots & \vdots & \ddots & \vdots & \vdots & \ddots & \vdots & \vdots & \ddots \\ \frac{\partial \widehat{\boldsymbol{y}}_{1,6}}{\partial \boldsymbol{p}_1} & \cdots & \frac{\partial \widehat{\boldsymbol{y}}_{1,6}}{\partial \boldsymbol{p}_8} & \frac{\partial \widehat{\boldsymbol{y}}_{1,6}}{\partial \boldsymbol{a}_{1,1}} & \cdots & \frac{\partial \widehat{\boldsymbol{y}}_{1,6}}{\partial \boldsymbol{a}_{1,5}} & 0 & \cdots & 0 & 0 & \cdots \\ \frac{\partial \widehat{\boldsymbol{y}}_{2,1}}{\partial \boldsymbol{p}_1} & \cdots & \frac{\partial \widehat{\boldsymbol{y}}_{2,1}}{\partial \boldsymbol{p}_8} & 0 & \cdots & 0 & \frac{\partial \widehat{\boldsymbol{y}}_{2,1}}{\partial \boldsymbol{a}_{2,1}} & \cdots & \frac{\partial \widehat{\boldsymbol{y}}_{2,1}}{\partial \boldsymbol{a}_{2,5}} & 0 & \cdots \\ \vdots & \vdots & \vdots & \vdots & \ddots & \vdots & \vdots & \ddots & \vdots & \vdots & \ddots \\ \frac{\partial \widehat{\boldsymbol{y}}_{2,6}}{\partial \boldsymbol{p}_1} & \cdots & \frac{\partial \widehat{\boldsymbol{y}}_{2,6}}{\partial \boldsymbol{p}_8} & 0 & \cdots & 0 & \frac{\partial \widehat{\boldsymbol{y}}_{2,6}}{\partial \boldsymbol{a}_{2,1}} & \cdots & \frac{\partial \widehat{\boldsymbol{y}}_{2,6}}{\partial \boldsymbol{a}_{2,5}} & 0 & \cdots \\ \frac{\partial \widehat{\boldsymbol{y}}_{3,1}}{\partial \boldsymbol{p}_1} & \cdots & \frac{\partial \widehat{\boldsymbol{y}}_{3,1}}{\partial \boldsymbol{p}_8} & 0 & \cdots & 0 & 0 & \cdots & 0 & \frac{\partial \widehat{\boldsymbol{y}}_{3,1}}{\partial \boldsymbol{a}_{3,1}} & \cdots \\ \vdots & \vdots & \vdots & \vdots & \ddots & \vdots & \vdots & \ddots & \vdots & \vdots & \ddots \end{bmatrix}, \tag{4.13}$$

and dimension $(6\cdot n_{df})\times(8+5\cdot n_{df})$. The model parameters affect $\widehat{\boldsymbol{y}}$ in every frame of data, and the first 8 columns (there are 8 model parameters) of the Jacobian have $6\cdot n_{df}$ elements. Following these, there are 6×5 blocks arranged in a diagonal fashion, each one giving the derivatives of $\widehat{\boldsymbol{y}}$ with respect to the joint angles of a particular data frame. Approximating the derivatives in $\mathbf{J}_1$ by the centered finite difference formula requires $26\cdot n_{df}$ evaluations of the model function as well as $13\cdot n_{df}$ subtractions and scalar multiplications of a 6-vector. Each update step requires solving a sparse $(8+11\cdot n_{df})\times(8+5\cdot n_{df})$ system of linear

equations, as well as n_{df} model function evaluations and 6-vector subtractions to calculate the updated residual vector, $\widetilde{\boldsymbol{y}}$.

4.4 Results

Results are presented for the fitting of the 5 DoF model of the hip and knee to a representative data set with 1491 frames of data. The two algorithms converge to nearly identical results for both the model parameters and joint angles. The model parameters at solution differed by less than 10^{-7} between methods, with units of meters for position and radians for orientation. Joint angle differences were below 2×10^{-5} degrees.

Both methods are reasonably well conditioned; the outer level of the two-level method has a condition number of 37.5 with minimum and maximum singular values of $\sigma_{min} = 1.77$ and $\sigma_{max} = 66.5$, while the one-level method has a condition number of 86.5 with $\sigma_{min} = 0.022$ and $\sigma_{max} = 1.91$. Because the two-level algorithm relegates the estimation of joint angle values to the inner level, the parameter covariance matrix for its outer level contains only model parameters and has dimension 8×8. The parameter covariance matrix for the one-level algorithm contains the model parameters and all of the joint angles, attaining the dimension $(8 + 5 \cdot n_{df}) \times (8 + 5 \cdot n_{df})$. This fact underlies the different singular values and conditioning between the Jacobians of the two methods; it also raises the possibility that the two-level method could mask a poorly conditioned problem.

Calculation speed is quite different between the two methods, which is most easily seen in the calculation of the Jacobian. For the outer level of the two-level method, this takes about 25 seconds on a machine operating at 35 Gflop/s. For the one-level method on the same machine, this takes about 0.85 seconds.

4.5 Discussion

It should be noted that Sommer and Miller used the iterative method of [1] for the inner level of the two-level optimization method, while a plain L–M algorithm was employed in this paper. This change from the original method saved the authors from having to reformulate the model's spherical joint in terms of revolutes.

In their presentation of the two-level optimization method, Sommer and Miller [6] explicitly mention the one-level method, stating that it "violates the spirit of experimental modeling" because each additional frame of data requires more values (joint angles) to be estimated in the outer level. They state, "rather than requiring the estimation of more ... values, each additional [frame of] data should add to the confidence in the computed values of the [model] parameters." This fails to realize that, for data measured with 6 DoF, each additional frame of data does add to the confidence in the estimated model parameters and joint angles, as long as the model has 5 or fewer DoF. For a 5 DoF model with 8 model parameters, the update step for the one-level method (equation (4.12)) is an overdetermined linear system when the number of data frames is 9 or more.

The one-level method produces results in good agreement with the two-level method, remains reasonably well-conditioned, and has a distinct speed advantage. For these reasons, we recommend its use.

Bibliography

Chapter 1

[1] Milton Abramowitz and Irene A. Stegun, editors. *Handbook of Mathematical Functions With Formulas, Graphs, and Mathematical Tables.* United States Department of Commerce, National Bureau of Standards, 1972.

[2] Richard C. Aster, Brian Borchers, and Clifford H. Thurber. *Parameter Estimation and Inverse Problems*, volume 90 of *International Geophysics Series.* Elsevier Academic Press, 2005.

[3] A. L. Bell, D. R. Pederson, and R. A. Brand. A comparison of the accuracy of several hip center location prediction methods. *Journal of Biomechanics*, 23:617–21, 1990.

[4] Daniel L. Benoit, Dan K. Ramsey, Mario Lamontagne, Lanyi Xu, Per Wretenberg, and Per Renström. In vivo knee kinematics during gait reveals new rotation profiles and smaller translations. *Clinical Orthopaedics and Related Research*, (454):81–88, 2007.

[5] Valentina Camomilla, Andrea Cereatti, Giuseppe Vannozzi, and Aurelio Cappozzo. An optimized protocol for hip joint centre determination using the functional method. *Journal of Biomechanics*, 39(6):1096–1106, 2006.

[6] A. Cappozzo, F. Catani, U. Della Croce, and A. Leardini. Position and orientation in space of bones during movement: anatomical frame definition and determination. *Clinical Biomechanics*, 10(4):171–178, 1995.

[7] Aurelio Cappozzo, Ugo Della Croce, Alberto Leardini, and Lorenzo Chiari. Human movement analysis using stereophotogrammetry: Part 1: theoretical background. *Gait & Posture*, 21(2):186–196, 2005.

[8] G. K. Cole, M. R. Yeadon, B. M. Nigg, and J. L. Ronsky. Application of the joint coordinate system to three-dimensional joint attitude and movement representation: A standardization proposal. *Journal of Biomechanical Engineering*, 115(4A):344–349, November 1993.

[9] R. B. Davis, III, S. Õunpuu, D. Tyburski, and J. R. Gage. A gait analysis data collection and reduction technique. *Human Movement Science*, 10:575–587, 1991.

[10] Ugo Della Croce, Leardini Alberto, Lorenzo Chiari, and Cappozzo Aurelio. Human movement analysis using stereophotogrammetry part 4: assessment of anatomical landmark misplacement and its effects on joint kinematics. *Gait and Posture*, 21:226–237, 2005.

[11] Rainald M. Ehrig, William R. Taylor, Georg N. Duda, and Markus O. Heller. A survey of formal methods for determining the centre of rotation of ball joints. *Journal of Biomechanics*, 39(15):2798–2809, 2006.

[12] Rainald M. Ehrig, William R. Taylor, Georg N. Duda, and Markus O. Heller. A survey of formal methods for determining functional joint axes. *Journal of Biomechanics*, 40 (10):2150–2157, 2007.

[13] Roger Fletcher. *Practical Methods of Optimization*, volume 1. John Wiley & Sons, 1980.

[14] Sahan S. Hiniduma Udugama Gamage and Joan Lasenby. New least squares solutions for estimating the average centre of rotation and the axis of rotation. *Journal of Biomechanics*, 35(1):87–93, 2002.

[15] Ruth Globus. What is gravity, July 2002. URL `http://settlement.arc.nasa.gov/teacher/lessons/bryan/microgravity/gravback.html`. Accessed Oct 2014.

[16] S. Gratton, A.S. Lawless, and N.K. Nichols. Approximate gauss-newton methods for nonlinear least squares problems. Technical report, The University of Reading, 2004.

[17] E. S. Grood and W. J. Suntay. A joint coordinate system for the clinical description of three-dimensional motions: Application to the knee. *Journal of Biomechanical Engineering*, 105(2):136–144, May 1983.

[18] M. E. Harrington, A. B. Zavatsky, S. E. M. Lawson, Z. Yuan, and T. N. Theologis. Prediction of the hip joint centre in adults, children, and patients with cerebral palsy based on magnetic resonance imaging. *Journal of Biomechanics*, 40(3):595–602, 2007.

[19] James G. Hay and J. Gavin Reid. *The Anatomical and Mechanical Bases of Human Motion*. Prentice-Hall, 1982.

[20] Michael T. Heath. *Scientific Computing: an Introductory Survey*. McGraw-Hill, second edition, 2002.

[21] Alberto Leardini, Aurelio Cappozzo, Fabio Catani, Soren Toksvig-Larsen, Aldo Petitto, Vincenzo Sforza, Giancarlo Cassanelli, and Sandro Giannini. Validation of a functional method for the estimation of hip joint centre location. *Journal of Biomechanics*, 32(1): 99–103, 1999.

[22] Alberto Leardini, Lorenzo Chiari, Ugo Della Croce, and Aurelio Cappozzo. Human movement analysis using stereophotogrammetry: Part 3. soft tissue artifact assessment and compensation. *Gait & Posture*, 21(2):212–225, 2005.

[23] Metria Innovation, Inc. MC 40180 moire phase tracking system brochure. URL `http://www.metriainnovation.com/pdfs/MC_40180_Brochure.pdf`. Accessed Oct 2014.

[24] Donald A. Neumann. *Kinesiology of the Musculoskeletal System*. Mosby, 2002.

[25] Jorge Nocedal and Steven J. Wright. *Numerical Optimization*. Springer, second edition, 2006.

[26] Stephen J. Piazza and Peter R. Cavanagh. Measurement of the screw-home motion of the knee is sensitive to errors in axis alignment. *Journal of Biomechanics*, 33(8): 1029–1034, 2000.

[27] Morgan Sangeux, Alana Peters, and Richard Baker. Hip joint centre localization: Evaluation on normal subjects in the context of gait analysis. *Gait & Posture*, 34(3):324–328, 2011.

[28] Anthony G. Schache, Richard Baker, and Larry W. Lamoreux. Defining the knee joint flexion-extension axis for purposes of quantitative gait analysis: An evaluation of methods. *Gait & Posture*, 24(1):100–109, 2006.

[29] Michael H. Schwartz and Adam Rozumalski. A new method for estimating joint parameters from motion data. *Journal of Biomechanics*, 38(1):107–116, 2005.

[30] George Arthur Frederick Seber and Christopher John Wild. *Nonlinear Regression*. Wiley Series in Probability and Mathematical Statistics. John Wiley & Sons, 1988.

[31] Jonathan Sinclair, Paul J. Taylor, and Lindsay Bottoms. The appropriateness of the helical axis technique and six available cardan sequences for the representation of 3-D lead leg kinematics during the fencing lunge. *Journal of Human Kinetics*, 37:7–15, 2013.

[32] H. J. Sommer, III and N. R. Miller. A technique for kinematic modeling of anatomical joints. *Journal of Biomechanical Engineering*, 102(4):311–317, November 1980.

[33] Rita Stagni, Alberto Leardini, Aurelio Cappozzo, Maria Grazia Benedetti, and Angelo Cappello. Effects of hip joint centre mislocation on gait analysis results. *Journal of Biomechanics*, 33(11):1479–1487, 2000.

[34] Gilbert Strang. *Linear Algebra and its Applications*. Harcourt Brace Jovanovich, third edition, 1988.

[35] W. R. Taylor, E. I. Kornaropoulos, G. N. Duda, S. Kratzenstein, R. M. Ehrig, A. Arampatzis, and M. O. Heller. Repeatability and reproducibility of ossca, a functional approach for assessing the kinematics of the lower limb. *Gait & Posture*, 32(2):231–236, 2010.

[36] S. J. Tupling and M. R. Pierrynowski. Use of cardan angles to locate rigid bodies in three-dimensional space. *Medical and Biological Engineering and Computing*, 25(5):

527–532, 1987. URL http://dx.doi.org/10.1007/BF02441745. J2: Med. Biol. Eng. Comput.

[37] User:Edoarado. File:anatomical planes-en.svg. Wikimedia Commons, CC-BY-SA-3.0, November 2011. URL http://commons.wikimedia.org/wiki/File:Anatomical_Planes-en.svg. Accessed Aug 2014.

[38] User:Inductiveload. File:maxima and minima.svg. Wikimedia Commons, public domain, October 2007. URL http://commons.wikimedia.org/wiki/File:Maxima_and_Minima.svg. Accessed Oct 2014.

[39] User:Nanoxyde. File:anatomical directions (fr).svg. Wikimedia Commons, CC-BY-SA-3.0, June 2011. URL http://commons.wikimedia.org/wiki/File:Anatomical_directions_%28fr%29.svg. Accessed Aug 2014.

[40] Anton J. van den Bogert, Graham D. Smith, and Benno M. Nigg. In vivo determination of the anatomical axes of the ankle joint complex: An optimization approach. *Journal of Biomechanics*, 27(12):1477–1488, December 1994.

[41] Mariana Ruiz Villarreal. File:human skeleton back en.svg. Wikimedia Commons, public domain, September 2007. URL http://commons.wikimedia.org/wiki/File:Human_skeleton_back_en.svg. Accessed Aug 2014.

[42] Mariana Ruiz Villarreal. File:human skeleton front en.svg. Wikimedia Commons, public domain, January 2007. URL http://commons.wikimedia.org/wiki/File:Human_skeleton_front_en.svg. Accessed Aug 2014.

[43] Joshua T. Weinhandl, Brian S. R. Armstrong, Todd P. Kusik, Robb T. Barrows, and Kristian M. O'Connor. Validation of a single camera three-dimensional motion tracking system. *Journal of Biomechanics*, 43(7):1437–1440, 2010.

[44] Ge Wu, Sorin Siegler, Paul Allard, Chris Kirtley, Alberto Leardini, Dieter Rosenbaum, Mike Whittle, Darryl D. D'Lima, Luca Cristofolini, Hartmut Witte, Oskar Schmid, and Ian Stokes. ISB recommendation on definition of joint coordinate system of various

joints for the reporting of human joint motion – Part I: ankle, hip, and spine. *Journal of Biomechanics*, 35:543–548, 2002.

[45] Vladimir M. Zatsiorsky. *Kinematics of Human Motion.* Human Kinetics, Champaign, IL, 1998.

Chapter 2

[1] L. Blankevoort, R. Huiskes, and A. De Lange. The envelope of passive knee joint motion. *Journal of Biomechanics*, 21(9):705–720, 1988.

[2] A. Cappozzo, F. Catani, U. Della Croce, and A. Leardini. Position and orientation in space of bones during movement: anatomical frame definition and determination. *Clinical Biomechanics*, 10(4):171–178, 1995.

[3] Aurelio Cappozzo, Ugo Della Croce, Alberto Leardini, and Lorenzo Chiari. Human movement analysis using stereophotogrammetry: Part 1: theoretical background. *Gait & Posture*, 21(2):186–196, 2005.

[4] G. K. Cole, M. R. Yeadon, B. M. Nigg, and J. L. Ronsky. Application of the joint coordinate system to three-dimensional joint attitude and movement representation: A standardization proposal. *Journal of Biomechanical Engineering*, 115(4A):344–349, November 1993.

[5] Ugo Della Croce, Leardini Alberto, Lorenzo Chiari, and Cappozzo Aurelio. Human movement analysis using stereophotogrammetry part 4: assessment of anatomical landmark misplacement and its effects on joint kinematics. *Gait and Posture*, 21:226–237, 2005.

[6] Rainald M. Ehrig, William R. Taylor, Georg N. Duda, and Markus O. Heller. A survey of formal methods for determining the centre of rotation of ball joints. *Journal of Biomechanics*, 39(15):2798–2809, 2006.

[7] Rainald M. Ehrig, William R. Taylor, Georg N. Duda, and Markus O. Heller. A survey of formal methods for determining functional joint axes. *Journal of Biomechanics*, 40 (10):2150–2157, 2007.

[8] M. E. Harrington, A. B. Zavatsky, S. E. M. Lawson, Z. Yuan, and T. N. Theologis. Prediction of the hip joint centre in adults, children, and patients with cerebral palsy based on magnetic resonance imaging. *Journal of Biomechanics*, 40(3):595–602, 2007.

[9] Jennifer L. Hicks and James G. Richards. Clinical applicability of using spherical fitting to find hip joint centers. *Gait & Posture*, 22(2):138–145, 2005.

[10] Anne M. Hollister, Sanjay Jatana, Anoop K. Singh, William W. Sullivan, and Andrei G. Lupichuk. The axes of rotation of the knee. *Clinical orthopaedics and related research*, 290:259–268, 1993.

[11] Alberto Leardini, Lorenzo Chiari, Ugo Della Croce, and Aurelio Cappozzo. Human movement analysis using stereophotogrammetry: Part 3. soft tissue artifact assessment and compensation. *Gait & Posture*, 21(2):212–225, 2005.

[12] T. W Lu and J. J. O'Connor. Bone position estimation from skin marker co-ordinates using global optimisation with joint constraints. *Journal of Biomechanics*, 32(2):129–134, 1999.

[13] Donald A. Neumann. *Kinesiology of the Musculoskeletal System.* Mosby, 2002.

[14] E. E. Pavan, P. Taboga, and C. Frigo. Feasibility of a new — joint constrained — lower limb model for gait analysis application. *Gait & Posture*, 24, Supplement 2(0):S20–S21, 2006.

[15] Stephen J. Piazza and Peter R. Cavanagh. Measurement of the screw-home motion of the knee is sensitive to errors in axis alignment. *Journal of Biomechanics*, 33(8): 1029–1034, 2000.

[16] Irene Reichl, Winfried Auzinger, Heinz-Bodo Schmiedmayer, and Ewa Weinmüller. Reconstructing the knee joint mechanism from kinematic data. *Mathematical and Computer Modelling of Dynamical Systems*, 16(5):403–415, 2010.

[17] Jeffrey A. Reinbolt, Jaco F. Schutte, Benjamin J. Fregly, Byung Il Koh, Raphael T. Haftka, Alan D. George, and Kim H. Mitchell. Determination of patient-specific multi-joint kinematic models through two-level optimization. *Journal of Biomechanics*, 38 (3):621–626, 2005.

[18] C. Reinschmidt, A. J. van den Bogert, A. Lundberg, B. M. Nigg, N. Murphy, A. Stacoff, and A. Stano. Tibiofemoral and tibiocalcaneal motion during walking: external vs. skeletal markers. *Gait & Posture*, 6(2):98–109, 1997.

[19] Morgan Sangeux, Alana Peters, and Richard Baker. Hip joint centre localization: Evaluation on normal subjects in the context of gait analysis. *Gait & Posture*, 34(3):324–328, 2011.

[20] Anthony G. Schache, Richard Baker, and Larry W. Lamoreux. Defining the knee joint flexion-extension axis for purposes of quantitative gait analysis: An evaluation of methods. *Gait & Posture*, 24(1):100–109, 2006.

[21] Michael H. Schwartz and Adam Rozumalski. A new method for estimating joint parameters from motion data. *Journal of Biomechanics*, 38(1):107–116, 2005.

[22] Jonathan Sinclair, Paul J. Taylor, and Lindsay Bottoms. The appropriateness of the helical axis technique and six available cardan sequences for the representation of 3-D lead leg kinematics during the fencing lunge. *Journal of Human Kinetics*, 37:7–15, 2013.

[23] H. J. Sommer, III and N. R. Miller. A technique for kinematic modeling of anatomical joints. *Journal of Biomechanical Engineering*, 102(4):311–317, November 1980.

[24] Rita Stagni, Alberto Leardini, Aurelio Cappozzo, Maria Grazia Benedetti, and Angelo Cappello. Effects of hip joint centre mislocation on gait analysis results. *Journal of Biomechanics*, 33(11):1479–1487, 2000.

[25] Anton J. van den Bogert, Graham D. Smith, and Benno M. Nigg. In vivo determination of the anatomical axes of the ankle joint complex: An optimization approach. *Journal of Biomechanics*, 27(12):1477–1488, December 1994.

[26] Ge Wu, Sorin Siegler, Paul Allard, Chris Kirtley, Alberto Leardini, Dieter Rosenbaum, Mike Whittle, Darryl D. D'Lima, Luca Cristofolini, Hartmut Witte, Oskar Schmid, and Ian Stokes. ISB recommendation on definition of joint coordinate system of various joints for the reporting of human joint motion – Part I: ankle, hip, and spine. *Journal of Biomechanics*, 35:543–548, 2002.

[27] Vladimir M. Zatsiorsky. *Kinematics of Human Motion*. Human Kinetics, Champaign, IL, 1998.

Chapter 3

[1] Valentina Camomilla, Andrea Cereatti, Giuseppe Vannozzi, and Aurelio Cappozzo. An optimized protocol for hip joint centre determination using the functional method. *Journal of Biomechanics*, 39(6):1096–1106, 2006.

[2] A. Cappozzo, F. Catani, U. Della Croce, and A. Leardini. Position and orientation in space of bones during movement: anatomical frame definition and determination. *Clinical Biomechanics*, 10(4):171–178, 1995.

[3] G. K. Cole, M. R. Yeadon, B. M. Nigg, and J. L. Ronsky. Application of the joint coordinate system to three-dimensional joint attitude and movement representation: A standardization proposal. *Journal of Biomechanical Engineering*, 115(4A):344–349, November 1993.

[4] Ugo Della Croce, Leardini Alberto, Lorenzo Chiari, and Cappozzo Aurelio. Human movement analysis using stereophotogrammetry part 4: assessment of anatomical landmark misplacement and its effects on joint kinematics. *Gait and Posture*, 21:226–237, 2005.

[5] J. Fuller, L. J Liu, M. C. Murphy, and R. W. Mann. A comparison of lower-extremity skeletal kinematics measured using skin- and pin-mounted markers. *Human Movement Science*, 16(2?3):219–242, 1997.

[6] E. S. Grood and W. J. Suntay. A joint coordinate system for the clinical description of three-dimensional motions: Application to the knee. *Journal of Biomechanical Engineering*, 105(2):136–144, May 1983.

[7] M. E. Harrington, A. B. Zavatsky, S. E. M. Lawson, Z. Yuan, and T. N. Theologis. Prediction of the hip joint centre in adults, children, and patients with cerebral palsy based on magnetic resonance imaging. *Journal of Biomechanics*, 40(3):595–602, 2007.

[8] Anne M. Hollister, Sanjay Jatana, Anoop K. Singh, William W. Sullivan, and Andrei G. Lupichuk. The axes of rotation of the knee. *Clinical orthopaedics and related research*, 290:259–268, 1993.

[9] Evgenios I. Kornaropoulos, William R. Taylor, Georg N. Duda, Rainald M. Ehrig, Georg Matziolis, Michael Müller, Georgi Wassilew, Patrick Asbach, Carsten Perka, and Markus O. Heller. Frontal plane alignment: An imageless method to predict the mechanical femoral-tibial angle (mFTA) based on functional determination of joint centres and axes. *Gait & Posture*, 31(2):204–208, 2010.

[10] T. W Lu and J. J. O'Connor. Bone position estimation from skin marker co-ordinates using global optimisation with joint constraints. *Journal of Biomechanics*, 32(2):129–134, 1999.

[11] Luigi Lucchetti, Aurelio Cappozzo, Angelo Cappello, and Ugo Della Croce. Skin movement artefact assessment and compensation in the estimation of knee-joint kinematics. *Journal of Biomechanics*, 31(11):977–984, 1998.

[12] E. E. Pavan, P. Taboga, and C. Frigo. Feasibility of a new — joint constrained — lower limb model for gait analysis application. *Gait & Posture*, 24, Supplement 2(0):S20–S21, 2006.

[13] Alana Peters, Brook Galna, Morgan Sangeux, Meg Morris, and Richard Baker. Quantification of soft tissue artifact in lower limb human motion analysis: A systematic review. *Gait & Posture*, 31(1):1–8, 2010.

[14] Jeffrey A. Reinbolt, Jaco F. Schutte, Benjamin J. Fregly, Byung Il Koh, Raphael T. Haftka, Alan D. George, and Kim H. Mitchell. Determination of patient-specific multi-joint kinematic models through two-level optimization. *Journal of Biomechanics*, 38 (3):621–626, 2005.

[15] Morgan Sangeux, Alana Peters, and Richard Baker. Hip joint centre localization: Evaluation on normal subjects in the context of gait analysis. *Gait & Posture*, 34(3):324–328, 2011.

[16] Anthony G. Schache, Richard Baker, and Larry W. Lamoreux. Defining the knee joint flexion-extension axis for purposes of quantitative gait analysis: An evaluation of methods. *Gait & Posture*, 24(1):100–109, 2006.

[17] Michael H. Schwartz and Adam Rozumalski. A new method for estimating joint parameters from motion data. *Journal of Biomechanics*, 38(1):107–116, 2005.

[18] H. J. Sommer, III and N. R. Miller. A technique for kinematic modeling of anatomical joints. *Journal of Biomechanical Engineering*, 102(4):311–317, November 1980.

[19] Ben C. Tesch and Brian S. R. Armstrong. Parameter identifiability in a five degree of freedom mechanism with applications in human movement analysis. *Unpublished*, 2014.

[20] S. J. Tupling and M. R. Pierrynowski. Use of cardan angles to locate rigid bodies in three-dimensional space. *Medical and Biological Engineering and Computing*, 25(5): 527–532, 1987. URL `http://dx.doi.org/10.1007/BF02441745`. J2: Med. Biol. Eng. Comput.

[21] Anton J. van den Bogert, Graham D. Smith, and Benno M. Nigg. In vivo determination of the anatomical axes of the ankle joint complex: An optimization approach. *Journal of Biomechanics*, 27(12):1477–1488, December 1994.

[22] Joshua T. Weinhandl, Brian S. R. Armstrong, Todd P. Kusik, Robb T. Barrows, and Kristian M. O'Connor. Validation of a single camera three-dimensional motion tracking system. *Journal of Biomechanics*, 43(7):1437–1440, 2010.

[23] Ge Wu, Sorin Siegler, Paul Allard, Chris Kirtley, Alberto Leardini, Dieter Rosenbaum, Mike Whittle, Darryl D. D'Lima, Luca Cristofolini, Hartmut Witte, Oskar Schmid, and Ian Stokes. ISB recommendation on definition of joint coordinate system of various joints for the reporting of human joint motion – Part I: ankle, hip, and spine. *Journal of Biomechanics*, 35:543–548, 2002.

Chapter 4

[1] J. Denavit and R. S. Hartenberg. An iterative method for the displacement analysis of spatial mechanisms. *Journal of Applied Mechanics*, 31(2):309–314, June 1964.

[2] John M. Hollerbach and Charles W. Wampler. The calibration index and taxonomy for robot kinematic calibration methods. *The International Journal of Robotics Research*, 15(6):573–591, 1996.

[3] Alana Peters, Brook Galna, Morgan Sangeux, Meg Morris, and Richard Baker. Quantification of soft tissue artifact in lower limb human motion analysis: A systematic review. *Gait & Posture*, 31(1):1–8, 2010.

[4] Jeffrey A. Reinbolt, Jaco F. Schutte, Benjamin J. Fregly, Byung Il Koh, Raphael T. Haftka, Alan D. George, and Kim H. Mitchell. Determination of patient-specific multi-joint kinematic models through two-level optimization. *Journal of Biomechanics*, 38(3): 621–626, 2005.

[5] George Arthur Frederick Seber and Christopher John Wild. *Nonlinear Regression*. Wiley Series in Probability and Mathematical Statistics. John Wiley & Sons, 1988.

[6] H. J. Sommer, III and N. R. Miller. A technique for kinematic modeling of anatomical joints. *Journal of Biomechanical Engineering*, 102(4):311–317, November 1980.

[7] Ben C. Tesch, Brian S. R. Armstrong, and Kristian M. O'Connor. An optimization method for estimating joint parameters at the hip and knee without thigh marker data. *Unpublished*, 2014.

[8] S. J. Tupling and M. R. Pierrynowski. Use of cardan angles to locate rigid bodies in three-dimensional space. *Medical and Biological Engineering and Computing*, 25(5):527–532, 1987. URL `http://dx.doi.org/10.1007/BF02441745`. J2: Med. Biol. Eng. Comput.